Investigation of propeller characteristics at low Reynolds number with an angle of attack

A computational aeroacoustic study

Akash Pandey

Master of Science Thesis

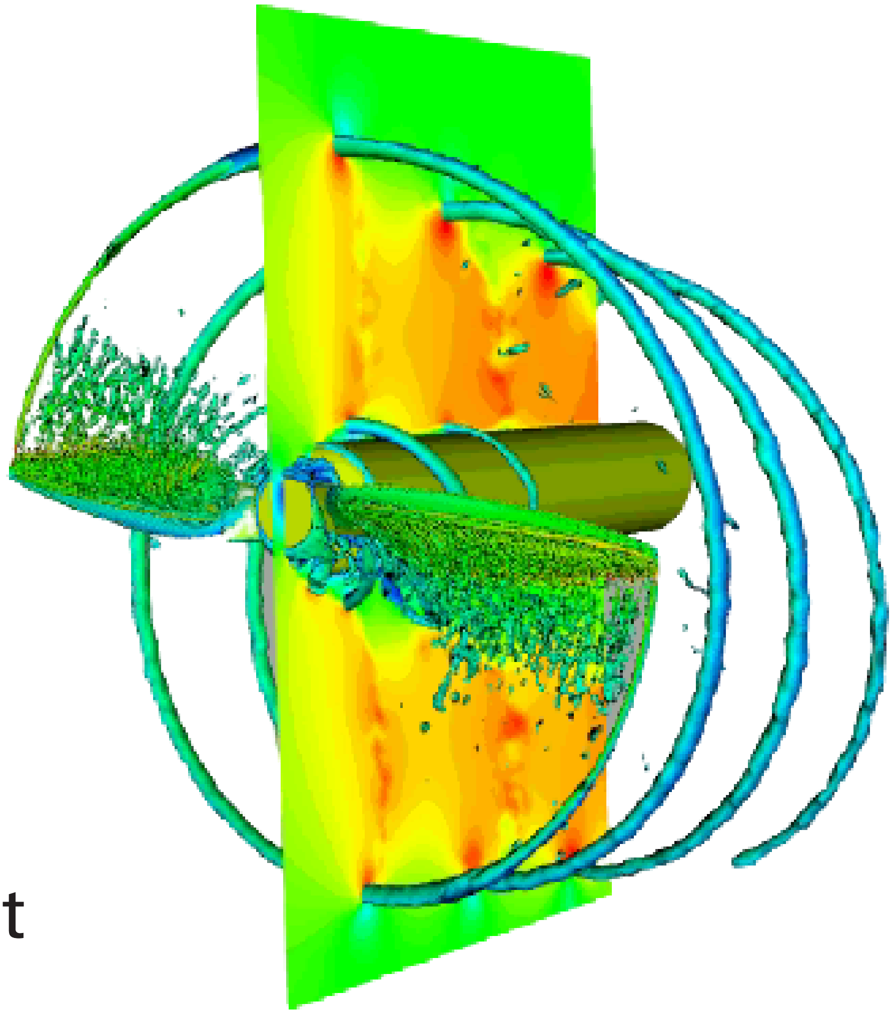

TU Delft

Investigation of propeller characteristics at low Reynolds number with an angle of attack

A computational aeroacoustic study

by

Akash Pandey

to obtain the degree of Master of Science
at the Delft University of Technology,
to be defended publicly on Wednesday, 7^{th} of April, 2021.

Student number:	4792955	
Research group :	Aeroacoustics group, Aerodynamics and Wind Energy track	
Thesis committee:	Prof. dr. D. Casalino,	TU Delft, chair
	Dr. F. Avallone,	TU Delft, supervisor
	Dr. D. Ragni,	TU Delft, supervisor
	G. Romani,	TU Delft, supervisor
	Dr. T. Sinnige,	TU Delft, external examiner

Acknowledgement

> ”Hard times create strong people, strong people create good times.”
>
> -G. Michael Hopf

It is how I would like to sum my experience of doing the thesis and my hopes for the future. Doing my master’s thesis in the middle of a pandemic with the entire aviation industry in shambles was perhaps never a part of my worst nightmare. Add to it the feeling of isolation and uncertainty coupled with my extroverted nature, and you have a recipe for disaster. Yet here we are, reading the acknowledgment section of my master’s thesis. So I guess these are some very special people, without whom this thesis couldn’t have been possible.

First of all, thank you to my family, mummy, papa, Aman. Despite being on three different continents, we never got distant. It is hard to put in words all that you have done for me. But all I can say is I owe all my success to your support. Shreyas and, Arpit thank you for being there no matter the time or place you guys have become family over the years. The Discord sessions and calls with you made work from home more bearable. My housemates Agnieszka, Kristyna, John, and Lilly, thank you for creating a home away from home and making the lockdown fun. Dr. Vinit and Ankur bhaiya for being the guiding lights of my journey in Delft. Both of you inspire me with your can-do attitude and deep knowledge of your respective fields. I have learned so much from you, and I sincerely hope it continues to be this way. My friends from Delft Abhratej, Anshita, Athreya, Hrishikesh, Haris, and Shubham. It was a delight working with you on the courses, having light-hearted discussions, and getting valuable feedback. Delft wouldn’t have been the same without you.

A big thank you to James, Ruben, Quint, Alex, Thom, Tom, Victor, Teresa, and all the other teammates at Silverwing. My best memories from Delft are with you guys. It was an absolute delight working, playing, and doing all sorts of random stuff with you guys. Making the aircraft has been one of the most enriching experiences of my life and was a great motivation in further exploring the field of aeroacoustics.

At TU Delft, I would like to extend my sincerest gratitude to Dr. Francesco Avallone for his guidance, support, and patience. Working with him has helped me develop a more critical attitude and an eye for detail. I am also thankful to Dr. Daniele Ragni and Gianluca, for providing their valuable inputs and enabling me to improve my work. It was a pleasure working with you and learning from you.

Lastly, I would like to acknowledge the role of COVID-19 in my thesis. Thank you for giving me so much time in isolation with my thoughts, thank you for making it so hard, and thank you for making me realize that I can do it. To close the loop, I would like to end with another quote that sums up all my learnings so far:

”The hardest battles that you would ever fight is with yourself.”

Akash Pandey
Delft, 2021

Summary

Advancements in technology have made commercial unmanned aerial vehicles reliable and readily available, leading to an exponential rise in their market demand over the past few years. COVID-19 has further accelerated this growth through an increase in demand for contact-less delivery and crowd monitoring systems. However, despite these favorable conditions, their limited range, perceived threat, and concerns about noise pollution in urban environments have prevented them from being widely accepted by society. A recent study by NASA [1] found that people perceive UAV noise to be more annoying than cars, and trucks at a similar sound pressure level, which highlights the need to understand the acoustic characteristic of these aircraft.

These UAVs are generally powered by electric motors, making their propellers the most dominant source of noise. In the past, researchers have conducted several studies to understand and characterize the noise produced by aircraft propellers. However, these studies were limited to high Reynolds ($> 10^6$) and Mach number operations for large commercial aircraft, creating a significant gap in the understanding of the aerodynamic and acoustic characteristics of propellers operating at low Reynolds ($< 2*10^5$) and Mach number. This thesis aims to address the research gap by performing a high-fidelity computational simulation using Dassault Systèmes PowerFLOW®. The tool uses a lattice Boltzmann-very large eddy simulation (LBM-VLES) based approach to compute the aerodynamic results and the Ffowcs-Williams and Hawkings (FWH) aeroacoustic analogy to calculate far-field acoustic values. The main objective of the thesis is:

> **"To characterize and quantify the effect of non-axisymmetric inflow conditions on the aerodynamic and acoustic properties of propellers operating at low Reynolds numbers."**

To meet the objective, a computational setup consisting of a twin-bladed propeller with a radius of $15\ cm$ is designed in PowerFLOW®. The propeller is analyzed at 0^o and 15^o AoA, operating at 6000 RPM with a freestream velocity of $12\ m/sec$ and the results validated against experimental data.

Aerodynamic measurements and flow analysis revealed that the change in angle of attack (AoA) resulted in a 3.87% increase in the net thrust, and 1.16% increase in the net torque value of the propeller. Operating at an AoA, the propeller blade experiences asymmetric loading around the propeller plane, the loads fluctuate by 35% between the points of maximum and minimum loading. Further analysis of the propeller flow field is carried out by averaging the velocity field and performing a phase-locked analysis to visualize the vortex field. The analysis helps in understanding the effect of AoA on propeller wake and quantifies its asymmetric nature.

Far-field acoustic data is acquired by two circular microphone arrays, with a polar angle resolution of 10^o. The arrays are placed around the propeller plane and along the axial axis of the propeller. The change in AoA results in a $3\ dB$ higher noise at an azimuthal angle (Ψ) of 90^o and reduces by an equal magnitude at $\Psi = 270^o$. The shift is attributed to the change in propeller tip Mach number and local blade AoA as a function of its azimuthal location and propeller AoA. Further analysis of the sound power level (PWL) produced by the propeller is carried out, showing a $1.5\ dB$ increase in the PWL produced by the propeller blade at 15^o AoA than 0^o.

Contents

List of Abbreviations

AoA	Angle of attack
BC	Boundary condition
BPF	Blade passing frequency
BVI	Blade vortex interaction
CAA	Computational aeroacoustics
CFD	Computational fluid dynamics
FWH	Ffowcs-Williams and Hawkings
FWH SLD	Ffowcs-Williams and Hawkings solid integration surface
FWH PRM	Ffowcs-Williams and Hawkings permeable integration surface
ICAO	International Civil Aviation Organization
LBM	Lattice Boltzmann method
LHS	Left hand side
LRF	Local rotating reference frame
OASPL	Overall sound pressure level
NS	Navier-Stokes
PAVs	Personal aerial vehicle
PS	Power spectrum
PSD	Power spectral density
PWL	Sound power level
RHS	Right hand side
RPM	Rounds per minute
SPL	Sound pressure level
SR	Single-rotating propellers
TR	Total reaction
UAVs	Unmanned aerial vehicle
VR	Variable resolution
VTOL	Vertical takeoff and landing
STOL	Short takeoff and landing

List of Symbols

Greek Symbols

α	Angle of attack $(^o)$
β	Blade pitch angle $(^o)$
η	Efficiency
θ	Axial angle $(^o)$
λ	Wavelength (m)
ρ	Density (Kg/m^3)
ϕ	Radiation angle $(^o)$
Ψ	Azimuthal angle of propeller $(^o)$
ω	Vorticity magnitude (Hz)

Latin Symbols

B	Number of propeller blades
C_d	Coefficient of drag
C_l	Coefficient of lift
C_T	Coefficient of thrust
C_Q	Coefficient of torque
D	Diameter (m)
dB	Decibel
f	Frequency (Hz)
J	Bessel function of the first kind
J	Advance ratio
k	Wave number
K	Kelvin
l	Characteristic length (mm)
M	Mach number
n	Rotations per second $(1/sec)$
N	Newtons
N	Number of blades
p	Pressure (Pa)

P	Power (W)
r	Sectional radius (mm)
R	Propeller radius (m)
Q	Torque (Nm)
Re	Reynolds number
t	Time (sec)
T	Temperature (K)
U_∞	Freestream fluid velocity (m/sec)

List of Figures

List of Tables

1

Introduction

Advancements in technology have made commercial unmanned aerial vehicles (UAVs) readily available to the public. Initially viewed as a military device, drones are now widely used by civilians as well. Thanks to their reduced cost, small size, and ability to perform hazardous tasks (mapping, inspecting, and/or surveying in contaminated/remote areas, etc.), drones are finding increased application in several sectors of the economy such as energy, mining, entertainment, and agriculture to name a few. As of 2018, the global commercial drone market was valued at $ 5.8 billion with an estimated sale of around 274,600 units in 2018 [20]. Startups like Zipline and Wingcopter have used drones to deliver medical supplies in remote regions of Africa. Technology giants like Amazon and Google are exploring avenues to use drones for package delivery in dense urban environments. COVID-19 has helped shift public perception about drones. People have now started accepting drones as a means of performing contactless delivery, and for disinfecting/monitoring public spaces. The increased use of drones comes with safety, privacy, and nuisance-related challenges. Authorities and operators expect factors like lack of trained UAV pilots, privacy concerns by the public, UAV traffic management issues, and the noise produced by them to be some of the hurdles restricting their market potential. In recent years investment by organizations into the research and development of UAVs has helped alleviate several issues regarding UAV operations however, the noise produced by such aircraft remains a cause of concern.

Figure 1.1: Drones performing aerial delivery of medical supplies; A hybrid tilt rotor UAV (left) and a fixed wing delivery drone (right)

To date, electric motors have been the preferred mode of powering UAVs. They provide a simpler, more efficient, and less noisy alternative to internal combustion/jet engines. Electric motors also enable drones to swivel their propellers, offering a relatively smooth transition from horizontal to vertical flight, giving these aircraft vertical take-offs and landing (VTOL) capabilities. As a result of which the propellers on these UAVs experience a higher range of angle of attack (AoA) than traditional aircraft. The relatively small size and diverse mission profiles of these UAVs, coupled with their proposed operating environment (dense urban areas) offer a unique set of challenges in understanding their acoustic characteristics.

Over the years, there have been several successful attempts in understanding and isolating the noise of propellers operating at high Reynolds numbers ($> 10^6$). However, research to understand the aerodynamic and aeroacoustic characteristics of propellers operating at low Reynolds ($< 2 * 10^5$) numbers and with an AoA is limited. The thesis aims to address the research gap by performing a critical analysis on the aerodynamic and aeroacoustic characteristics of propellers operating at low Reynolds numbers with an AoA.

1.1. Research objective

Researchers have dedicated considerable resources towards understanding the effect of installation (presence of wings, nacelle, strut, etc.) and small variations in AoA [12, 21–23] on the aerodynamic and acoustic characteristics of propellers. However, most of these analyses were performed in the late 1900s for large turbo-prop aircraft operating at considerably higher Reynolds numbers ($> 10^6$). Around 2010, manufacturers like DJI, Parrot, etc., made drones available to commercial consumers. The availability of commercial drones sparked a new wave of research in the field of UAVs. The past decade has seen researchers conduct several studies to understand the aerodynamic and acoustic characteristics of propellers at low Reynolds numbers. These studies, however, have mainly been done for axisymmetric inflow conditions. Most commercial UAVs (tilt or multi-rotor) have VTOL capabilities. A typical mission profile of such a UAV includes vertical take-off, landing, transitioning to horizontal flight, and cruise. The propellers experience significant changes in AoA during these flight phases. The non-zero AoA results in unsteady loading due to the variation in effective AoA for the propeller blade element around the propeller plane. These changes impact the aerodynamics, and consequently, the acoustic characteristics of the propeller. The goal of this thesis is:

> **“To characterize and quantify the effect of non-axisymmetric inflow conditions on the aerodynamic and acoustic properties of propellers operating at low Reynolds numbers.”**

The goal shall be met by attaining the following objectives:

1. Understanding the aerodynamic and acoustic characteristics of propellers operating at low Reynolds numbers and identify the differences compared to propellers operating at high Reynolds numbers.
2. Quantifying and analyzing the changes in aerodynamic and acoustic characteristics of the propeller due to AoA.

The first objective is met by carrying out an extensive literature review. The learnings from the literature reviewed are discussed in Chapter 3. The chapter also lists the research questions that will be answered through this thesis. The second objective has been achieved by carrying out a high-fidelity computational analysis of a UAV propeller operating at a low Reynolds number. The details of the setup used have been discussed in Chapter 5. The following section discusses the approach taken to reach the objective and the motivation behind its selection.

1.2. Approach

Based on the literature review and in consideration of the present experimental research at TU Delft, conducting a computational study was deemed to be the best approach. It would complement the experimental research and help create a benchmark computational setup that can be used for future studies. The computational analysis also provides some distinct advantages over experimental studies, which are listed below:

- It eliminates the uncertainties caused due to structural vibrations experienced by an experimental setup. Which could translate into unsteady blade motion resulting in additional noise sources.
- Acoustic measurements in a computational analysis do not contain wind tunnel background noise and other superfluous noise sources, such as electric motor noise, making it easier to analyze the aerodynamic noise produced by the propeller.

- In a computational analysis, placement of microphones does not alter the flow field, enabling a 360^o directivity analysis.

The computational setup consists of an isolated twin-bladed propeller with a diameter of $30\ cm$ rotating at $6,000$ RPM. The simulation is carried out with a free stream velocity of $12\ m/sec$ at an AoA of 0^o and 15^o. A high fidelity computational flow solver PowerFLOW®, developed by Dassault Systèmes has been utilized for this study. It utilizes the lattice-Boltzmann method (LBM) alongside a very large-eddy simulation (VLES) turbulence modeling approach to resolve the flow field. The reason for choosing such a solver over a traditional Navier-Stokes-based solver is their higher computational efficiency, lower dispersion, and dissipation errors [24]. The computation of the acoustic field is performed using the Ffowcs Williams–Hawkings (FWH) analogy. A more detailed discussion on the flow solver and the computational setup has been carried out in Chapter 4 and 5 respectively.

1.3. Outline of thesis

Along with the present chapter, this report consists of 8 other chapters. A brief introduction to which has been provided below:

- `Chapter 2:` provides the reader with the theoretical background in propeller aerodynamics and aeroacosutics .
- `Chapter 3:` introduces the reader to the flow physics of a propeller operating at an AoA. It also discusses research in this field of propeller performance at low Reynolds numbers.
- `Chapter 4:` introduces the principles of the LBM, and its implementation into the flow solver. The chapter also discusses the implementation of the FWH analogy in the aeroacoustic solver of the tool.
- `Chapter 5:` presents the setup created to perform the analysis in PowerFLOW®. It includes description of the computational geometry, resolution and simulation parameters.
- `Chapter 6:` discusses the results of the grid resolution study. It also presents the validation of the computational data obtained by comparison against experimental data.
- `Chapter 7:` explains the results, through the analyses of the flow field and post-processing of acoustic data.
- `Chapter 8:` provides the conclusion to the thesis and summaries the key results and their significance. It concludes by discussing recommendations for the extension of this study.

2
Theoretical Background

This chapter provides the reader with a theoretical background and concepts that shall be used throughout the thesis. Section 2.1 introduces the reader to the fundamentals of propeller aerodynamics. In Section 2.2 the basic definition of sound, types of sound sources, and sound measurement techniques are discussed. Section 2.3 discusses the study of noise generated by fluid-solid interaction. The chapter ends with a review of acoustic analogies that are used for modeling aerodynamic noise sources.

2.1. Propeller aerodynamics

Literature classifies rotating blades into three main categories fans, propellers, and rotors. The mechanism by which these rotating blades produce thrust is the same. Rotors and fans differ from a propeller in terms of flow regime and number of blades, respectively. A rotor experiences radial inflow across its disc during a forward flight (similar to a helicopter, see Fig. 2.1a), whereas a propeller experience axial inflow. A propeller and a fan experience axial inflow condition, but fans have a significantly higher number of blades (8+) than propellers. It results in much higher wake interaction between the blades.

A propeller is a mechanical device consisting of a rotating shaft with blades attached to it. These blades are broad and angled, which help move a vehicle (typically an aircraft or marine vessel). The blades have the cross-section of an airfoil, and the propeller operates by using the torque generated by a power source to accelerate a mass of fluid, which produces thrust. Essentially a propeller can be re-imagined as a rotating wing that moves through an air mass by pushing it back and accelerating it, as shown in Fig. 2.1b. The airfoil theory describes how the acceleration of flow over an airfoil results in low pressure (suction side at the top) and high pressure (pressure side at the bottom) of the airfoil, producing lift. The airfoil theory, coupled with Newton's third law can explain how a propeller blade generates thrust.

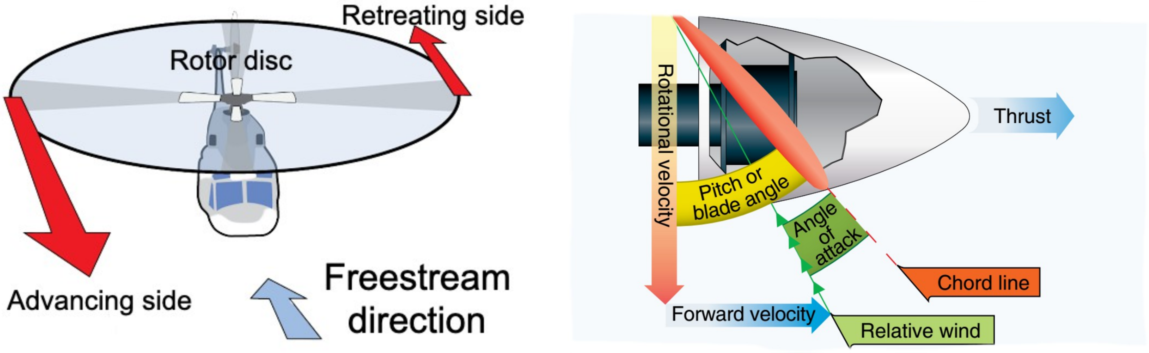

(a) Inflow condition for a rotor disc

(b) Propeller blade cross section and velocity diagram [25]

Figure 2.1: Propellers and rotors

The blades of a propeller rotate about their axis while moving forward. The AoA of a propeller blade element is defined as the angle at which the air (relative wind) strikes the propeller blade or the angle between relative airflow and the propeller chord line. As a result of this AoA, the air mass flowing over the propeller produces a net aerodynamic force known as the total reaction (TR) force, shown in Fig. 2.2b, which can be broken into its two key components lift (thrust) and drag. With an increase in AoA, lift (thrust in case of propeller) increases linearly (generally up to $15^o \pm 2^o$) and then drops. The drop in lift is due to the stalling of the airfoil. The drag force keeps increasing exponentially with increasing AoA. Hence for fixed pitch propellers, there is an optimum AoA at which the efficiency is the highest, while variable pitch, propellers that can adjust blade angle in flight, change blade angle depending on the flight phase, shown in Fig. 2.3. A variable pitch mechanism, because of its weight and mechanical complexity, is not suitable for small UAVs. UAV propeller designers optimize the propellers for a particular flight phase and AoA, resulting in reduced efficiency for the propellers in off-design conditions.

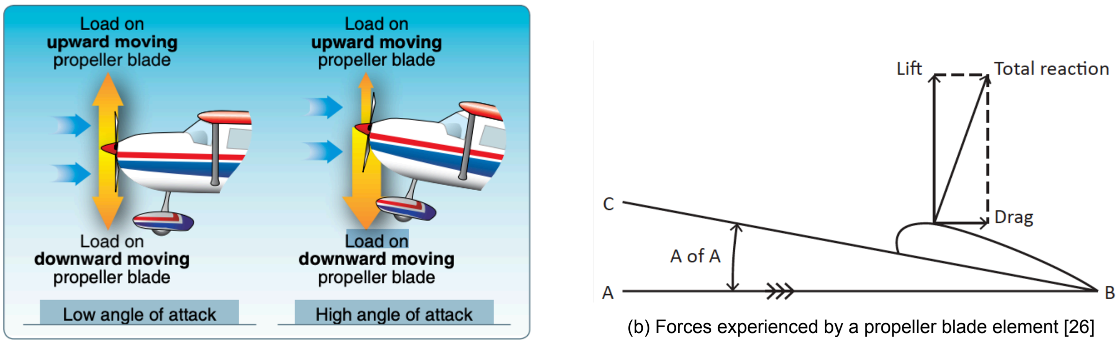

(a) Uneven loading caused at the propeller disc due to AoA [25]

(b) Forces experienced by a propeller blade element [26]

Figure 2.2: Force experience by a propeller at an AoA

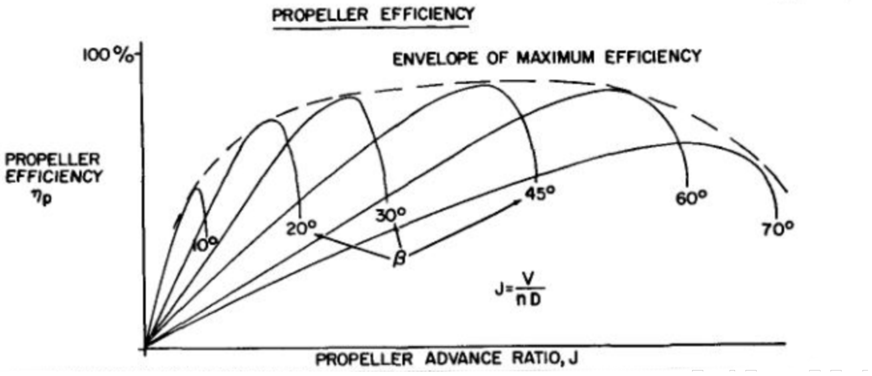

Figure 2.3: Change in Propeller efficiency vs advance ratio at specific blade AoA [2]

During the cruise phase, propellers are at a shallow (or 0^o) AoA resulting in axial inflow condition and steady disc loading. The new generation of PAVs and UAVs feature electric motors and novel tilt-rotor mechanisms, along with mission profiles that include transitions from vertical to horizontal flight paths (and vice-versa). These propellers operate at a wide range of AoA and experience non-axial inflow conditions. The non-axial inflow results in the variation of resultant velocity experienced by the propeller blade at a different azimuthal position (Ψ), resulting in the change of local blade AoA around the propeller plane. As a propeller has a similar operating principle to a wing, changes in AoA result in variation of the net aerodynamic forces experienced by the propeller, resulting in asymmetric loading of the propeller disc, shown in Fig. 2.2a.

2.2. Sound

This section introduces the reader to the properties and sources of sound and the basics of sound measurement techniques.

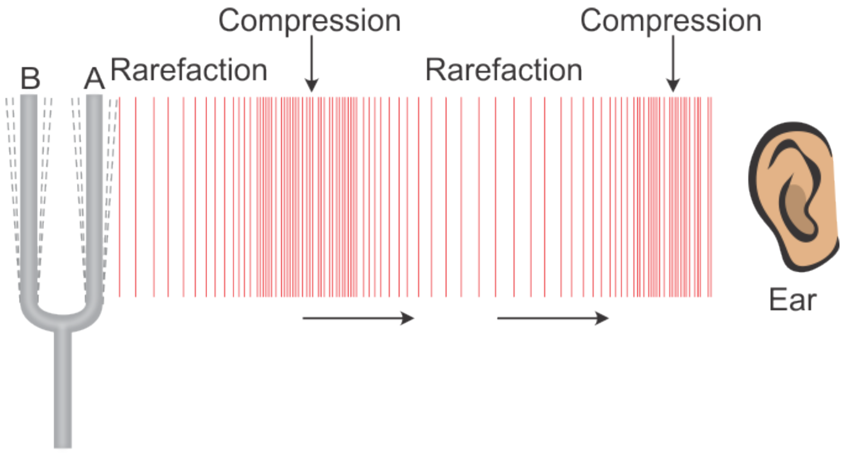

Figure 2.4: Compression and expansion of air due to propagation of sound waves [3]

Sound is a mechanical wave (longitudinal wave) that propagates through a medium (solid, liquid, or gas) in the form of isentropic pressure fluctuation. It creates a region of compression and expansion (high/low pressure) in its direction of propagation, as shown in Fig. 2.4. The rate (per sec) of compression and expansion determines the frequency of a particular sound wave. The audible frequency range for humans lies in the frequency band of 20-20,000 Hz. The speed (c) at which the fluctuation travels through a medium (ideal gas) is given by:

$$c = \sqrt{\frac{\gamma R^{*} T}{\text{mol}}} \tag{2.1}$$

where γ is the adiabatic index (1.4 at 0 °C, for air), R^{*} is the universal gas constant (8.314 $\text{J mol}^{-1}\,\text{K}^{-1}$), T is the absolute temperature (K), and mol is the molar mass of the gas. This means that the speed of sound is dependent upon the physical properties of the medium through which it travels, as seen in Table 2.1.

Medium	**Speed of Sound (m/sec)**	**Temperature (K)**
Air	331	273
Helium	965	273
Air	343	293
Fresh Water	1,480	293
Lead	1,960	–
Glass	5,640	–

Table 2.1: Speed of sound in different mediums [19]

The terms sound and noise are used interchangeably, however, there is a difference between them. Sound can be desirable or undesirable, like the sound produced by a speaker or a passing aircraft. Noise is an unwanted sound, which may cause annoyance or physical discomfort.

2.2.1. Sources of sound

Sources of sound have diverse sound generation mechanisms, directivity, frequency spectra, and radiation efficiency. Most sound sources consist of a mixture of elementary source types, which is dependent upon the sound generation mechanism. The three fundamental source types that make up most of the sound sources are acoustic monopole, dipole, and quadrupole, see Fig. 2.5. This section explains the different characteristics of these elementary sound sources.

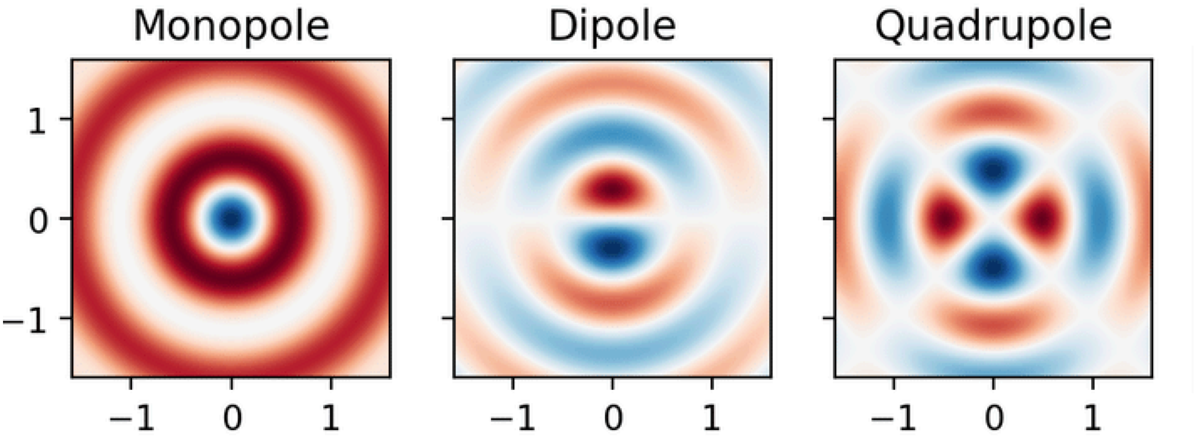

Figure 2.5: Radiation pattern of different sound sources [4]

- **Monopole:** A monopole is the building block for all the other elementary sources of noise, such as dipoles and quadrupoles. The dimensions of monopole sources are typically much smaller than the radiated sound wavelength. The pressure amplitude radiated by a monopole in the far-field is given by:

  $$|p(x,\phi,t)| = \frac{S\rho ck}{4\pi x} \tag{2.2}$$

  where, k is the wavenumber given by $\frac{2\pi}{\lambda}$ or $\frac{f}{c}$, S is the source strength, and x is the distance between the source and the observer.

  The pressure amplitude for a point source does not depend on the radiation angle (ϕ); hence a monopole radiates sound equally in all directions. The sound power (Π) radiated by a monopole source is given by [27]:

  $$\Pi = \frac{S^2\rho ck^2}{8\pi} \tag{2.3}$$

  as $k = \frac{f}{c}$, the above equation can also be written as $\Pi \sim f^2$, meaning that the sound power radiated by a monopole varies with the square of the frequency.

- **Dipole:** A dipole is made up of two monopoles of equal strength but opposite phases. The distance between the two monopoles in a dipole satisfies $kd << 1$, where d is the distance between two monopoles. The pressure amplitude of a dipole radiated in the far-field is given as

  $$|p(x,\phi,t)| = \underbrace{\frac{S\rho ck}{4\pi x}}_{\text{Source term}} *kd* \underbrace{cos\phi}_{\text{Directivity}} \tag{2.4}$$

  where kd relates the radiated wavelength to the distance between two monopoles.

  The directivity function depends on ϕ, meaning that the sound is not radiated equally in all directions (max when $\phi = 0^o$ and 180^o). The sound power radiated by a dipole varies with the 4^{th} power of frequency ($\Pi \sim f^4$), meaning that a monopole source is more efficient in radiating low-frequency sound with similar source strength than a dipole source.

- **Quadrupole:** A quadrupole source consists of two dipoles of equal strengths but opposite phase or four monopoles with alternating phase, as seen in Fig. 2.5. The monopoles are separated by a distance of d_h and d_v (horizontal and vertical). The separation is smaller than the wavelength of the sound produced. The pressure amplitude produced by a quadrupole source in the far-field is given by:

$$|p(x,\phi,t)| = \underbrace{\frac{S\rho ck}{4\pi x}}_{\text{Source term}} *4k^2 d_h d_v * \underbrace{cos\phi sin\phi}_{\text{Directivity}} \tag{2.5}$$

The directivity is such that there are four angles (ϕ) of high noise radiation and four shadow regions. The sound power radiated by a quadrupole varies with the 6^{th} power of frequency. For a source of similar strength, a quadrupole is the least efficient radiator for low-frequency noise.

2.2.2. Measurement of sound

Measuring a source of sound helps in quantifying the pressure fluctuation produced by it. Sound waves with pressure fluctuation in the range of $20\mu\ Pa$ to $2,000\ Pa$ fall within the audible band of an average human and are of particular interest for most acoustic studies. Given the range of pressure fluctuation, it is difficult to capture it on a linear scale against a standard atmospheric pressure of $101,325\ Pa$. Hence, a logarithm scale (decibel dB) is used to measure sound, and the most common quantity used to describe it is sound pressure level (SPL). It is defined as:

$$SPL = 10 * log_{10}\left(\frac{p_{rms}}{p_{ref}}\right)^2 \tag{2.6}$$

where p_{rms} is the root mean square of the pressure fluctuation and p_{ref} is the reference pressure. It is $2 \times 10^{-5}\ Pa$ for air and is the minimum threshold of human hearing, as shown in Fig. 2.6.

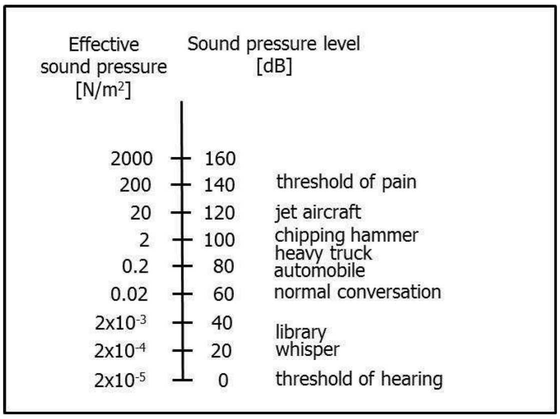

Figure 2.6: Effective Sound pressure and corresponding SPL in decibel scale [5]

A sound signal consists of multiple frequencies. Human ears, similar to human eyes, are more sensitive to a specific range of frequency. The International Electro-Technical Commission (IEC) defines a family of curves that provide an independent standardized way of measuring sound perceived by humans, see Fig. 2.7. It applies a certain weight to the measured SPL as per their frequency and is defined under IEC 61672:2003 as:

- **A** - weighting is most commonly used for measuring environmental and industrial noise, as well as in the assessment of potential hearing damage and other noise health effect at all sound levels.
- **B, D** - weightings are no longer described in IEC 61672:2003, but their frequency response can be found in older IEC 60651. It is interesting to note that D-frequency-weighting was developed specifically for high-level aircraft noise under the IEC 537 measurement standard.
- **C** - weighting is in use by many sound level meters, and their fitting is mandated (at least for testing purpose) to precision (class one) sound level meters.

Applying Fourier transform converts a pressure signal in the time domain to acoustic spectra in the frequency domain. A noise spectrum represents the contribution of different frequencies to the overall sound pressure level (OASPL). OASPL is used to quantify the total energy contained in a noise spectrum. Performing a Fourier transform on a pressure signal reveals its characteristics (tonal or

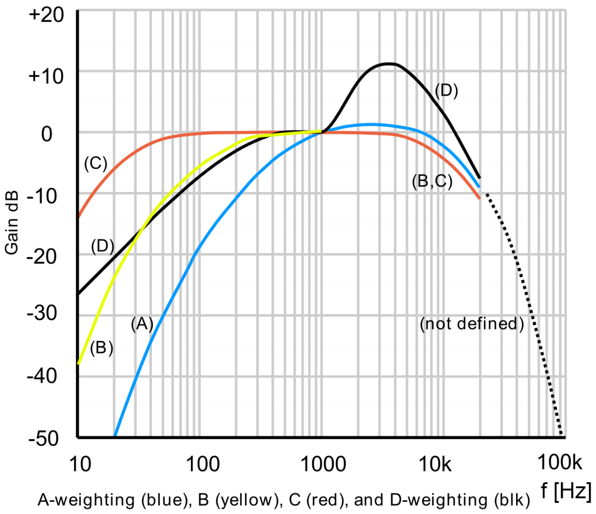

Figure 2.7: Weighting graph for sound pressure levels [6]

broadband) and helps detect its dominant features. Tonal noise can be defined as a discrete frequency noise characterized by spectral peaks at specific frequencies, as shown in Fig. 2.8. Broadband noise, also know as wideband noise, is a noise whose energy is distributed over a wide range of frequencies with no distinct peaks in the spectrum.

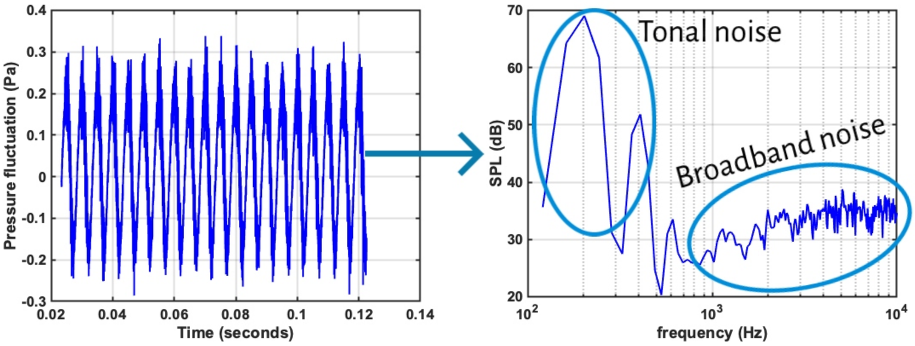

Figure 2.8: Converting pressure signal from a propeller analysis to power spectrum

2.3. Aeroacoustics

Aeroacoustic is a discipline that combines fluid mechanics with classical acoustics to study the noise produced by an aerodynamic source. It analyses and quantifies noise generated due to unsteady fluid motion and interaction of surfaces with fluid in motion, resulting in fluctuating aerodynamic forces. The characteristics of noise generated by a propeller are discussed in Section 2.3.1 and the broadband noise generation mechanism of an airfoil is discussed in Section 2.3.2.

2.3.1. Propeller noise

Noise has been one of the main factors limiting the widespread use of propeller-driven aircraft. This section introduces the reader to the characteristics of noise generated by a propeller and briefly explains the mechanism behind them.

Propeller noise is classified into tonal noise and broadband noise, see Fig. 2.8. Pressure fluctuations produced by the rotation of a propeller blade in a fluid medium consist of tonal and broadband components. Fig. 2.9 shows the pressure fluctuation produced by a three-bladed propeller in one rotation. The top left corner of the figure represents the tonal component of the pressure signal. The three distinct pressure peaks observed in the signal repeat themselves per rotation and are responsible for the tonal peak observed at lower frequencies. The frequencies at which these tonal peaks appear are multiples of the blade passing frequency (BPF) of the propeller, which is defined as:

$$\textbf{BPF} = n * \mathrm{N} \tag{2.7}$$

where N is the number of blades on the propeller and n is the number of rotations completed by the propeller in one second. Fig. 2.8 shows the power spectrum for a two-bladed propeller at $6,000$ RPM. The power spectrum has two distinct tonal peaks at $200\ Hz$ and $400\ Hz$, meaning that the BPF of the propeller is $200\ Hz$. The tonal noise in a propeller is produced due to [28]:

- **Blade loading:** It is the noise generated as a by-product of the thrust produced by the propeller. Like an airfoil, the pressure difference between the pressure and suction side of the propeller blade element results in thrust. When the rotating pressure field is observed from a fixed point, it appears as an oscillating pressure filed on the propeller blade. The frequency of the oscillation is determined by the propeller blade passing frequency. The chordwise pressure distribution on the blade determines the waveform of the oscillating pressure.
- **Blade thickness:** Rotation of the propeller blade results in the introduction and removal of mass at each element near the propeller disc. The rate of which is dependent on the blade profile, incidence angle, and rotation speed. At low-speeds, the noise produced due to the blade thickness is lower than that produced by blade loading. At high-speed thickness, noise assumes equal importance as loading noise [28].

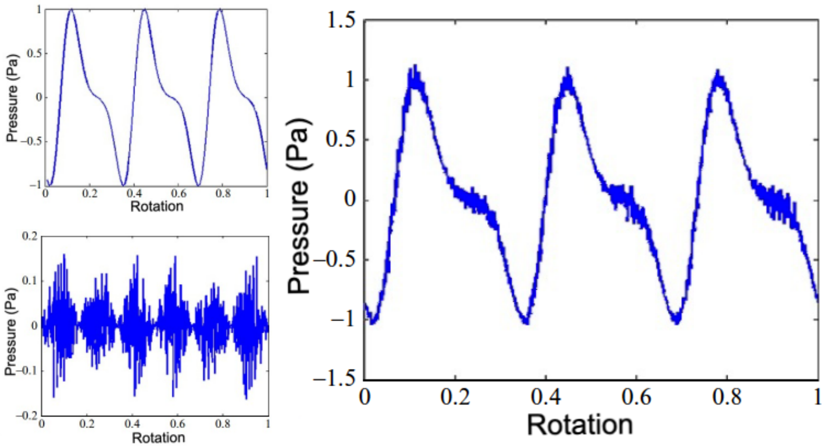

Figure 2.9: Pressure signal produced by a propeller; Tonal component (top left), Broadband component (bottom left), and total pressure signal (right); adapted from [7]

The broadband component of propeller noise is a random, non-periodic signal caused by the unsteady pressure field on the propeller blade. The mechanisms generating these pressure fields include shedding of the vortices from the propeller tip and trailing edge, turbulent inflow over the propeller blade, etc., and have been discussed in Section 2.3.2. The frequency at which these vortices are shed varies along the propeller blade span, resulting in a wide range of frequencies. It results in the production of broadband noise, as seen in Fig. 2.8.

2.3.2. Airfoil noise generation mechanism

The study of airfoil self-noise has been motivated by its contribution to the broadband component of the rotor, propeller, wind turbine, and airframe noise [29]. It can be classified into five subtypes: laminar boundary layer instability noise, turbulent boundary layer trailing edge noise, trailing edge bluntness noise, separation and stall noise, and tip noise. The noise generation mechanism is dependent on the inflow conditions, Reynolds number, and the shape/construction of the airfoil. The mechanisms that are of particular interest for this thesis are:

- **Turbulent boundary layer trailing edge noise:** Turbulent flows result in the downstream convection of eddies (unsteady pressure fluctuation) of different scales and energy. Upon reaching the trailing edge of an airfoil, these eddies experience a sudden change in pressure and acoustic impedance and scatter as broadband noise. It is a significant contributor to the noise produced by propellers and wind turbines [30].

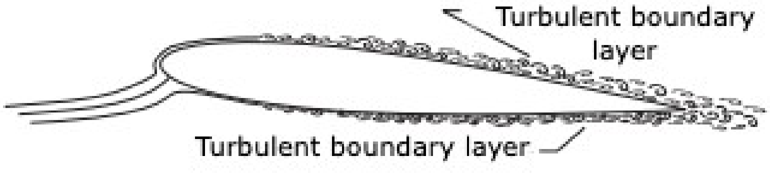

Figure 2.10: Turbulent boundary layer trailing edge noise [8]

- **Separation and stall noise:** At high AoA, depending on Reynolds number and airfoil characteristics, flow separation may occur on the suction side of the airfoil. Flow separation at the suction side results in unsteady flow and generation of tonal humps in the broadband spectrum due to vortex shedding [31]. It can be avoided by tripping the propeller blades [32].

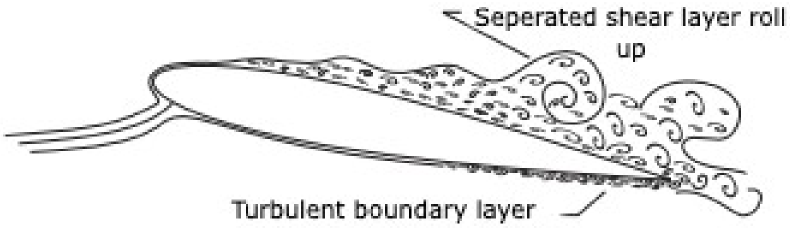

Figure 2.11: Separation and stall noise [8]

2.4. Aeroacoustic analogies

An acoustic analogy reduces the source of aeroacoustic noise into simple emitter types and decouples the noise generation mechanism from its pure propagation. It is achieved by rearranging the equations governing the acoustic field such that the field variables (wave operator) are on the left-hand side of the equation and the source quantities to the acoustic field (source part) on the right-hand side. Doing so enables the use of CFD/CAA simulations to computationally predict noise in the far-field without the need for a large simulation domain with high resolution. The three most commonly used acoustics analogies were developed by Lighthill, an extension to Lighthill's analogy by Curle, and Ffowcs Williams & Hawkings. Sections 2.4.1 and 2.4.2 explains the characteristics of these analogies and their relevance for the present study, however, before expanding on the analogies the section discusses the basic equations defining linearised acoustic wave propagation and generation.

Consider a medium with a stationary flow such that the average flow properties are uniform throughout the flow domain. As an acoustic wave propagates through the medium, it becomes the only source of pressure and velocity fluctuation. For a sound wave traveling isentropically through the medium, the relation between pressure and density perturbation is given as:

$$p' = \rho' c_o^2 \quad \text{where} \quad c_o^2 = \left(\frac{\partial p}{\partial \rho}\right)_{isentropic} \tag{2.8}$$

By assuming that the acoustic wave results in small density perturbation (ρ') in the medium, $\rho' << \rho_o$ where ρ_o is the mean density, substituting it in the continuity equation gives:

$$\frac{\partial \rho'}{\partial t} + \rho_o \frac{\partial v_i}{\partial x_i} \approx 0 \tag{2.9}$$

where v_i is the velocity fluctuation induced by the acoustic wave.

Next, the momentum equation is modified by neglecting the effects of viscosity and applying a small perturbation assumption to it. The small perturbation assumption helps linearise the equation by ignoring all second-order terms, resulting in:

$$\rho_o \frac{\partial v_i}{\partial t} + \frac{\partial p'}{\partial x_i} \approx 0 \tag{2.10}$$

By combing the momentum and continuity equation, the linear homogeneous acoustic wave equation is obtained. It forms the base for all calculation in the field of linear acoustics and is given as [7]:

$$\frac{1}{c^2}\frac{\partial^2 p'}{\partial t^2} - \nabla^2 p' = 0 \tag{2.11}$$

where p' is the pressure fluctuations caused by the acoustic wave. In the linear homogeneous acoustic wave equation, the effect of external force (F), mass, and momentum injection are neglected, and the fluid domain is assumed to be stationary. It can not be used to describe an acoustic wave propagating from a source of sound or in a non-stationary medium.

A wave equation that includes the sound source is defined using an inhomogeneous wave equation. It is derived by rearranging the momentum and continuity equations. The process is similar to deriving the linearised homogeneous wave equation without neglecting the effect of external force (F), mass, and momentum injection. Which results in [33]:

$$\frac{1}{c^2}\frac{\partial^2 p'}{\partial t^2} - \nabla^2 p = \underbrace{\frac{\partial m}{\partial t}}_{\text{Monopole}} - \underbrace{\nabla . F}_{\text{Dipole}} \tag{2.12}$$

Eq. (2.11) and Eq. (2.12) are similar to each other, except for the monopole and dipole source terms on the right-hand side of the equation.

Monopole: A monopole source term represents the displacement of mass ($\frac{\partial m}{\partial t}$) in the system. As described in Section 2.2.1, such a source radiates noise equally in all directions. The sound produced by the displacement of air by a propeller is a monopole sound source.

Dipole: A dipole source represents the noise produced by the force exerted on the flow. The forces exerted by rotating propellers into the flow are an example of such a source.

2.4.1. Lighthill's acoustic analogy

Lighthill's acoustic analogy provides the theory for the sound generated by turbulence and helps in identifying the source of sound in an arbitrary unsteady flow [7]. Based on exact equations of fluid flow, Lighthill's equations make no assumptions relating to compressibility effects and is given as [34, 35]:

$$\frac{\partial^2 \rho'}{\partial t^2} - c^2 \frac{\partial^2 \rho'}{\partial x_i^2} = \frac{\partial^2 T_{ij}}{\partial x_i \partial x_j} \tag{2.13}$$

Where T_{ij} is the Lighthill's stress tensor and is given by:

$$T_{ij} = \rho u_i u_j + (p - c^2 \rho)\delta_{ij} - \tau_{ij} \tag{2.14}$$

The LHS of the equation describes the acoustic wave propagation in a uniform medium, where $\rho' = \frac{(p - p_\infty)}{c^2}$ is the dependent variable and c is the speed of sound in the stationary medium. The RHS describes the source term consisting of all the effects that generate the wave. The Lighthill's stress tensor T_{ij} in is defined as:

- $\rho u_i u_j$: is the Reynolds stress tensor.
- $(p - c^2\rho)\delta_{ij}$: represents the excess momentum transfer by pressure and can be ignored in an isothermal, incompressible flow [36].
- τ_{ij}: is the viscous stress tensor and can be ignored for high Reynolds number flow.

A closer analysis of the source term reveals a second-order spatial derivative, making it a quadrupole source of the sound [37]. It also means that the source term only models free turbulence and does not account for the effect of moving boundaries or surfaces present in the flow. The presence of a surface/solid body in the flow influences how sound waves are produced and radiated in the sound field.

Not being able to account for the presence of a surface was a limitation of Lighthill's analogy. Curle [38] in 1955 extended Lighthill's analogy to include the effects of a surface/solid body in the flow. Curle's analogy is relatively advanced to Lighthill's analogy, however, it assumes the surface to be stationary in the fluid. The noise produced by propellers is due to moving surfaces, as result, both these analogies are unsuitable for analyzing the acoustic field of rotating propellers.

2.4.2. Ffowcs-Williams and Hawkings (FWH) analogy

FWH [39] extended Lighthill's and Curle's analogy in 1969 to include moving surfaces. It redefines the pressure, density, and velocity variables in terms of generalized derivatives such as the Heaviside step function H_S and substitutes these variables into the continuity and momentum equations. The equations are solved to obtain a wave equation in terms of the new variables. It is the FWH equation, given as:

$$\begin{aligned}\rho'(x,t)c_\infty^2 H_s = & \frac{\partial^2}{\partial x_i \partial x_j}\int_{V_o}\left[\frac{T_{ij}}{4\pi r\,|1-M_r|}\right]_{\tau=\tau^*} dV(z) \\ & - \frac{\partial}{\partial x_i}\int_{S_o}\left[\frac{\left(\rho v_i\left(v_j - V_j\right) + p_{ij}\right) n_j}{4\pi r\,|1-M_r|}\right]_{\tau=\tau^*} dS \\ & + \frac{\partial}{\partial t}\int_{S_o}\left[\frac{\left(\rho v_j - \rho' V_j\right) n_j}{4\pi r\,|1-M_r|}\right]_{\tau=\tau^*} dS\end{aligned} \tag{2.15}$$

The modification makes the FWH analogy suitable for performing analysis for propeller noise. The $\frac{1}{(1-M_r)}$ term physically signifies the impact of motion of the source on its time history. The significance of the other terms on the RHS are as follows [7]:

- **Quadrupole term:** it is defined as the volume source term and its strength depends upon T_{ij}. It consists of sound radiated by turbulence and flows distortion due to shock waves. At low speeds, this term is of negligible importance.
- **Dipole term:** It is the second term of the equation and is controlled by surface loading p_{ij}.
- **Monopole term:** It is a volume displacement source and is dependent upon the blade surface velocity and the density at the observer.

FWH analogy can model noise produced by moving sources, making it the most suitable analogy for modeling propeller noise. PowerFLOW® uses the FWH analogy for computing the aeroacoustic properties. The way an FWH analogy works in a CAA setup is [40]:

1. The acoustic pressure fluctuations produced by the source are captured inside a control surface using a fine mesh. It is done by placing permeable or solid integrating surfaces in the control volume, details of which have been discussed in Section 4.3.1.
2. The acoustic reciprocity theorem is then used to collect and find equivalent sources (monopoles, dipoles, and quadrupoles) to set at the control surface.
3. Linear acoustic propagation schemes are then used to calculate the noise in the far-field.

3

Literature Review

This chapter reviews the research done in the field of propeller aerodynamics and aeroacoustics. Part one, Section 3.1, of this chapter recapitulates the research done on propellers operating at high Reynolds numbers (Re) and the impact of inflow angle on their characteristics. It is achieved by discussing the various experimental, analytical, and numerical techniques used to analyze propeller characteristics. Part two, Section 3.2, of this chapter, reviews the most recent research on propellers operating at low Reynolds number. The section is divided into an aerodynamic and an acoustics section. They address the progress made in the field and identify the research gaps. The final part, Section 3.3, of this chapter, presents the research question that the author aims to answer through this thesis.

3.1. Fundamental research

Propellers preceded all means of powering an aircraft by several decades and saw significant improvement in their performance between the 1930s & 40s. It was during this period Gutin [41] started performing theoretical work in understanding the sound field produced by a rotating propeller. The introduction of jet engines in the 1950s saw the propellers fall out of favor for a less efficient though faster means of propulsion, causing a slump in propeller-related research. In the 1970s, however, a steep rise in fuel cost shifted the attention back to efficiency spurring propeller-related research.

Researchers were concerned about the increase in annoyance due to low flying aircraft powered by propellers. The projected rise in the use of such aircraft was a big motivation to develop noise abatement techniques. By 1970, analytical studies recognized blade thickness and loading, tip vortex, and trailing edge vortex as the primary sources of aerodynamic noise on a propeller. Researchers were able to identify that factors such as the number of blades, flow velocity, flow direction play a vital role in determining the acoustic characteristics of a propeller [28]. Quantification, detailed analysis, and validation of these theoretical results were limited by the experimental and computational resources available at the time.

Post-1970s the renewed interest in propeller-powered aircraft lead to the development of advanced turboprops and prop fans. These developments were supported by advancements in experimental and computational research, enabling researchers to validate the analytical models and explain propeller noise radiation and generation mechanism. One such model is the helicoidal surface theory developed by Hanson [42] in 1980. The analytical model used a frequency domain analysis of the pressure field to show how blade thickness, chord length, sweep, and the airfoil section shape influenced noise radiation. The theoretical results were compared against experimental data from a supersonic tip speed propeller at a flight Mach number of 0.32 and showed good agreement. The model assumed the propeller to be in a uniform axial inflow condition. However, it paved the way for future research in non-axial inflow conditions by providing a way to account for variation in blade geometry on far-filed noise.

In the mid-1980s, the International Civil Aviation Organization (ICAO) introduced a new procedure in the noise certification of propeller-driven aircraft. The new regulations required the aircraft noise to be measured during the cruise, take-off, and approach flight phase. The propeller operates at an AoA during take-off and approach conditions. The non-axial inflow conditions result in the variation of aerodynamic as well as acoustic characteristics of the propeller. The fundamental cause and mechanisms of which have been discussed in the following sections.

3.1.1. Radial directivity

Operating under non-axial inflow propeller blade experiences periodic variation in the magnitude of inflow velocity and local blade AoA. The accompanying variation in the helical propeller tip Mach number (M_{HT}) and its AoA (α_L), wrt. to 0^o AoA, can be expressed as a function of its azimuthal angle (Ψ), advance ratio (J), and propeller disc AoA (α), and is given as [9]:

$$\frac{M_{HT}(\alpha,\Psi)}{M_{HT}(\alpha=0)} = \sqrt{1+\frac{2J\ \mathrm{sin}\alpha\ \mathrm{sin}\Psi}{1+J^2}} \tag{3.1}$$

$$\Delta\alpha_L = tan^{-1}\left[\frac{J(1-\mathrm{cos}\alpha+J\ \mathrm{sin}\alpha\ \mathrm{sin}\Psi)}{1+J^2\ \mathrm{cos}\alpha+J\ \mathrm{sin}\alpha\ \mathrm{sin}\Psi}\right] \tag{3.2}$$

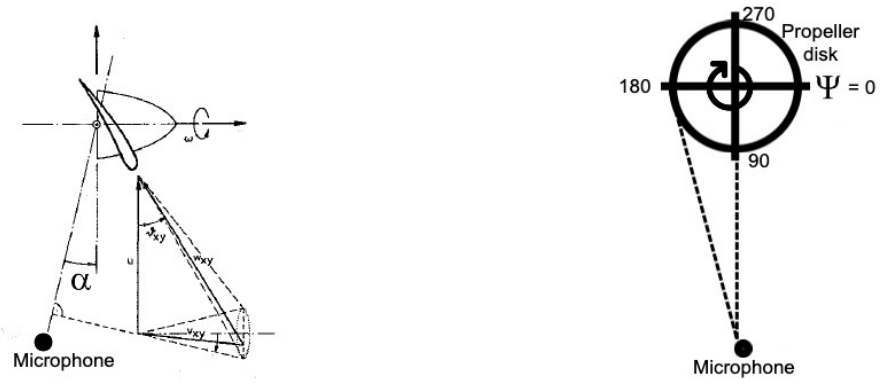

(a) Side view of propeller microphone setup

(b) Front view of propeller microphone setup

Figure 3.1: Visualisation of propeller disc AoA; adapted from [9]

Based on Eq. (3.1) and Eq. (3.2), it can be seen that the maximum value wrt. 0^o AoA will be attained when $\Psi = 90^o$ (or 270^o depending on how AoA and Ψ are defined). Experiments performed by Dobrzynski et al. [9] found that for a microphone in the propeller plane the pressure amplitude is governed by the pressure wave being produced by the propeller blade advancing in the direction of the microphone. From theoretical knowledge, it is deduced that the variation in the helical tip Mach number (M_{HT}) and local AoA (α_L) will result in variation of the pressure amplitude produced by the propeller blade. The variation in pressure amplitude will cause a change in the SPL calculated at the microphone location and produce asymmetry in circumferential noise directivity.

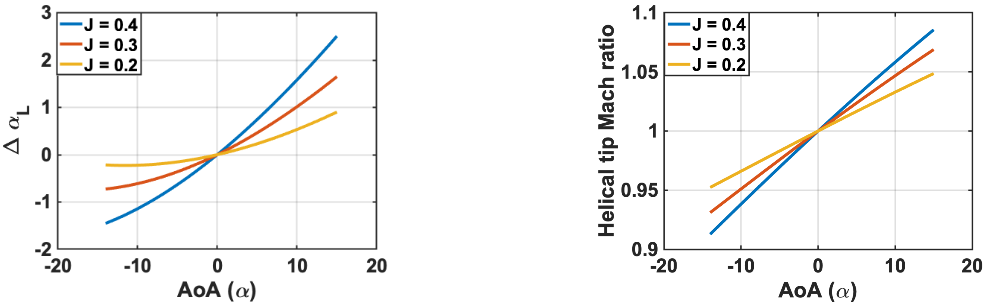

(a) Variation in local AoA (α_L)

(b) Variation in helical tip Mach number

Figure 3.2: Variation in propeller blade properties with AoA (α) at $\Psi = 90^o$

Fig. 3.2 graphically represents the variation in α_L and M_{TH} with AoA for different advancing ratio (J). It can be seen that J of the propeller has a significant impact on $\Delta\alpha_L$, doubling the advanced ratio from

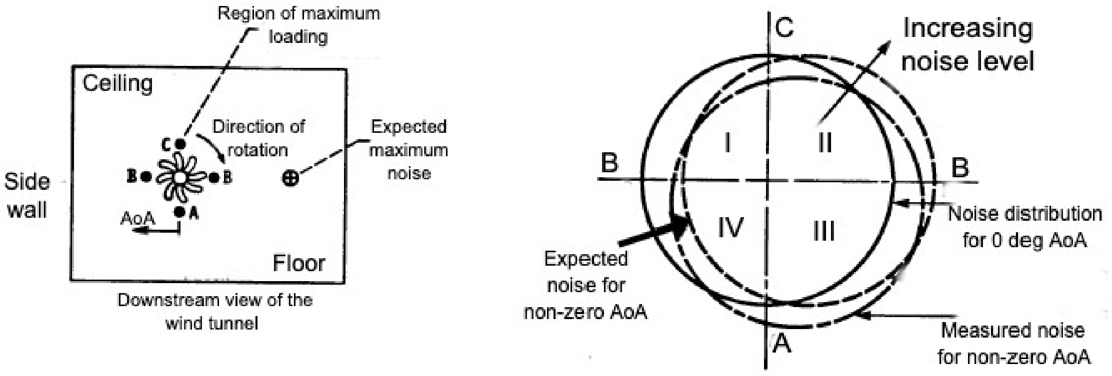

(a) Layout of the wind tunnel setup

(b) Radial noise directivity

Figure 3.3: Experimental setup and radial noise directivity [10]

$J = 0.2$ to 0.4 triples the value of Δ from 0.91^o to 2.50^o at $= 15^o$. The change in the helical tip Mach ratio is relatively modest with changes in J.

Woodward [10] in 1987 conducted experiments on an eight-bladed SR-7A (see Appendix A for more technical details) at a freestream Mach number of 0.2 at non-zero AoA to simulate takeoff/landing conditions. Citing the theory discussed above, the author predicted changes in the radial noise field. Woodward associates the variation in $\Delta\alpha_L$ with AoA to the changes in blade loading, which affects the noise generation. The experimentally measured noise field showed asymmetry in the radial noise field with non-zero AoA, as seen in Fig. 3.3b. However, a closer look at the result shows that the asymmetry is not exactly as predicted by the theory. For non-zero AoA, the measured noise peak is leaning more into the 3^{rd} quadrant than expected (phase lead). This variation can be attributed to unsteady inflow conditions experienced by the propeller blades as they operate in the wake of other blades. The high number of propeller blades at non-zero AoA in a relatively low freestream Mach number could create such a condition. By 1989 Whitefield et al. [11] recognized that propellers (especially with a large number of blades) experience a phase lag/lead effect. The effect is due to unsteady loading caused by large-scale low-frequency distortion in the flow. The distortions are a consequence of installation effect, non-zero AoA, etc. As a result, a new theory using a quasi-steady approach to model the effect of unsteady forces was developed. The phase effect is calculated from the linearized 2D gust theory. Fig. 3.4 shows the impact of including these effects into radial noise calculations. In Fig. 3.4a, the old theory shows the maximum variation to be around $\Psi = 90^o$ including the phase effect (Fig. 3.4b) shifts it closer to $\Psi = 120^o$. The results showed an encouraging match with experimental data and help to understand the mechanism involved in radial directivity of propeller noise.

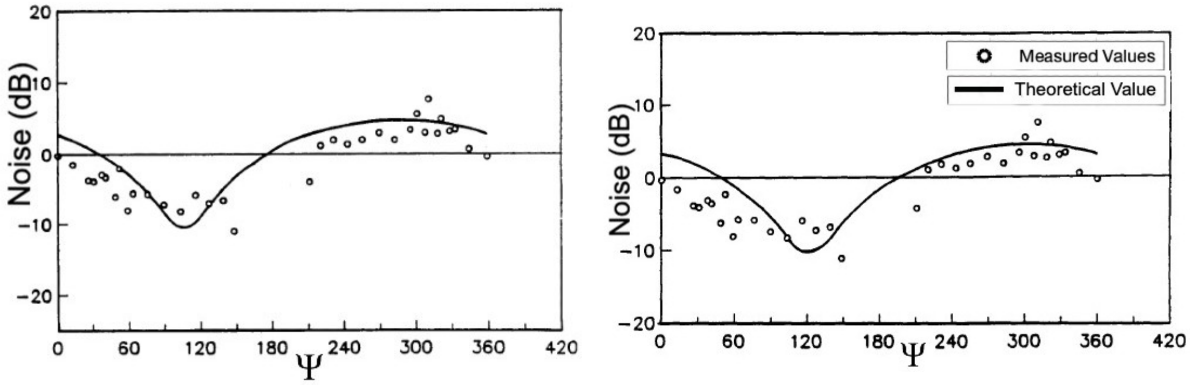

(a) Radial directivity with old theory

(b) Radial directivity with new theory

Figure 3.4: Radial noise directivity at 1^{st} BPF of a 4 bladed SR-2 propeller at 9^o AoA wrt. 0^o base line; Operating condition $M_{tip} = 0.4$ freestream velocity $30\ m/sec$ [11]

Based on the above theories and experiments, Mani [12] in 1990 developed an improved model for the prediction of the 1^{st} BPF noise produced by a propeller. He proposed a new mechanism of noise radiation for high-tip speed, heavily loaded propellers, where he suggested a change in the radiative efficiency of steady loading/thickness noise. However, it is not relevant for this study, and only results from low tip speed propellers are discussed here. To calculate the pressure amplitude in the far-field Mani, assumed the sound field produced by steady blade loading/thickness to be unchanged with AoA. To account for the influence of AoA, a once per revolution unsteady load was introduced into the calculation, adding additional noise at BPF. By combing the two noise fields due to steady and unsteady loads, a new non-axisymmetric noise field is obtained. A key takeaway from the new theory is the relationship between tip Mach number (M_T) and relative change in noise with a change in AoA in the radial direction. At BPF the ratio of unsteady to steady loading scales as:

$$\frac{\mathrm{J}_{\mathrm{N}-1}(\mathrm{N}M_T)}{\mathrm{J}_{\mathrm{N}}(\mathrm{N}M_T)} \tag{3.3}$$

where J is the Bessel function of the first kind and N is the number of blades. From Eq. (3.3) it can be reasoned that with an increasing value of M_T (for subsonic range), the ratio would diminish. The diminishing ratio would result in a lower variation of noise radiation in the radial plane with AoA, as seen in Fig. 3.5.

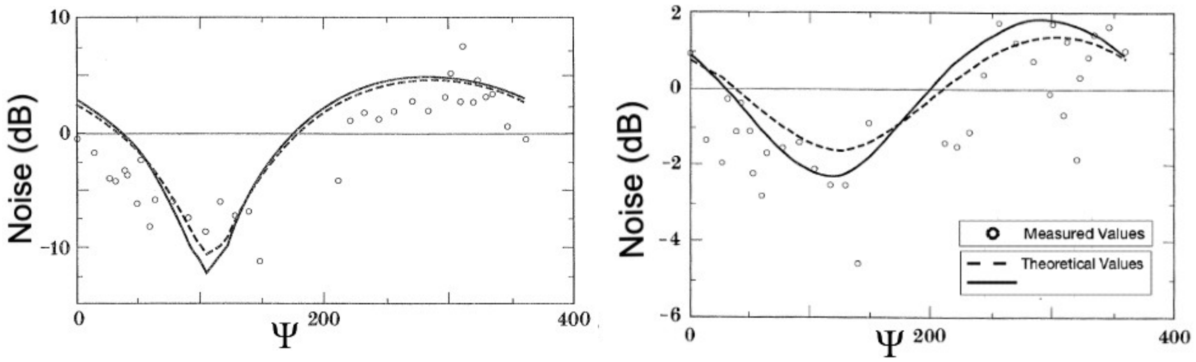

(a) Tip Mach number ($M_T = 0.4$)

(b) Tip Mach number ($M_T = 0.66$)

Figure 3.5: Radial noise directivity at 1^{st} BPF of a 4 bladed SR-2 propeller at 9^o AoA wrt. 0^o base line at a freestream velocity $30\ m/sec$ [12]

3.1.2. Axial directivity

The axial directivity of noise defines the characteristics of propeller noise along its axis of rotation. Understanding the axial directivity of propeller noise is vital in understanding the on-ground noise footprint of a propeller. This section shall combine the leanings from Section 2.2.1 and Section 2.3.1 to understand the axial directivity pattern of broadband and tonal propeller noise. It then discusses relevant research in the field to understand the impact of non-axial inflow conditions on axial directivity.

Fig. 3.6 shows us the directivity pattern (dipoles) for steady loading noise and unsteady loading noise in the axial direction. The directivity pattern shows a 90^o phase shift between loading and vortex noise which is due to a difference in the noise-generating mechanism of these two sources. Steady loading noise is generated in the propeller plane due to blade rotation. Unsteady loading noise is produced by the fluctuation of forces on the blade surface (normal to propeller plane). Keeping that in mind from Eq. (2.4) the directivity pattern of these two sources can be calculated to be maximum in the plane of rotation (for steady loading noise) and along the propeller axis (for unsteady loading noise).

By measuring noise of scaled model high-speed propeller at simulated takeoff/approach (-10^0 to $+15^o$) conditions, Woodward [10] was able to understand the trends in axial directivity with AoA. He obtained the measurements by placing a translating microphone in the NASA Lewis anechoic wind tunnel to simulate an observer location directly below the propeller during a level flyover, see Fig. 3.7a. The microphone measured the acoustic field between 25^o to 140^o (θ) below the propeller axis (90^o being directly underneath the propeller).

Taking measurements in axial inflow condition at BPF and 2x BPF, Woodward noticed that the maximum noise occurred directly below the propeller ($\theta = 90^o$), Fig. 3.7b. The noise level decreases

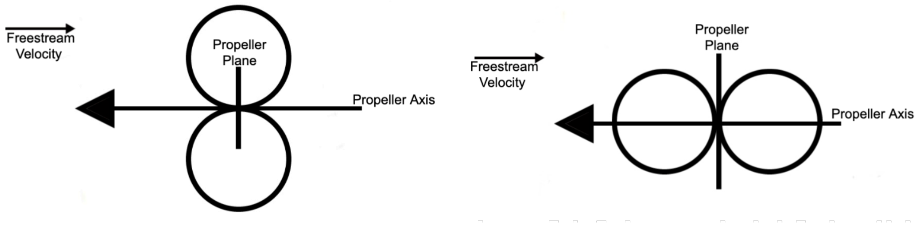

(a) Directivity pattern of steady loading noise on the propeller plane

(b) Directivity pattern of unsteady loading on the propeller plane

Figure 3.6: Propeller noise directivity pattern for axial inflow condition

on both sides of (θ = 90^o). The side lobes occur due to reflection from the tunnel wall and interference from the microphone array. These side lobes are not indicative of the axial directivity of propeller noise. The experimental results, therefore, show the same directivity trends as the theory discussed above. Measurements with changing AoA showed that the noise levels increase below the propeller with positive AoA, see Fig. 3.8. The difference in noise levels can be as high as 10 dB directly below the propeller when the AoA changes from 0 to 15^o.

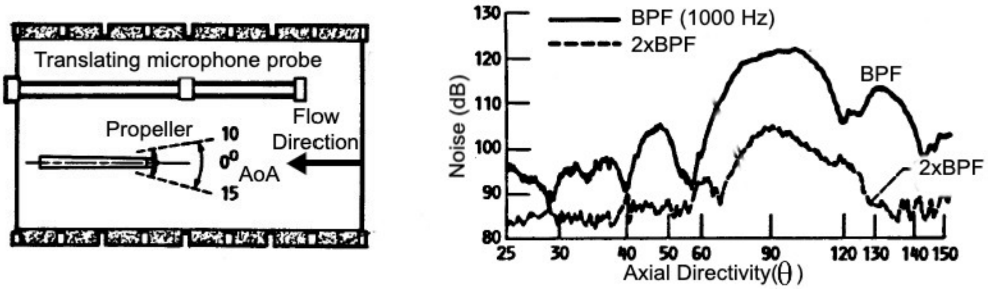

(a) Top view of the experimental setup [10]

(b) Axial Directivity at 0^o AoA

Figure 3.7: Experimental setup and propeller noise directivity at 0^o AoA [10]

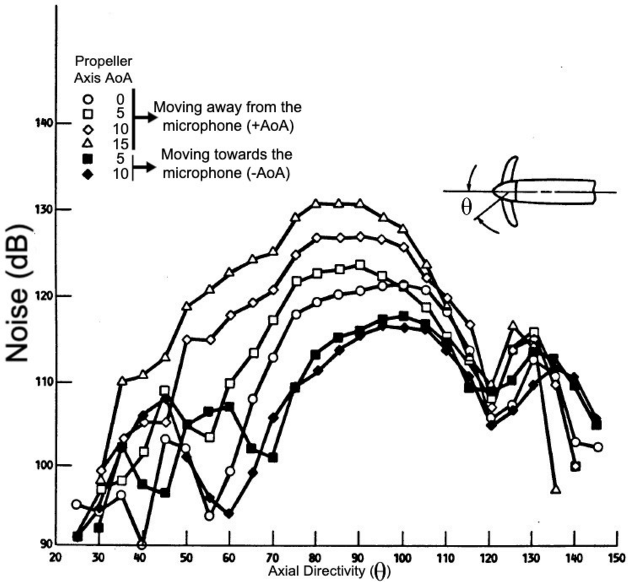

Figure 3.8: Effect of AoA on axial directivity of BPF [10]

Padula [43] in 1985, conducted further experimental research on the variation in axial directivity with AoA. He conducted experiments on high ($M_T = 0.76$) and low ($M_T = 0.4$) tip speed propellers at

AoA ($\pm 10^o$). He found that due to the domination of thickness noise at higher M_T the propellers show relatively smaller variation in axial directivity with AoA. A similar observation made by Mani [12] has also been discussed in Section 3.1.1.

These observations show the variation in acoustic characteristics with AoA and highlight the need for detailed acoustic analysis of low-speed propellers operating at an AoA. During the 1980s, the focus was on large propellers operating at high Reynolds numbers for commercial aircraft. It was not until the mid to late 2000s that propellers operating at low Reynolds numbers would get their due.

3.2. Low Reynolds number

This section discusses the most recent research in the field of UAV propellers operating at low Reynolds numbers. It is divided, into an aerodynamic (Section 3.2.1) and an aeroacoustics (Section 3.2.2) section. The aerodynamic section explores the variation in aerodynamic characteristics of airfoils with Reynolds number and its impact on propeller performance. In the aeroacoustics section, the acoustic characteristics of UAV propellers in different configurations are discussed.

3.2.1. Aerodynamic research

A common feature across all commercial UAVs is their compact size and relatively low flight speed, which effectively translates into an operational Reynolds number of $\leq 2 * 10^5$. At such low Reynolds numbers, viscous forces assume greater importance than the inertial forces within the fluid. It results in the change of boundary layer (BL) characteristics, such as flow transition, separation, etc. Fig. 3.9a provides an insight into these changes with change in Reynolds number. For airfoils operating between $10^4 < Re < 5*10^4$ the BL is stable (due to the influence of viscous forces), and the flow remains laminar (does not separate) for most of the chord length. Due to the relatively low Reynolds number, there is no formation of a turbulent boundary layer over the airfoil resulting in direct flow separation. The flow separation point starts moving towards the leading edge of the airfoil with an increase in AoA, which causes abrupt changes in lift and drag values. At Reynolds number in the range of $5*10^4 < Re < 2*10^5$, after separation the laminar boundary layer gains enough momentum to reattach itself to the airfoil. The region between the point of separation and reattachment is known as a laminar separation bubble (that spans $15 - 40\%$ of the chord length [44]) and results in increased drag over the airfoil. The point of reattachment is dependent upon the Reynolds number, as a result, the reattachment point is further downstream as compared to $Re > 2 * 10^5$. Airfoils operating at $Re > 2 * 10^5$ experience flow transition (from laminar to turbulent) before flow separation. The turbulent boundary layer energized by the free stream remains attached to the airfoil and prevents flow separation, improving $(C_L/C_D)_{max}$ performance. As a result of which Reynolds number has a significant impact on airfoil performance, see Fig. 3.9b.

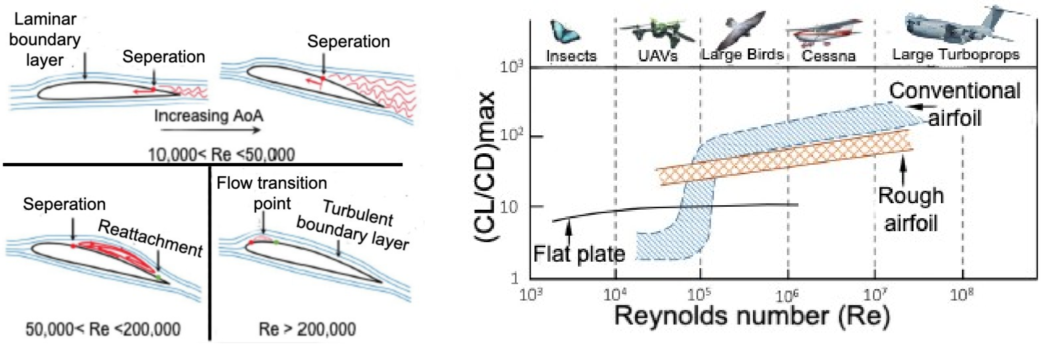

(a) Airfoil boundary layer flow characteristics with Re [45]

(b) Effect of Re on airfoil sectional $(C_L/C_D)_{max}$; adapted from [44]

Figure 3.9: Impact of Re on airfoil characteristics

Historically extensive studies have been carried out to understand the performance of propellers operating at high Reynolds numbers. The efficiency of these fixed pitch propellers peaked (for designed conditions) at around 83% for traditional wooden propellers and went up to 90% for modern composite propellers [46]. UAV propellers have shown considerably lower performance, with peak efficiency at around $60 - 70\%$ [47]. These propellers also exhibit a high sensitivity to change in Reynolds number, with peak efficiency dropping by 10% as the Reynolds number changes from $2 * 10^5$ to $1 * 10^5$ [47]. However, above $Re = 2 * 10^5$ Reynolds number has a relatively lower impact on propeller efficiency. An experimental study by Gamble showed that efficiency drops by only 5% as the Reynolds number drops from $1.1 * 10^6$ to $4 * 10^5$ [46]. It is due to the variation of $(C_L/C_D)_{max}$ value with Reynolds number. At $5 * 10^4 < Re < 2 * 10^5$ the $(C_L/C_D)_{max}$ shows a sharp increase in value resulting in improved airfoil performance. The improvement in airfoil performance results in better propeller efficiency, as the propeller can produce more lift (thrust) at lower drag (torque). Experiments by Gamble et al. [46, 47] showed a dependency of propeller performance on Reynolds number and recommended more studies to quantify the variation. It eventually leads to the development of the UIUC [48] database for low Reynolds number propellers. The database contains performance data of about 79 propellers in the 9 to 11-inch diameter range. To examine the Reynolds number effect (Re range of $5 * 10^4 - 10^5$) these propellers were tested for a range of RPM $(1,500 - 7,500)$ and echoed the observations made by previous researchers. The peak efficiency was measure at 65% and went as low as 28% for some Reynolds number, and propeller types [49]. The low Reynolds number provides unique challenges in predicting propeller performance using existing models [50]. As a result, such experiments provide data to validate and improve existing models. A similar approach is taken to understand the impact of inflow angle on propeller performance [51]. A common trend observed is that the thrust value increases with an increase in AoA. The AoA has a comparatively smaller impact on the torque (and consequently the power consumed) of the propeller [52]. Demonstrating an increase in propulsive efficiency with AoA, however, the difference in propulsive efficiency with AoA collapse when calculated using the inflow-based advance ratio (see Appendix A) [53].

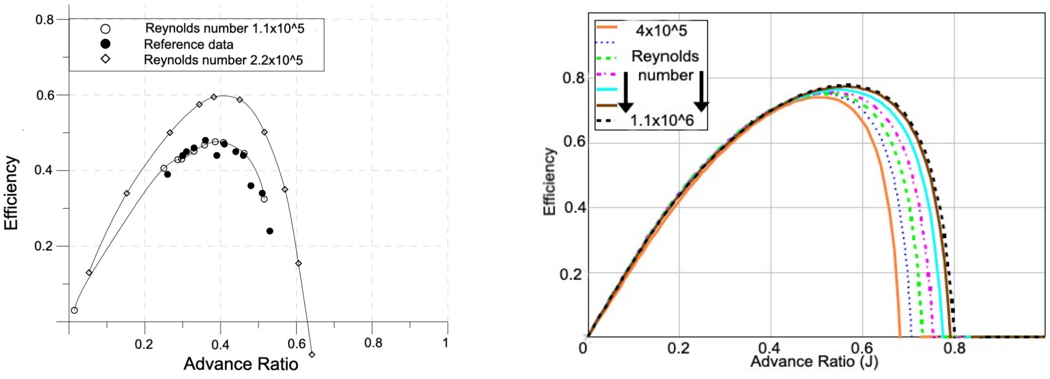

(a) Variation in efficiency of a Zinger 16x6 propeller [47]

(b) Variation in efficiency of an APC 18x12 propeller [46]

Figure 3.10: Impact of Re on airfoil characteristics

3.2.2. Aeroacoustic research

Historically research on UAVs was primarily geared towards flight dynamics and controls. It helped understand their performance characteristics but was not much help in improving them. The surge in commercial UAVs use highlighted their performance shortcomings and annoyance caused by their acoustic signature [13]. According to the literature surveyed [13, 54], the primary sources of propeller noise are steady loading, unsteady loading/vortex sound, and motor noise. The present section will look into the influence of these sources on the acoustic characteristics of UAV propellers and their variation with change in inflow/surrounding condition.

Zawodny et al. [13] conducted acoustic measurements on two isolated propellers (DJI 9443 and APC 11x4.7 SF) to understand their acoustic characteristics. Measurements were taken by a five microphone arc placed at a distance of $1.9\ m$ (from the center of the propeller) along the propeller axis. The propellers produced the same thrust at different RPM resulting in a difference of up to 8 dB in the OASPL. The difference was primarily due to the change in BPF due to RPM. However, on applying A-weighting to OASPL, the noise advantage from having a lower RPM reduced to less than 3 dB. The presence of motor noise in the mid-frequency range $(1,000-3,000\ Hz)$, see Fig. 3.11, can be identified as one of the probable causes.

In traditional propellers installation effects, caused due to flow distortions, impact propeller noise [9]. Hence, it is imperative to understand the impact of the rotor and airframe interaction on UAV noise to

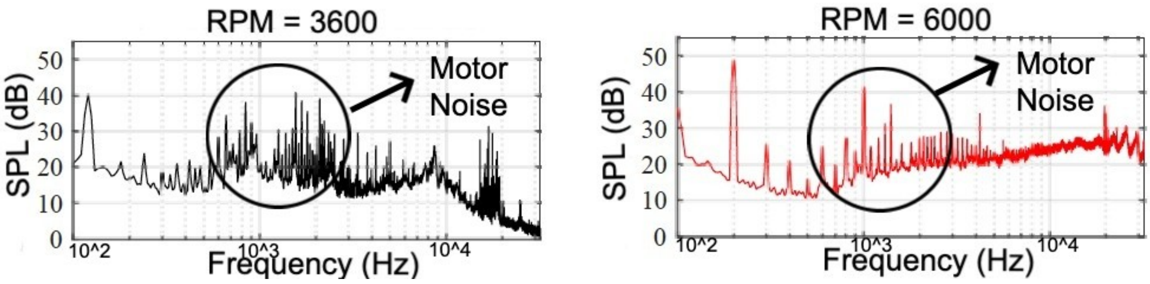

(a) APC 11×7 propeller

(b) DJI 9443 propeller

Figure 3.11: Power spectrum plot for at constant thrust of 2.8 N [13].

develop a more realistic understanding of their acoustic signature. Zawodny et al. [14] built on the study of isolated propellers to include UAV airframe, see Fig. 3.12a. The study revealed that the presence of an airframe close to the rotor ($\Delta/R = 0.1$) increases the amplitude of BPF harmonics (up to 7^{th} BPF), see Fig. 3.12b. The sudden change in local induced velocity due to the airframe causes unsteady blade loading, which increases the amplitude of higher harmonics. The rise in amplitude of higher harmonics falls significantly with increasing rotor-airframe separation. It starts to resemble the acoustic spectra of an isolated propeller at $\Delta/R = 0.5$. Yoon, Wang et al. [55, 56] conducted further computational and experimental studies to understand the impact of rotor mounting location (over vs. under mount) on noise. The results showed a significantly higher tonal content for under-mounted rotors (especially at higher BPF). The presence of an airframe above the rotor produces large disturbances in the flow field, which results in a larger fluctuation of induced velocity, causing a rise in the amplitude of fluctuating pressure. It results in the production of higher unsteady noise. These findings are in line with the results by Zawodny, Coffen et. al. [14, 57]. The results reported take us a step closer to understanding the acoustic characteristics of UAVs.

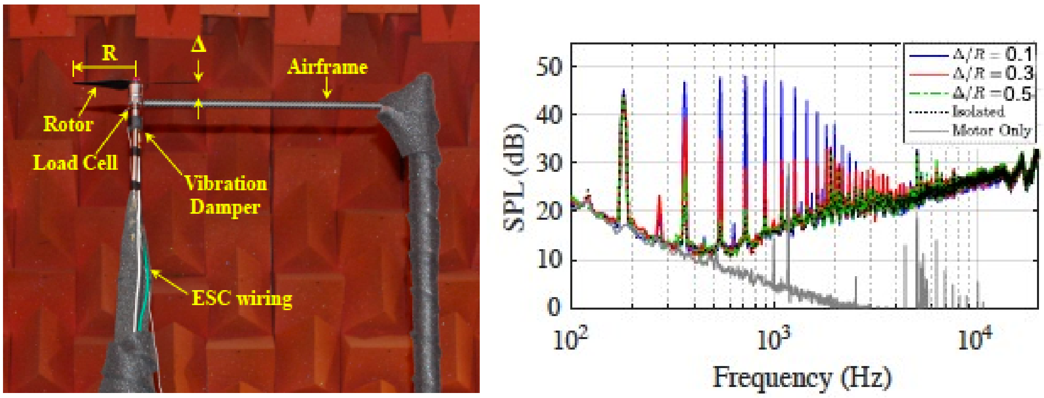

(a) Experimental setup used by Zawodny (over mounted rotor configuration)

(b) Impact of rotor airframe separation (Δ/R) on propeller noise

Figure 3.12: Experimental setup and impact of rotor airframe separation on propeller noise [14]

Yang et al. [15], investigated the impact of freestream velocity and AoA on an isolated UAV rotor. It is the only study (to the best of the author's knowledge) exploring the effect of shaft AoA on isolated UAV rotors. The experiment was conducted at an AoA of 90^o to 70^o, reference AoA defined in Fig. 5.4, for different freestream velocities, and RPM. The increase in freestream velocity at constant RPM and AoA increased the mean thrust produced by a rotor. Operating at an AoA, the radial (cos) component of the free stream is responsible for introducing asymmetry in rotor disc loading, see Fig. 3.13. Consequently, at fixed free stream velocity, increasing the AoA results in the higher harmonics of the BPF, see Fig. 3.14b. Increasing the free stream velocity at fixed AoA also has a similar effect Fig. 3.14a. The direction of flow over the rotor causes BVI, which could also be one of the probable causes for the rise in higher harmonics (up to 7^{th} BPF) [15]. The circumferential directivity was measured using an array of 18 microphones placed at the base of the setup, see Fig. 3.13. The directivity pattern was dominated by the 1^{st} BPF noise and is higher in the first and the third quadrants for all AoAs and free stream velocity. Doppler shift, BVI, and higher relative velocity of the blade sections in the first and third of the blade are all listed as plausible causes for the effect. Distinguishing the contribution of phenomena is left for future work.

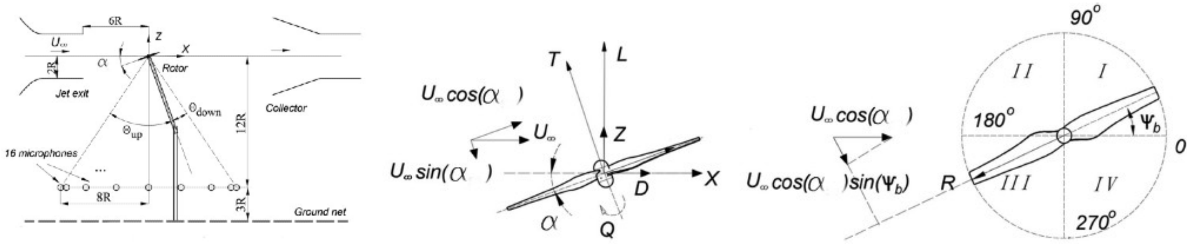

Figure 3.13: Schematics of the experimental setup along with rotor coordinates [15]

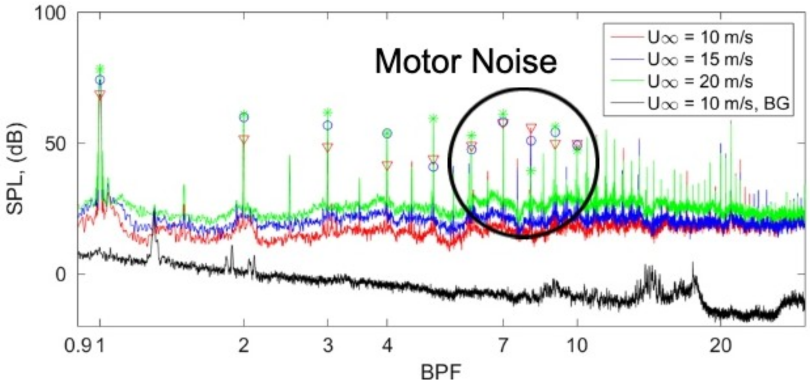

(a) Noise spectra for different free stream velocity at 7000 RPM, $\alpha = 10^o$ and $\Psi = 0^o$

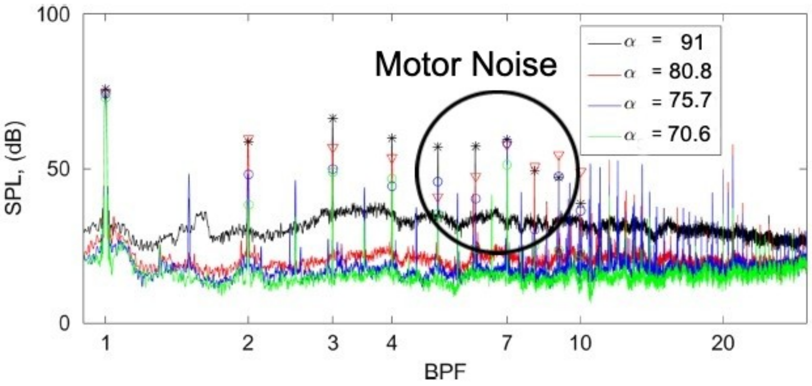

(b) Noise spectra for different AoA at 7,000 RPM, $U_\infty = 15$ m/sec and $\Psi = 0^o$

Figure 3.14: Noise spectra for different free stream velocity and AOA [15]

3.3. Research questions

The literature surveyed point to an increased interest in understanding the characteristics of propellers operating at Low Reynolds numbers. The focus area of researchers has been in the axial flow regime. Only a few experimental and analytical studies have attempted to capture the trends in aerodynamic performance with inflow angle. Even fewer studies exist in understanding the acoustics characteristic at an inflow angle. The review highlighted a research gap in the impact of non-axial inflow conditions on propellers operating at low Reynolds numbers.

To address this gap, the author chooses to conduct a high fidelity CFD study. The study is performed using PowerFLOW®. It is an LBM-VLES based flow solver that offers a relatively cost-effective way to

CFD and CAA analysis. However, the net cost associated with conducting a CAA study is still high. As a result, the first research question that this project seeks to answer is:

1. **What is the computational resource required in conducting a study of the impact of AoA on aerodynamics and acoustic characteristics of a propeller operating at low Reynolds numbers?**
    - What is the required grid resolution to accurately capture all the flow phenomena?
    - What is the impact on the accuracy of results with changes in grid resolution?
    - How does the variation in AoA impact the accuracy of the results at a similar grid resolution?

    Having answered the above question and performed the validation of the results wrt. experimental data. The next question that this research seeks to answer is:

2. **What is the impact on Aerodynamics characteristics of the propeller with a change in AoA?**
    - What impact does a change in AoA have on the overall performance and efficiency of the propeller?
    - How does the thrust and torque value vary across the propeller blade with a change in AoA and azimuthal position?
    - What is the impact of the change in AoA on the flow field?

    The acoustic behavior of a propeller is directly linked to its aerodynamic characteristics, hence the next question that the research aims to answer is:

3. **What is the impact on the acoustic characteristics of the propeller with a change in AoA?**
    - How does the sound power level produced by the propeller change with AoA? How does it relate to the aerodynamic characteristics of the propeller blade?
    - How does the axial and radial directivity of the noise produced change with changing AoA?
    - What changes occur in the SPL levels of higher harmonics due to change in AoA?

Based on these questions, analysis of the results has been carried out and discussed in Chapter 6 and 7. The conclusions drawn are discussed in Chapter 8 along with the scope of future research.

4

Methodology

This chapter introduces the methodology used for conducting the CFD and CAA analysis of this study. Section 4.1 discusses the fundamentals of the lattice Boltzmann method (LBM). The section also lists its advantages and disadvantages. Section 4.2 discusses how LBM is implemented in Dassault Systèmes PowerFLOW®. In the final part, Section 4.3, the implementation of the FWH analogy in the solver, the sampling criteria, and other methodology used for obtaining the aeroacoustic results are presented.

4.1. Lattice Boltzmann method

The first part of this section (Section 4.1.1) shall discuss the fundamental principles of the LBM and its underlying physics. The second part (Section 4.1.2) presents a comparison between LBM and traditional Navier-Stokes (NS) based flow solver.

4.1.1. Principle of LBM:

The LBM, though not directly developed from the Boltzmann equation, is an extension of the lattice gas automata method and is based on microscopic models and mesoscopic kinetic equations. The basic idea of LBM is to develop simplified kinetic models incorporating the physics of microscopic processes such that macroscopic averaged properties follow the desired macroscopic equations [58]. The premise for using such simplified kinetic models is that the macroscopic dynamics of fluid result from the collective dynamic properties of its constituent microscopic particles and is not sensitive to the details in the physics of the underlying microscopic particles [59].

The Boltzmann kinetic theory describes a fluid as a composition of several small particles exhibiting random motion. These particles exchange momentum and energy with one another through streaming and collision [16]. The LBM simplifies the Boltzmann equation by restricting the movement of particles to discrete nodes of a lattice. These models are represented using the $''DkQb''$ notation, where k represents the dimensions, and b represents the number of discrete velocity directions. If a 2D analysis is performed using a quadratic mesh, each particle can move in 9 discrete directions, and hence the model will be defined as $D2Q9$, as seen in Fig. 4.1. For a 3D space, depending on the computational need, it can be extended to a $D3Q15$, $D3Q19$, or $D3Q27$ model. PowerFLOW® uses the $D3Q19$ model, using 19 particle velocity states ensures sufficient lattice symmetry to recover the NS equation for isentropic flow [60, 61]. The phenomenon of particles exchanging momentum and energy through streaming and collision can be modeled using the Boltzmann transport equation, given as:

$$\frac{\partial f}{\partial t} + u.\nabla f = \Omega \tag{4.1}$$

where $f(x,t)$ is the particle distribution function, u denotes the particle velocity, and Ω is the collision operator. LBM is a simplification of the Boltzmann equation through discretization. Hence, the above equation after LBM discretization can also be written as [16]:

$$\underbrace{f_i(x+ce_i,t+\Delta t)-f_i(x,t)}_{\text{Streaming}} = \underbrace{-\frac{f_i(x,t)-f_i^{eq}(x,t)}{\tau}}_{\textbf{Collision}} \tag{4.2}$$

where $c = \frac{\Delta x}{\Delta t}$ is the lattice speed, e_i denotes the microscopic velocities, the subscript i denoting all the possible direction in which the particle can travel (19 for a $D3Q19$ model), f_i is associated with the discrete probability distribution function, f_i^{eq} the equilibrium distribution and τ the relaxation time towards local equilibrium.

To simulate a single-phase flow, f_i^{eq} can be defined using the Bhatnagar-Gross-Krook (BGK) collision model as [16]:

$$f_i^{eq}(x,t) = w_i\rho\left[1+3\frac{e_i.u}{c}+\frac{9}{2}\frac{(e_i.u)^2}{c^2}-\frac{3}{2}\frac{u.u}{c^2}\right] \tag{4.3}$$

In the above equation, w_i are the weights which for a $D2Q9$ model are given as:

$$w_i = \begin{cases} 4/9 & i = 0 \\ 1/9 & i = 1,2,3,4 \\ 1/36 & i = 5,6,7,8 \end{cases}$$

where i represents the number of discrete directions in the model.

The summation of microscopic particle distribution can be used to find the macroscopic fluid properties. Fluid properties such as density (ρ) and velocity (u), for a $D2Q9$ model, be obtained from microscopic properties as [16]:

$$\rho(x,t) = \sum_{i=0}^{8} f_i(x,t) \tag{4.4}$$

$$u(x,t) = \frac{1}{\rho}\sum_{i=0}^{8} cf_ie_i \tag{4.5}$$

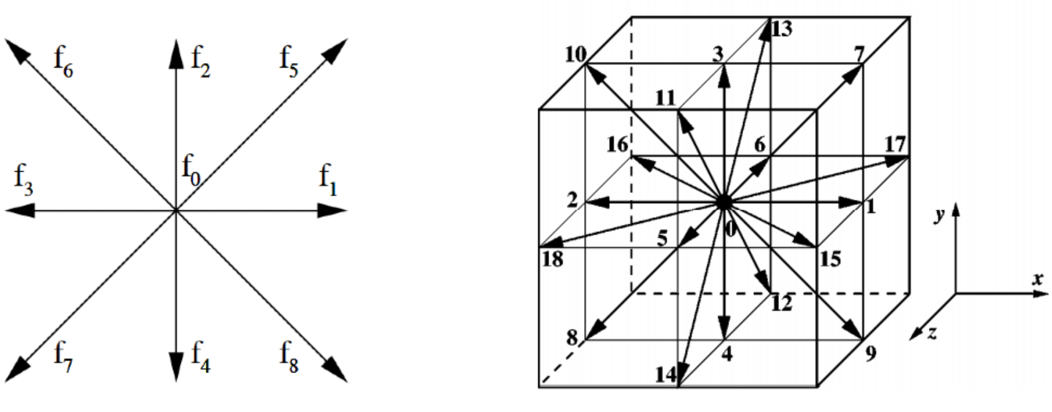

Figure 4.1: Discrete lattice nodes in D2Q9 model (left([16]) and D3Q19 model (right [17]).

4.1.2. Choice of LBM

Recent years have seen LBM-based flow solvers gaining acceptance as a promising and viable alternative to NS-based flow solvers. As mentioned, this study utilizes an LBM based flow solver called PowerFLOW®, the choice of which has been motivated based on the following factors [17, 60, 62]:

Advantages

- Simulations are inherently transient, stable, and convergent.

- Easy parallelization of simulations enabling it's use for resource-intensive simulation.
- Low dissipative properties of LBM and the capability to correctly reproduce fundamental acoustic phenomena.
- Capability to manage complex geometries and unlike NS-based CFD solvers, cell quality is not a concern.

Disadvantages

- Applications of the LBM have not yet been validated for supersonic flows. Hence their use is presently limited to compressible low Mach number or transonic flow regime.
- LBM is valid only for small Knudsen numbers, i.e., it can be used only for continuum flow.
- It is less suited for steady-state flow.

Based on the above factors, it can be stated that LBM is best suited for transient, subsonic flow involving complex geometries. This study focuses on the aerodynamic and acoustic properties of a propeller (complex geometry) operating under unsteady flow conditions at low Reynolds and Mach number ($M < 0.3$). As a result, the disadvantages of LBM are not as significant as the advantages for this study. Hence an LBM-based solver has been used.

4.2. LBM implementation in the flow solver

This section discusses the implementation of LBM into PowerFLOW®. Section 4.2.1 discusses the algorithm and computational loop used by PowerFLOW®, followed by the turbulence model used in Section 4.2.2. In Section 4.2.4 and Section 4.2.3, grid generation and the boundary conditions have been discussed.

4.2.1. Algorithm

The algorithm used for computationally implementing the LBM for flow characterization is broken into the three main steps and described as [16, 17]:

- **Step a →Initialization:** The values for ρ, u, f_i and f_i^{eq} are initialised for the first time step of the simulation. Otherwise, values of ρ and u are obtained from f_i using Eq. (4.4) and Eq. (4.5). The length of the arrow, see Fig. 4.2 is representative of f_i i.e. the probability that the chosen particle with a specified velocity shall move in the direction of the arrow.
- **Step b →Propagation:** This step is represented by Fig. 4.2a, while the state between collision and propagation is represented by Fig. 4.2b. The state can be represented as:

  $$f_i^*(x + e_i, t + 1) = f_i(x, t) \tag{4.6}$$

  where f_i^* on the LHS is computed using f_i on the RHS obtained from the previous time steps. The new value of f_i^* is then used to compute ρ and u using Eq. (4.4) and Eq. (4.5). Which are used for initializing the loop for recurring time step in **Step a**.
- **Step c →Collision:** This step is represented by Fig. 4.2c after collision, the new equilibrium distribution (f_i^{eq}) for this step can be calculated using Eq. (4.3). A new frequency distribution ($f_i^{'}$) can be calculated using:

  $$f_i^{'} = f_i^* - \frac{1}{\tau}(f_i^* - f_i^{eq}) \tag{4.7}$$

  The new distribution function ($f_i^{'}$) can be used again in **Step a** and the process continues.

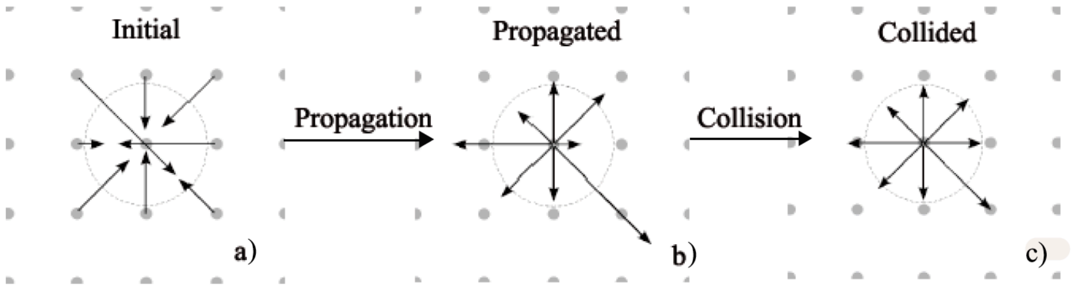

Figure 4.2: Computational Steps - $D2Q9$ from propagation to collision [17]

4.2.2. Turbulence model

Turbulence models are mathematical models that help predict the effects of turbulence, without first calculating the full-time-dependent flow field. In PowerFLOW® the simulation methods are divided into two main categories, each following a different simulation method. They are given as [63]:

- **Direct Simulation:** It is applied when the lattice length of the simulation is small enough to directly capture/resolve the smallest scale of turbulence. In such a case, LBM is equivalent to direct numerical simulation (DNS) of NS-equation [60]. The requirements of a DNS are measured by resolving the Kolmogorov length scale (around $Re^{-\frac{3}{4}}$), which makes DNS impractical for high Reynolds number. As a result, this simulation method is limited to flow in the region of $Re < 10^4$.

- **Turbulence Modeling:** It is not computationally feasible to resolve all scales at high Reynolds numbers ($Re > 10^5$). PowerFLOW® uses turbulence modeling for both bulk fluid and near the wall. The approach used by PowerFLOW® is commonly known as very large eddy simulation (VLES). In this approach, turbulent kinetic energy and dissipation are calculated by solving a variant of the RNG k-ϵ model for the unresolved scales of turbulence [60]. It also uses a wall function approach is to model boundary layers on solid surfaces.

4.2.3. Boundary condition

Boundary conditions (BC) are essential for the stability and accuracy of a numerical simulation. They help the simulation in representing the physical features of the simulation as close as possible. LBM needs to account for the discrete distribution functions (f_i) on the boundary. It is required to reflect the macroscopic properties of the fluid. To do so, the two most widely used BC are [16]:

- **Bounce-back BC:** These are used to implement a no-slip boundary condition. This implementation is well suited for simulating flow over complex geometry as it does not differentiate the orientation of the boundary. In such a BC when the fluid particle interacts with the boundary node, it is sent back (bounces back) to its original location. In this way, the velocity at the wall is set to zero ensuring a no-slip condition. The two main implementations of the bounce-back BC are on-grid and mid-grid BC [64]. On-grid bounce back is easier to implement than mid-grid BC, however, it is only first-order accurate. Mid-grid BC offers second-order accuracy at the cost of a modest increase in complications.

- **Zou-He Velocity and pressure BCs:** In this implementation, the BC depends upon the geometry of the boundary and is hard to implement for complex geometries. However, it enables users to model physical situations where velocity and pressure need to be prescribed at the boundary.

Based on these implementations, PowerFLOW® offers a set of BC such as a standard wall, frictionless wall, sliding wall, rotating wall, velocity wall, etc. These help model the physical characteristics of the simulation.

In PowerFLOW® a pressure-gradient extended law of the wall (PGE-LW) is used to produce a no-slip BC on solid walls [65]. The wall-model helps in reducing the computational cost and is given as:

$$u^+ = \frac{1}{\kappa} ln\left(\frac{y^+}{A}\right) + B \tag{4.8}$$

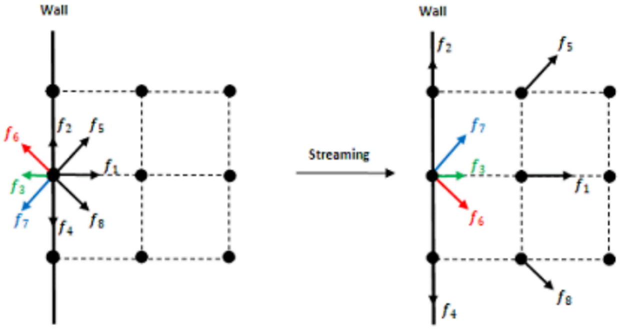

Figure 4.3: On-grid implementation of bounce Back BC [16]

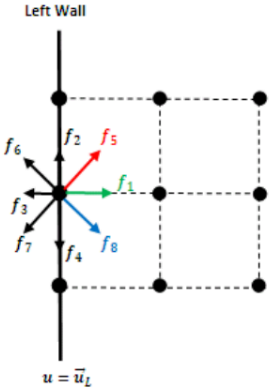

Figure 4.4: Zou-He BC [16]

such that,

$$A = 1 + \frac{f\left|\frac{dp}{ds}\right|}{\tau_w} \qquad \& \qquad y^+ = \frac{u_\tau \rho y}{\mu} \tag{4.9}$$

where y^+ represents the non-dimensional distance, u^+ is the non-dimensional velocity, u_τ represents the shear velocity, y the vertical distance between the solid surface and the mesh wall, and Von Karman constant $\kappa \approx 0.41$. A generalization of the bounce-back BC is used to iteratively compute the value of wall shear stress τ_w and used as a wall boundary condition.

4.2.4. Grid generation

Mesh/Grid divides a continuous geometric space into discrete topological and geometric cells. The method of mesh generation depends on the type of solver being used. In PowerFLOW® it is a semi-automated process which varies significantly from most Navier-Stokes based flow solver. To create a mesh in PowerFLOW® the entire simulation domain is divided into lattice elements during the discretization phase. The lattice elements form discrete cubes (know as voxels) in a 3D simulation domain. When the lattice interacts with a solid body in the simulation domain, it creates a planar lattice, also know as a surfel, as seen in Fig. 4.5. The fluid-particle moves from one voxel to another during the simulation; if it encounters a surfel, then the user-defined BC is initialized.

In the present study, the flow region closest to the object being analyzed is of most interest. As a result, the region close to the propeller blade has a very high resolution. It is also recommended to have a simulation domain at least ten times the object of interest. Having the same mesh resolution throughout would make the simulation computationally expensive and waste resources. Hence, mesh refinement is applied in a traditional NS-based solver to get a higher resolution near the object while

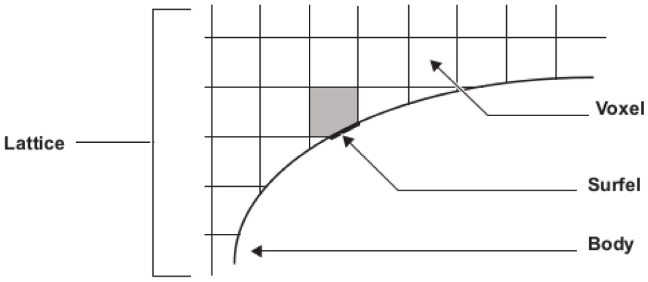

Figure 4.5: Elements of a lattice in PowerFLOW® [18]

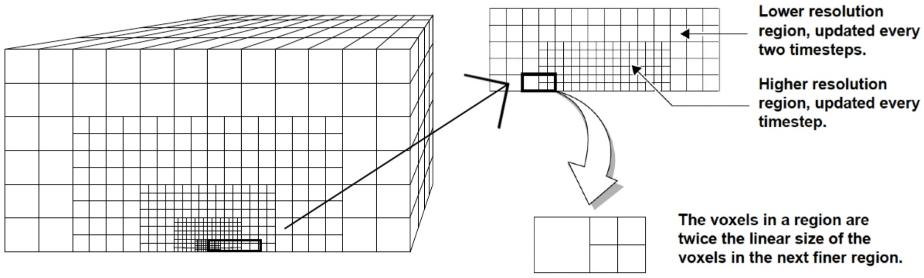

Figure 4.6: Voxel size dependence on VR region, adapted from [18]

having a progressively lower resolution further away. PowerFLOW® implements this by defining variable resolution (VR) regions in the simulation domain, as shown in Fig. 4.6. When moving between adjacent VR regions (high to low), the size of the voxel doubles (volume increases eight times), and the rate at which they are updated (time steps) halves. To ensure that the data between different VR regions are in sync with each other, the period of data collection between different VR regions varies as a multiple of 2^{n-1}. Where $n = 1$ defines the VR region with the highest resolution. The resolution of a setup defines the size of the voxels in the finest VR region. It determines the extent to which the flow phenomena are resolved in the simulation. Defining the resolution and number of VR regions in a setup is a trade-off between computational cost and desired accuracy.

In PowerFLOW® to simulate a rotating body, such as a propeller, a local rotating reference frame (LRF) needs to be defined. It allows the user to include rotating and non-rotating geometry in the same simulation. Enclosing the rotating geometry in a LRF creates a different reference frame, allowing the user to prescribe a rotational speed to these parts. The LRF has two main subtypes:

- **Stationary LRF:** It does not rotate wrt. the global frame, however, produces accurate results. It is best suited for axisymmetric flow conditions with negligible transient effects.
- **Sliding-mesh LRF:** The frame changes position and orientation wrt. to other portions of the domain. It is best suited for asymmetric inflow conditions with significant transient effects.

The present study needs to take into account the flow asymmetry and transient effects caused due to AoA. Hence, sliding-mesh LRF is chosen. The LRF region is divided into several axisymmetric rings during discretization, see Fig. 4.7 (bottom). In the case of a sliding-mesh LRF, each of these radial rings can only cross two VR regions during rotations, as shown in Fig. 4.7 (top).

4.3. Aeroacoustic solver

The FWH analogy has been implemented in PowerFLOW® to capture the pressure values obtained by solving the flow field. This section explains how the FWH analogy is implemented in the solver in Section 4.3.1, and Section 4.3.2 discusses the sampling criteria used to capture the desired frequency range of the noise produced by the propeller.

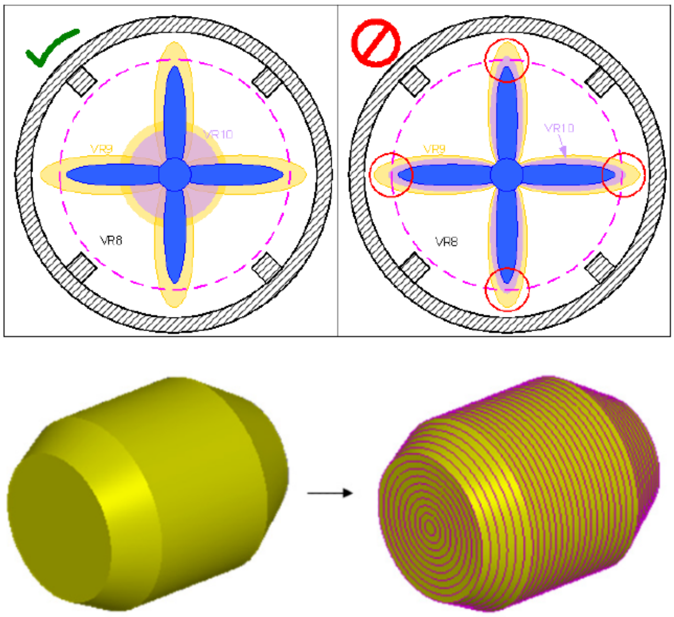

Figure 4.7: Grid generation for rotating bodies [18]

4.3.1. FWH analogy implementation

The FWH analogy has been introduced in Section 2.4.2 this section deals with its practical implementation into the solver. FWH analogy solves for the acoustic far-field by integrating the pressure field over a surface in PowerFLOW® these surfaces are defined as:

- **FWH solid surface (FWH SLD):** In this case, the integrating surface matches the boundary of the solid that is being analyzed. It requires low computational resources and enables the user to isolate the contribution of different components. However, the solid FWH surface only accounts for the loading (dipole) and thickness (monopole) noise source. The noise produced due to flow non-linearities (quadrupole source) is not considered [66].

- **FWH permeable surface (FWH PRM):** It was developed by Francescantonio [67] in 1997. In this method, an integrating surface surrounds the solid of interest and tries to capture the surface and volume source terms. It typically means that the integrating surface is much larger than the object of interest. As pressure fluctuations require a fine resolution to be accurately captured, propagating it to larger distances increases the computational cost. Apart from this, interaction with turbulent structures and hydrodynamic fluctuations can also corrupt the pressure data captured on the permeable integration surface.

This thesis deals in low Mach number flow hence the contribution of quadrupole noise sources would be negligible. Consequently, both solid and permeable FWH surfaces can be used for acoustic post-processing. Section 6.2.1 presents a comparison between the acoustic result from the two surfaces and discusses the motivation behind selecting one of the analogies.

Dassault PowerFLOW® employs an advanced-time approach (derived from retarded time approach), based on formulation 1A by Farassat [68], to solve the FWH equation. The retarded time approach adopts a receiver/observer point of view, where signals emitted at different times and covering different distances are evaluated at a particular time by summing up the pressure fluctuations. In the advanced time approach, a source point of view is adopted, calculating the contribution of the source at a particular time and propagating it to the receiver/observer. Meaning that a signal emitted by a point source moving at sub/supersonic velocity is received only once by an observer at subsonic velocity [66].

The advantage of using an advanced time approach over retarded time approach is that it enables the use of a parallel architecture, which reduces the computational cost associated with acoustic prediction in a simulation. The advanced time approach also does not require iterative solutions, making it easier to implement and more efficient than retarded time approach [66].

4.3.2. Acoustic signal sampling

Section 2.2.2 provides an overview of different frequencies perceived by humans. It helps in selecting a desirable frequency range that should be analyzed. Selecting the desired frequency range comes under signal sampling and is governed by two main criteria:

- **Temporal criterion:** The Nyquist criterion states that the sampling frequency (f_s) should be at least two times the highest frequency (f) of the signal that needs to be captured ($f_s \geq f$).
- **Spatial criterion:** Applicable in the case of computational analysis, this criterion defines the minimum number of numerical points (voxels in PowerFLOW®) required per wavelength for a given frequency. The recommended value is to have at least ten numerical points per wavelength [69].

These criteria determine the highest frequency range that can be captured without introducing signal aliasing. Fig. 4.8 shows the difference between a well-sampled (top) vs. an aliased signal due to undersampling (bottom). A Fourier analysis on an undersampled signal results in a wave with a different phase and frequency than the original wave.

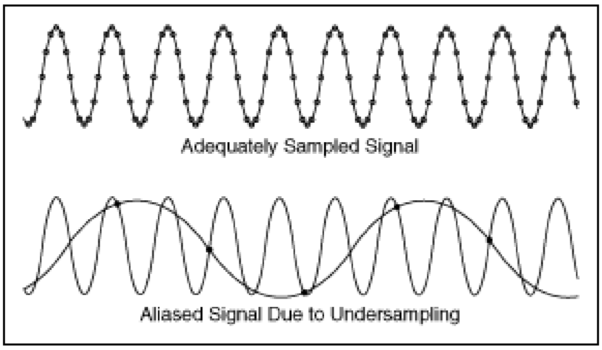

Figure 4.8: Well sampled signal (top) vs aliased signal due to under-sampling (bottom)

The sampling of data should start only after removing the initial transient phase of the simulation. Based on past experiences, it is recommended to start sampling the data after [31]:

1. At least ten flow passes over the entire length (l) of the object being analyzed.

$$t_{start} \leq \frac{10l}{U_\infty} \tag{4.10}$$

2. The flow should have passed through the entire length (L) of the initial flow domain at least once and cleared the initial field setup.
3. The flow parameters should have converged.

In PowerFLOW®, transient time can be reduced by seeding files from a previous simulation to initialize the flow field. The general practice is to use a coarse simulation file as a seed for a finer simulation, which helps in reducing the value of (t_{start}) and hence the overall cost of the simulation.

5

Setup

This chapter explains the computational setup designed for the study. Section 5.1 reports the geometry used and the coordinate system of the setup. It is followed by a discussion on the mesh resolution and rationale behind its selection in Section 5.2. Sections 5.3 and 5.4 introduces the reader to the boundary conditions, flow parameters, and flow measurements being saved. In Section 5.5 the experimental setup is presented, and parallels are drawn to the computational setup.

5.1. Geometry

The propeller chosen for this study is designed and manufactured at TU Delft. It is a twin-blade propeller with a radius of $15\ cm$ and utilizes a NACA-4412 airfoil for its blade section. The distribution of blade angle (twist) and chord length of the propeller to the blade span is given in Fig. 5.1.

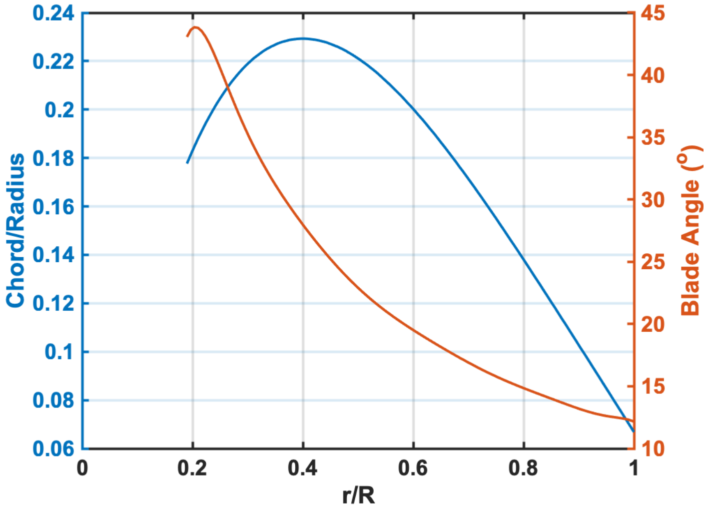

Figure 5.1: Propeller chord length and blade angle vs blade span (r/R)

The blade geometry is imported as a single-faced STL file into $Opty\partial b^{®}$. The tool, developed by Dr. D.Casalino, segments the blade into multiple faces, referred to as Face IDs, and can add a user-defined zig-zag trip on the blade surface, see Fig. 5.2. Dividing the blade into multiple faces enables the user to set different mesh resolutions for different faces, while the trip induces flow transition. The significance of the trip for the setup has been discussed in Section 5.1.2. Table 5.1 describes the colored sections (Face IDs) on the blade surface. The computational setup is based on an experimental study being performed at TU Delft. To accurately replicate the experimental setup it is decided to add a nacelle in the computational domain instead of analyzing a stand-alone propeller, as shown in Fig. 5.3.

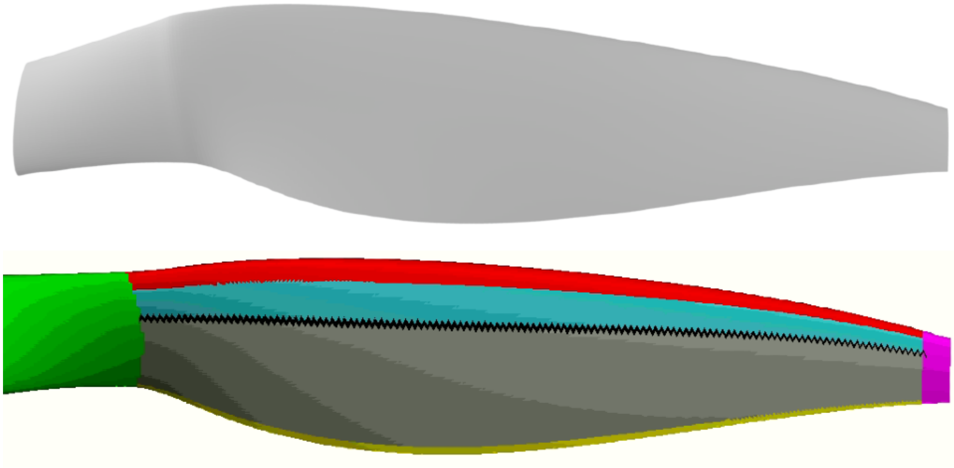

Figure 5.2: Propeller blade before (top) and after (bottom) being processed by $Opty\partial b^{\circledR}$

Face ID	Tip	Root	Leading Edge	Trailing Edge.	Laminar Section	Turbulent Section
Color	Purple	Green	Red	Yellow	Blue	Grey
Location	2.5 % of R	20 % of R	10 % of C	5 % of C	15 % of C	70 % of C

Table 5.1: Description and location of Face IDs on the rotor blade; R = blade radius, C = local chord length

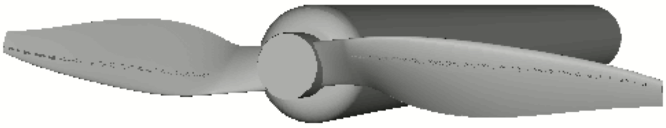

Figure 5.3: Complete geometry of the propeller setup

5.1.1. Coordinate System

Coordinate systems are used to define the geometry and physical properties of the flow in a computation setup. This simulation utilizes three Cartesian coordinate systems to define the propeller position, simulate an AoA, and rotation of the propeller blades. The coordinate systems that have been used are defines as follows:

- **Default/Aircraft coordinate system:** The default/aircraft coordinate system is the global coordinate system for the setup. It is the base coordinate system of the setup upon which all the other coordinate systems are defined. In this coordinate system The z-axis is defined along the axis of rotation and the positive y-axis and x-axis points towards $\Psi = 180^o$ and $\Psi = 270^o$ respectively, see Fig. 5.4a.
- **freestream coordinate system:** The setup changes the inflow angle instead of moving the propeller geometry to simulate an AoA. This method of defining the AoA ensures that the propeller position stays fixed despite the change in AoA. It eliminates the need to correct the acoustic data for distance with a change in AoA. The freestream coordinate system takes the default/aircraft coordinate system as its reference frame. On specifying an AoA, the freestream coordinate system adapts its position to the default coordinate system. It modifies the inflow angle of the freestream hence simulating an AoA. Fig. 5.4b shows the change in inflow angle relative to the propeller

geometry.

- **Local Rotating reference frame (LRF):** The LRF is a non-inertial rotating reference frame of the setup. It defines the speed and direction of rotation for the propeller. For the present simulation, the RPM is $6,000$, and the propeller rotates in an anti-clockwise direction (forward-looking aft). A volume of revolution is defined to create the LRF, such that it contains all the parts of the geometry that will rotate relative to the inertial reference frame. Fig. 5.4c shows the direction of rotation of the propellers to the default coordinate system.

In this thesis, all the measurements and results discussed are relative to the default/aircraft coordinate system.

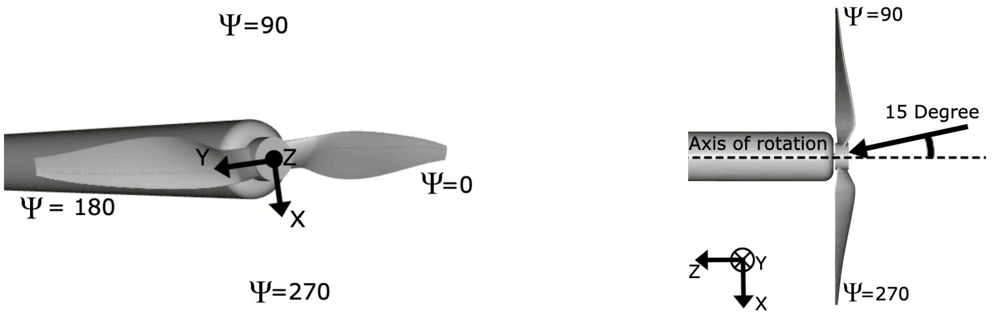

(a) Default/Aircraft coordinate system

(b) Freestream inflow at an AoA of 15^o

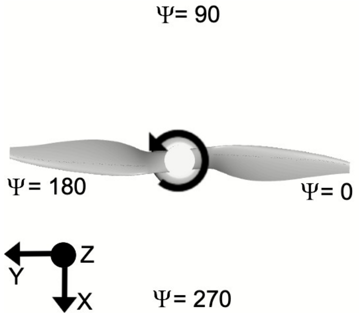

(c) LRF coordinate system

Figure 5.4: Coordinate system with respect to the propeller geometry

5.1.2. Blade tripping

The nature of the flow (laminar or turbulent) over an airfoil directly impacts its aerodynamic and aeroacoustic properties. Inherently a complex phenomenon, flow transition depends on several parameters such as inflow condition, surface roughness, etc. [70]. LES can directly capture flow transition [71]. However, the ability comes with its own set of challenges as errors in defining the conditions of transition in LES can give rise to artificial laminar regimes in the flow. It could induce fictitious separation of the boundary layer, severely impacting the validity of the results [72]. Forcing transition at a user-defined location helps avoid this pitfall, and study the flow characteristics with confidence.

Flow transition, in this study, is induced by placing zig-zag trips on the suction side of the propeller blades. The choice is motivated by the fact that the pressure side experiences a lower flow velocity compared to the suction side. Hence, flow separation would be less likely. Experiments by Leslie [32] have shown that tripping the suction side of a propeller blade leads to a reduction in the high frequency ($> 2,000\ Hz$) noise produced by the laminar separation bubble. $Opty\partial b^{®}$ is used to generate these user-defined trips. The trip properties relative to the propeller blade are shown in Fig. 5.5a.

The trip thickness of $17.41 * 10^{-2}\ mm$ was chosen, which has a resolution (trip thickness/ smallest voxel size) of at least 2 voxels for coarse resolution and 4 for the highest resolution. The choice of trip thickness is driven by the belief that a minimum of 2 to 3 voxels are required to accurately resolve the trip in the simulation [73]. The trip is placed at a relative distance of 25% of the chord length. It spans from 20 to 97.5% of the blade span more details about the trip have been provided in Table 5.2.

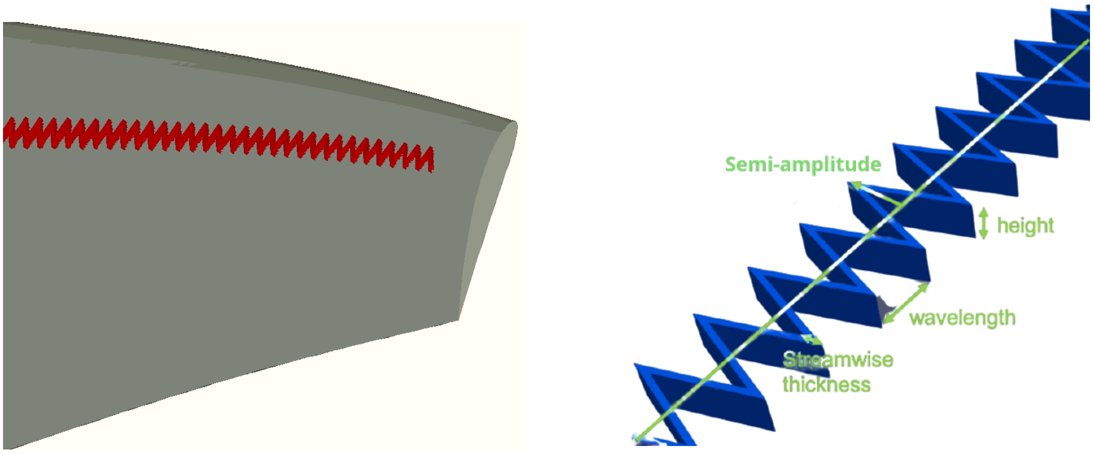

(a) Closeup of propeller blade (grey) and trip on the suction side (red)

(b) Trip parameters

Figure 5.5: Zig-Zag trip on propeller blade

Properties of trip	**Value**
Trip starting location	20% of R
Trip ending location	97.5% of R
Trip wavelength	4% of C
Chord/stream-wise thickness	2% of C
Max and Min Trip Height	0.75% of C
Trip amplitude	2% of C
Trip location	25% of C

Table 5.2: Zig-Zag trip properties on the propeller blade; R = blade radius, C = local chord length

5.2. Resolution

Mesh or grid resolution is defined as the distance between two measurement points in a computational setup. A fine/high resolution corresponds to having a lesser distance between two measuring points and improves the accuracy of the simulation. However, it also increases the computational cost, and having a fine mesh throughout the computational domain is prohibitively expensive. As a result, a computational setup consists of several layers of mesh with varying resolutions. These layers are referred to as variable resolution (VR) regions and have the highest resolution closest to the area of interest. The mesh gets progressively coarser away from the area of interest, as shown in Fig. 5.6. In this study, the computational domain has sixteen different VR regions. The corresponding voxel size for each VR region has been shown in Table 5.3.

VR Region	15	14	13	12	11	
Voxel size (m)	$5.71 * 10^{-5}$	$1.14 * 10^{-4}$	$2.29 * 10^{-4}$	$4.57 * 10^{-4}$	$9.14 * 10^{-4}$	
VR Region	10	9	8	7	6	
Voxel size (m)	$1.83 * 10^{-3}$	$3.66 * 10^{-3}$	$7.31 * 10^{-3}$	$1.50 * 10^{-2}$	$2.9 * 10^{-2}$	
VR region	5	4	3	2	1	0
Voxel Size (m)	$5.90 * 10^{-2}$	$11.70 * 10^{-2}$	$2.34 * 10^{-1}$	$4.68 * 10^{-1}$	$9.36 * 10^{-1}$	1.87

Table 5.3: Variation in voxel size with VR region for (for a medium resolution setup)

In the present simulation, the region near the propeller blades is the area of interest. As a result, VR regions 15 to 12 which have the smallest voxel size and consequently the highest resolution are

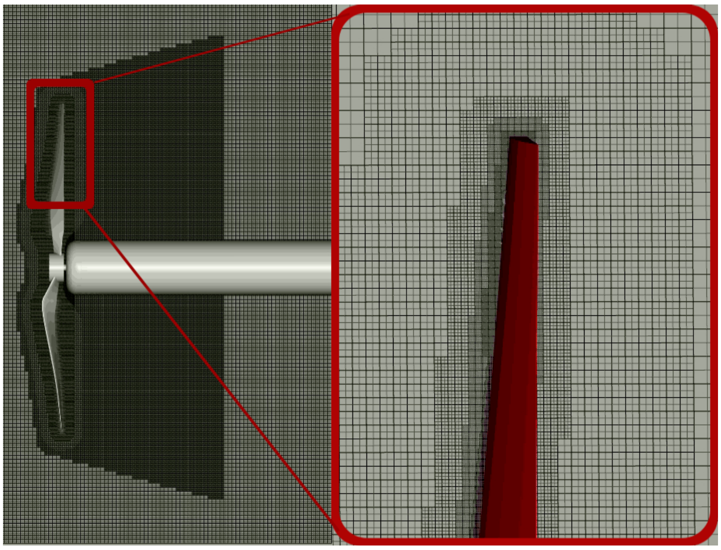

Figure 5.6: Change in grid size with VR region; VR region in close proximity of propeller setup (left) and VR region closer to the propeller blade (right)

placed closest to the propeller blade surface. It enables the simulation to resolve the flow field close to the propeller blade surface and get accurate force measurements while keeping the computational cost in check. To capture the tip vortices being shed by the propeller, a frustum is created in the propeller wake region. The frustum has a relatively high resolution than its surrounding (VR 11) and can be seen as the darker region on the left of Fig. 5.6. The frustum is chosen over a cylinder, as the cylinder can not accurately capture the deflection in the propeller wake due to the change in AoA. The location and shape of the VR regions have been discussed further in Section 5.2.1.

Resolution	Simulation domain size (m)	Smallest voxel $(10^{-5}\ m)$	Largest voxel (m)	Fine equivalent voxels (10^{6})
Coarse	$338 * 338 * 338$	8.1	2.6	9.8
Medium	$239 * 239 * 239$	5.7	1.7	18.6
Fine	$168 * 168 * 168$	4.0	1.3	36.4

Table 5.4: Variation in simulation domain and voxel size with resolution

Conducting a grid convergence/resolution study is a way of verifying the computational results. The study helps find if the simulation results produced are due to the inflow and boundary conditions set by the user or a consequence of mesh resolution. If the results are invariant to the mesh density then the simulation is said to be grid-independent. Chapter 6 discusses the results of the resolution study conducted on this simulation. For this study, three mesh densities were chosen (coarse, medium, and fine). The size of the voxels across the VR region changed with the mesh resolution. The size of the simulation volume depends on the voxel size, consequently, it also varies with the mesh resolution, as shown in Table 5.4. Increasing the mesh density increases the computational cost and is computed base on the number of fine equivalent voxels in a particular setup. The number of fine equivalent voxels is calculated using:

$$\begin{aligned}\textbf{Fine equivalent voxels} \ &= N(\text{ finest scale }) + N(2^{nd}\text{ finest scale })/2 + \\ &N(3^{rd}\text{ finest scale })/4 + N(4^{th}\text{finest scale})/8 + \ldots + \\ &N(\text{ coarsest })/\left(2^{(n\text{ grid levels- }1)}\right)\end{aligned} \tag{5.1}$$

where N corresponds to the total number of voxels in a VR region. Reduction in voxel size also impacts the Courant–Friedrichs–Lewy (CFL) condition of the setup, resulting in an increased number of time steps. Depending upon the hardware, an estimate of the computational time required per time step is provided by the solver and can be seen in Table 5.5.

Resolution	**Time-steps** 10^5	**Seconds per time-step** 10^{-8}
Coarse	9.9	12
Medium	14.1	8.5
Fine	19.9	6

Table 5.5: Variation in time stepping with resolution; the simulation is run for $0.12\ sec$

5.2.1. VR Regions

The VR regions used in the setup can be classified into three key regions: propeller surface (high resolution), propeller wake (medium resolution), and far-field (low resolution). The grid resolution and rationale behind the selection of these regions have been explained in this section.

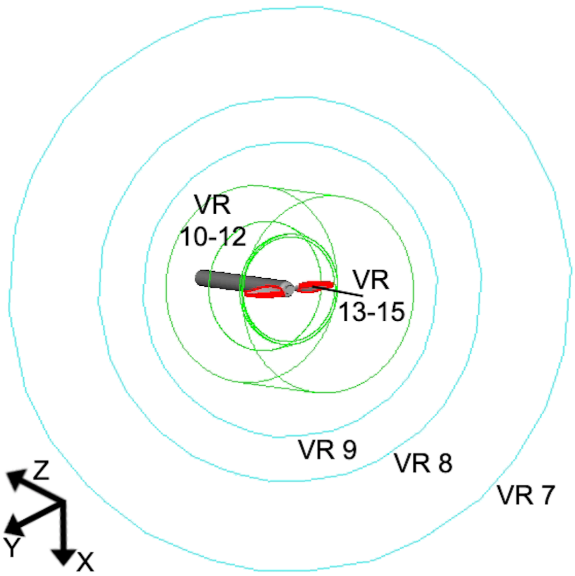

Figure 5.7: Variable resolution regions; propeller surface (red), propeller wake (green) and far field (blue)

Propeller surface

The region closest to the surface of the propeller blade experiences the highest variation in flow properties. The ability to resolve these flow fluctuations affects the qualitative and quantitative properties of the simulation. As a result, the mesh needs to be of the highest resolution closest to the propeller blade surface. In this simulation, the finest VR region (VR 15) is placed around the propeller blade surface. Subsequently, coarser VR regions then envelop the finest VR region. Each VR region is offset from the other by a thickness of approximately six voxels, which offers a fair compromise between computational cost and accuracy. The different VR regions over the propeller blade surface are shown in Table 5.6.

VR	**Surface location**	**Offset from propeller surface** $(10^{-3}\ m)$
13	All propeller face ID but root	2.6
14	All face IDs of propeller but root and laminar region on the pressure side	1.1
15	Trip, Tip, and TE of the propeller blade	0.37

Table 5.6: VR location in the propeller region (for medium resolution setup)

Propeller wake

The propeller wake is the region around the propeller in which the flow gets altered due to the propeller. The relative change in flow properties in this region is lower than close to the propeller blade surface. As a result, a relatively coarser mesh resolution can be used in this region. The region includes the frustum to capture the tip vortices and the permeable FWH surface for the acoustic measurements. It consists of three VR regions 10, 11, and 12, as shown in green in Fig. 5.8.

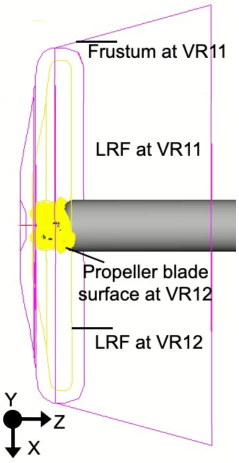

Figure 5.8: Variable resolution regions; VR 12 (yellow) VR 11 (Pink)

- **VR 12:** it consists of all the propeller blade surfaces (including the hub) and the inner LRF of the propeller. The VR region surrounding the propeller blade and the LRF have a thickness of 13 voxels. For the medium resolution set up, they are offset by $8.5\ mm$ from the propeller surface. As the LRF is in the same VR region as the propeller blade, it does not cross two VR regions in one rotation and avoids the limitations imposed in Section 4.2.4.
- **VR 11:** it consists of the frustum (as described in Section 5.2) and the outer LRF of the propeller. The frustum is 1.13 times the blade radius at $z/R = 0$, and increases to 1.4 times the propeller radius at a distance of $z/R = 1$ downstream of the propeller, making an angle 15^o with the propeller axis, giving it the ability to capture the wake being deflected due to the simulated AoA. The outer LRF has a thickness of 13 voxels and an offset of $20.42\ mm$ from the propeller blade surface for the medium resolution setup.
- **VR 10:** consists of a cylinder (see Fig. 5.8) that encapsulates the FWH permeable surface along with the transient fluid measurement region. It is 2.2 times the propeller radius and and a length of $0.53\ m$, stretching from $z/R = -1.8$ (upstream) to 1.8 (downstream) of the propeller.

Far field

The far-field region starts at VR 9 and expands radially outward till VR 0. The regions from VR 9 to VR 1 are spherical and are offset by 26 voxels from each other, whereas VR 0 is a cube. As the size of the domain is dependent upon the size of the voxels there is a variation in simulation domain size as observed in Table 5.4.

5.3. Acoustic measurement

A far-field analysis of the propeller noise is carried out to understand the acoustic characteristics of the propeller. The acoustic pressure fluctuations are sampled on a solid and permeable FWH surface, as discussed in Section 4.3.1. Acoustic measurements from the two formulations have been compared and discussed in Section 6.2.1.

Drawing from the recommendations made in Section 4.3.2, this study uses ten numerical points (voxels) per wavelength and an aliasing safety factor of four to calculate the highest sampling frequency. The permeable surfaces are placed inside VR region 10, see Fig. 5.9, with the innermost permeable

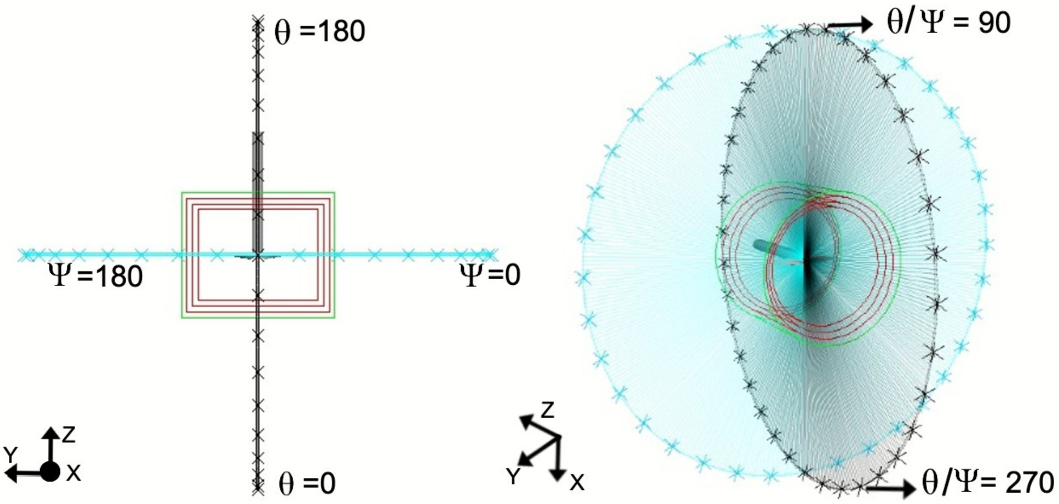

Figure 5.9: Acoustic setup of the simulation; 3 FWH permeable surface (red), VR 10 (green)

surface, having a radius of $0.26\ m$. The subsequent permeable surfaces grow outwards and are offset from each other by 13 voxels. The reason behind creating three permeable surfaces instead of one is to average out the hydrodynamic noise that might be present in the sound field [74]. The pressure fluctuations in a sound field are of the order $\bar{\rho}cU_l$, where $\bar{\rho}$ is the mean pressure, c is the speed of sound, and U_l is the local velocity fluctuation. The hydrodynamic pressure fluctuation (pseudo-noise field) is of the order $\bar{\rho}U_l^2$. As the hydrodynamic noise essentially travels at fluid velocity, averaging the value of pressure fluctuation from the three surfaces helps remove this pseudo-noise field.

The permeable surfaces are located in VR region 10, the size of a voxel (for medium resolution) in this region is $1.83 * 10^{-3}\ m$, and the flow values in this region are sampled at $3.67 * 10^5\ Hz$. The highest sampling frequency was calculated using an aliasing safety factor of 4 and comes up to be $91,000\ Hz$. However, given the location of the permeable surface, the spatial criterion determines the cutoff frequency. Table 5.7 shows the cutoff frequency as determined by the spatial criterion for different grid resolutions.

The noise radiation pattern of the propeller is captured around the propeller plane and in the axial direction. It is done by placing two circular microphone arrays, about the XY and XZ plane, with a polar resolution of 10^o and a radius of $1\ m$ from the center of the propeller axis, see Fig. 5.9.

Resolution	**Spatial cutoff frequency** (Hz)
Coarse	$13,282$
Medium	$18,773$
Fine	$26,564$

Table 5.7: Highest frequency set by spatial criterion at 10 voxels per wavelength

5.4. Simulation settings

This section reports the global parameters and the boundary conditions being used for the simulation in Sections 5.4.1 and 5.4.2. Section 5.4.3, checks for the time convergence of the simulation before discussing the measurements being saved in Section 5.4.4.

5.4.1. Global parameters

The values defined as the global parameters control the overall behavior of the simulation case. These values are the characteristic physical parameters that establish reference values used to non-dimensionalize the results. For this simulation, the default turbulence intensity is set at 0.1% of the

Characteristic parameters	Value
Pressure	$99,000\ Pa$
Temperature	293 K
Density	$1.18\ Kg/m^3$
Kinematic viscosity	$1.54 * 10^{-5}\ m^2/sec$

Table 5.8: Global characteristic parameters for the simulation

local velocity, and the turbulence length scale is set at $1\ mm$. These parameters define the turbulence characteristics for the fluid's initial condition. At 0.1% of the mean velocity, the turbulence intensity replicates a uniform inflow condition with very low freestream turbulence. The characteristic velocity is calculated by adding the rotor tip speed, at $6,000$ RPM, to the freestream velocity. The mean chord length of the propeller blade, at $22.85\ mm$, is set as the characteristic length (l). The characteristic Reynolds number is calculated to be $1.6 * 10^5$.

5.4.2. Boundary Conditions

Characteristic parameters	Value
Velocity	$12\ m/sec$
Turbulence intensity	0.1%
Turbulence length scale	$1\ mm$

Table 5.9: Characteristic parameters at pressure velocity inlet

PowerCASE creates a boundary condition for each face of every solid defined in the simulation. The boundary conditions can be edited to meet the requirements of the simulation, for the present simulation two types of boundary conditions are used and are defined as follows:

- **Standard wall:** The standard adiabatic (no-slip) wall simulates a passive wall and has been used to define the propeller geometry in the simulation.

- **Pressure and velocity inlet:** A solid box enclosing the entire simulation domain is created at VR region 0. The box acts as a pressure and velocity inlet for the simulation with a user-defined flow direction. It enables the face upstream of the propeller to function as an inlet and the one downstream to act as an outlet. Table 5.9 defines the parameters used to initialize the domain; the pressure and temperature are the same as in Table 5.8.

5.4.3. Time convergence

Section 4.3.2 lists the criteria for selecting the transient time for the simulation. The mean chord length (l) of the propeller was chosen as the reference length of the object being analyzed, and at a free stream velocity of $U_\infty = 12\ m/sec$, the transient time was calculated to be $2 * 10^{-3}$ seconds. Based on the requirements stated in point 2, for an initial flow domain of length (L) $= 0.3\ m$ the transient time was calculated to be $2.5 * 10^{-2}$ seconds.

The C_T value for 0^o and 15^0 AoA have been analyzed to check for time convergence of the simulation, see Fig. 5.10. The figure shows the values have converged well before the allotted 0.02 seconds. The fluctuation in the C_T values, with respect to the mean C_T, for 0^o and 15^o AoA case is calculated to be 0.7% and 1.3% respectively. Based on the above values, 0.02 seconds or two propeller rotations was chosen as the transient time of the simulation.

5.4.4. Measurements

CFD simulations can sample multiple parameters over the entire flow domain, producing several hundred gigabytes of data. Hence, a crucial aspect is to define the sampling domain, duration, and parameters of the simulation. It requires a trade-off between the available computational resources

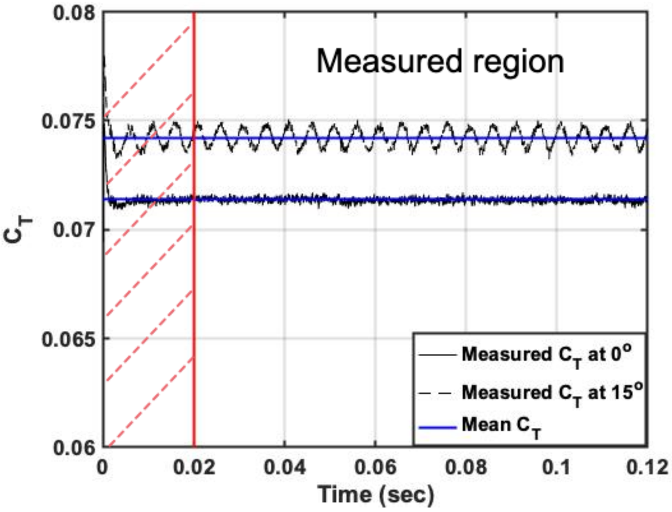

Figure 5.10: Time convergence of C_T value at medium resolution at 0^o AoA

Measurement type	**Measurement duration** (Seconds)	**Sampling frequency** (Hz)
Transient flow	0.05	$7,200$
FWH solid surface	0.1	$3.6 * 10^5$
FWH permeable surface	0.1	$9.1 * 10^4$
Forces	0.12	$1.8 * 10^5$

Table 5.10: Measurement type for the simulation domain; Sampling frequency for the medium resolution setup

and the measurements required to understand the flow characteristics. The measurements saved for all simulations during this study are shown in Table 5.10.

Transient Flow: The transient flow measurement records the fluid and surface variable within a volume enclosed by it. Fig. 5.11 shows the part (in pink) used to define the transient measurement volume. The cylinder has a volume of $5.9 * 10^{-2}\ m^3$, and extends from $z/R = -3.3$ in front of the propeller plane to $z/R = 2$ aft of it. It samples and saves parameters such as density, velocity, vorticity, forces (only for surface), and pressure. The sampling frequency of $7,200\ Hz$ gives it a polar resolution of 5^o.

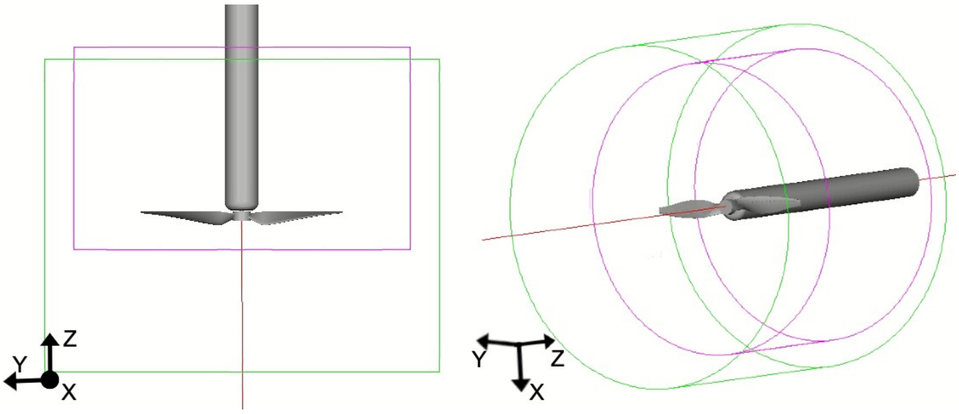

Figure 5.11: Fluid measurement setup; transient measurement volume (pink), VR 10 (green)

FWH solid surface: The FWH solid surface samples the pressure.

FWH permeable surface: It samples the pressure, density, and velocity over its surface without influencing the flow.

Forces: The forces measurement type samples the forces and moments experienced by the propeller blade surface.

5.5. Experimental setup

The experimental setup designed by Edoardo Grande of the TU Delft aeroacoustics group is used for validating the computational results. This section provides an overview of the experimental setup that has been used for the purpose. The setup consists of a twin-bladed propeller, as reported in Section 5.1, supported by a strut enclosed in a nacelle placed at the TU Delft anechoic wind tunnel. The main difference between the experimental and the computational propellers is the absence of a zig-zag trip on the experimental setup. The zig-zag trips could be a potential source of variation in the aerodynamic and acoustic result and shall be discussed further in Chapter 6.

For the acoustic measurements, two microphone arrays are placed in the wind tunnel to perform beam-forming (Array 1) and find the directivity of the noise (Array 2). In the computational study, acoustic data is compared by replicating Array 2 from the experimental setup. Mic 5 on Array 2 is located at a distance of $1.5\ m$ from the propeller axis (at 0^o AoA). The array has a radius of 3.5 times the propeller diameter, measured at a distance of $45\ cm$ from the center of the propeller axis. Tables A.1 and A.2 provides the exact locations of the microphones used in Array 2 in the default/aircraft coordinate system used in this thesis.

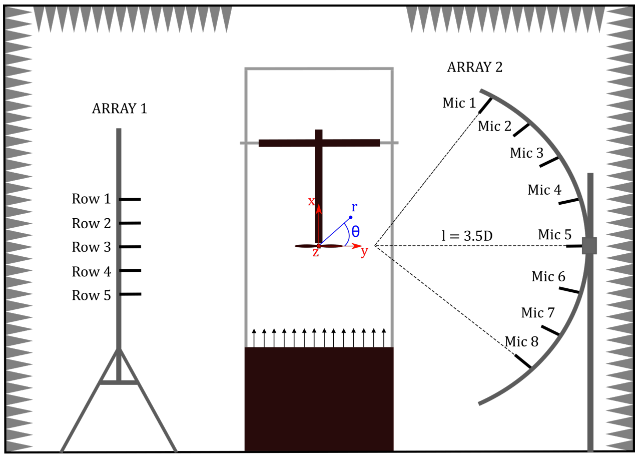

Figure 5.12: Experimental Setup

6

Resolution Study

The resolution of the mesh affects the ability of the solver to resolve the flow field. It impacts the qualitative and quantitative solutions of the simulation. Hence, it is vital to check if the results are affected by the resolution or independent of it. The mesh resolution requirements of a simulation are dependent upon inflow and operating conditions. As a result, change in the operating condition such as the AoA demands a separate resolution study. For this thesis, resolution studies have been carried out for 0^o and 15^o AoA. The variation in aerodynamic and acoustic properties with the resolution has been discussed in Section 6.1, and Section 6.2. Results have also been compared with experimental data where possible.

6.1. Aerodynamic study

Thrust and torque are the main aerodynamic parameters for evaluating propeller performance. These quantities act as the base quantity for deriving other parameters like propeller power and efficiency. Hence, the mean values for the coefficient of thrust (C_T) and torque (C_Q) have been selected for the resolution study. The size of the smallest voxel halves between the coarse and the fine resolution, see Table 5.4. As a result, the number of fine equivalent voxels quadruples, causing a significant rise in computational cost, making it imperative to study the corresponding impact on the accuracy.

Refinement case	0^o	Relative % change	15^o	Relative % change
Coarse	$6.69 * 10^{-2}$	-	$6.96 * 10^{-2}$	-
Medium	$7.14 * 10^{-2}$	6.3	$7.42 * 10^{-2}$	6.2
Fine	$7.16 * 10^{-2}$	0.3	$7.44 * 10^{-2}$	0.3

Table 6.1: Variation in C_T value with grid resolution for 0^o and 15^o AoA; Relative % change measured between subsequent grid resolutions

The first parameter that has been studied is C_T. The flow field close to the surface of the blade influences the value of C_T. As a result, the accuracy with which the mesh can resolve the flow field plays a critical role in determining the C_T value. Table 6.1 shows the variation in mean C_T value with AoA. The "%" change in C_T value with the resolution is constant for different AoA. It implies that for the given range of AoA, the mesh resolution is sufficient to capture the flow fluctuation with the change in AoA. The value of C_T varies by more than 6% between the coarse and medium resolution. In this study, a tolerance of 2.5% is taken as the standard to show grid convergence. The variation between coarse and medium resolution is much higher than the proposed value, meaning that the results are mesh-dependent. The change in C_T between the medium and fine resolution is 0.3%, lying well within the tolerance range to show that the solution is independent of the grid size in the simulation, see Fig. 6.1a.

A deeper analysis has been performed to understand the cause of change in C_T value with grid resolution. Fig. 6.1b and Fig. 6.1c, show the spanwise variation in the mean C_T value with AoA. It can be seen that the C_T value of the coarse resolution begins to diverge from the medium and fine resolution towards the tip of the propeller ($r/R = 0.7$). The mean difference in the sectional C_T value at the tip region ($r/R = 0.8$ to 1) is around 16% between the coarse and the medium resolution setup for the two AoAs. The propeller blade experiences the highest velocity due to the rotation of the propeller at the tip region. It results in significantly higher variation in the flow field compared to the root and mid-span section of the propeller blade. The coarse mesh is unable to resolve these variations in the flow field, which results in the underprediction of the velocity magnitude around the propeller blade causing a reduction in the calculated C_T value. The phenomenon can be visualized using the Lambda-2 vortex criterion (Λ_2), which uses a three-dimensional velocity field to identify vortices using a vortex core line detection algorithm. Fig. 6.2, visualizes the vortices close to the propeller blade surface at $\Lambda_2 = -1*10^7$ $1/sec^2$. It can be seen through the figure that the vortices detected by the Λ_2 criterion are significantly larger than the medium and fine resolution setup. The large size is a result of the higher jump in velocity experienced while calculating the velocity field due to the larger grid size. Signifying the inability of the grid resolve the small-scale fluctuation in the flow field.

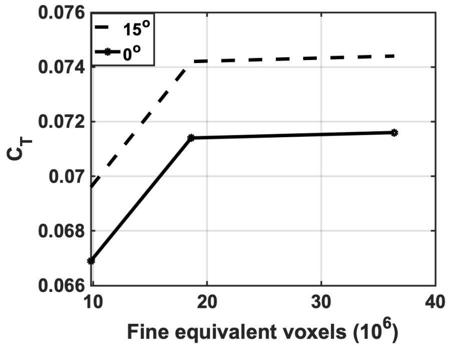

(a) Variation of overall C_T with grid resolution

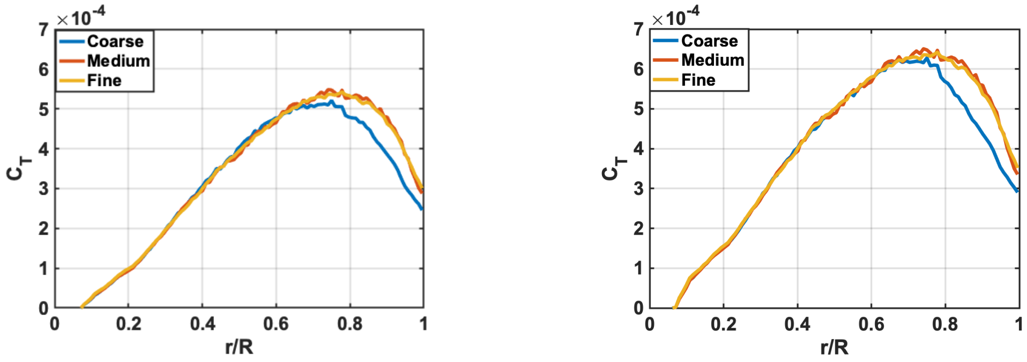

(b) Variation of C_T across blade span with grid resolution at 0^o AoA (c) Variation of C_T across blade span with grid resolution at 15^o AoA

Figure 6.1: Variation of C_T value with grid resolution

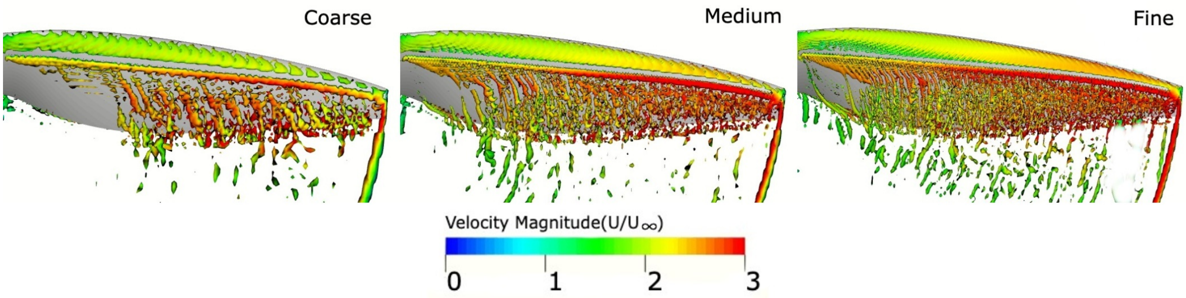

Figure 6.2: Vortex visualization for different resolution at $\Lambda_2 = -1 * 10^7$ $1/\text{sec}^2$ for $\alpha = 15^o$; Suction side of propeller blade.

The next parameter that has been studied is C_Q. It is a measure of the resistance to rotation experienced by a propeller and determines the power required to drive it. The value of C_Q varies by around

4% between coarse and medium resolution at 0^o AoA and 5% at 15^o AoA. The change in C_Q value is limited to about 2% between the medium and fine resolution setup for both AoAs, see Fig. 6.3a. Analyzing the span-wise distribution of C_Q shows that the coarse resolution slightly over predicts the torque value in the propeller mid-span ($r/R = 0.4 - 0.7$), and the value is under-predicted in the tip region, as shown in Figs. 6.3b and 6.3c. The observed variation can be explained using the same hypothesis proposed for the observed variation in C_T. The value of aerodynamic forces shows a good convergence for the medium resolution setup based on a computational cost vs. accuracy tradeoff of the medium resolution setup is a viable choice for aerodynamic analysis. After verifying that the aerodynamic results are independent of the grid size, they are validated against experimental data.

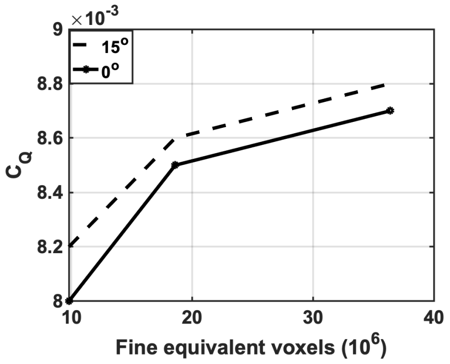

(a) Variation of overall C_Q with grid resolution

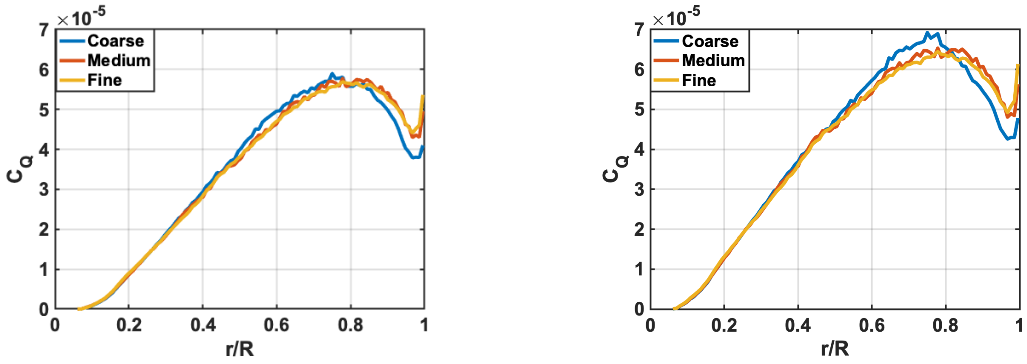

(b) Variation of C_Q across blade span with grid resolution at 0^o AoA (c) Variation of C_Q across blade span with grid resolution at 15^o AoA

Figure 6.3: Variation of $C_Q$value with grid resolution

Table 6.2 presents the comparison between experimental and computational force coefficients. The C_Q value has been over-predicted in the simulation by $9 - 10\%$, whereas the C_T value is underpredicted by 8.5%. The difference in C_Q value can be associated with the different boundary-layer conditions over the experimental and computational propellers. In the computational setup, the boundary layer is forced to transition using a zig-zag strip, whereas the flow is allowed to transition naturally in the experiment. It could potentially mean that the flow remains laminar in the experimental case for a significantly higher percentage of the chord length than in the simulation. Turbulent BL exerts higher shear stress on the propeller surface and produces a higher skin friction drag than laminar BL. Therefore, justifying the variation in C_Q value between the experimental and computational results. The C_T value is dependent primarily upon the lift produced by the propeller blade section, which in turn depends upon the pressure distribution over the blade surface. The presence of a trip acts as an obstruction to the flow over the propeller blade surface resulting in a jump in the C_P value on the suction side. This in turn could impact the overall pressure distribution over the propeller blade surface.

6.2. Aeroacoustic study

Understanding the acoustic characteristics of the propeller is a critical part of this study. Hence, it is vital to study the impact of FWH integration surface and grid resolution on the acoustic results. A power spectrum (PS) analysis is performed on the noise signal to examine its tonal and broadband content. It

	0^o			15^o		
	Experimental	Computational	Variation	Experimental	Computational	(%)
C_T	$7.8 * 10^{-2}$	$7.1 * 10^{-2}$	-8.5%	$8.1 * 10^{-2}$	$7.4 * 10^{-2}$	-8.4
C_Q	$7.7 * 10^{-3}$	$8.5 * 10^{-3}$	9.3%	$7.7 * 10^{-3}$	$8.6 * 10^{-3}$	10.6

Table 6.2: Force comparison between experimental and computational result; Variations measured wrt. experimental and simulation values

calculates the energy within the specified frequency bandwidth (Δf) to generate a spectrum plot of the signal. As opposed to power spectral density (PSD) which calculates the energy of the signal per unit frequency. The advantage PS offers is that changing the frequency bandwidth (Δf) of the analysis does not affect the tonal noise levels in a PS analysis, while in PSD the tonal noise levels change with Δf. As tonal noise tends to dominate the OASPL in propeller noise, using PS makes it easier to compare noise levels. In this thesis, the PS analysis has a frequency bandwidth (Δf) of $20\ Hz$ and a range of $40 - 10{,}000\ Hz$.

This section is divided into two sub-parts Section 6.2.1 analyses the acoustic results from solid (FWH SLD) and permeable(FWH PRM) surfaces and decides upon the FWH formulation that shall be used throughout this thesis. Section 6.2.2 studies the impact of grid resolution on the acoustic results and decides upon the grid resolution that shall be used for further analysis.

6.2.1. FWH surface selection

Section 4.3.1 discussed how the FWH analogy is implemented in PowerFLOW® through the formulation of solid and permeable integration surfaces. In this section, the far-field noise captured by the integration surfaces is calculated using two circular microphone arrays described in Section 5.3. A comparison between their OASPL is performed, followed by a power spectrum analysis to understand the observed variations.

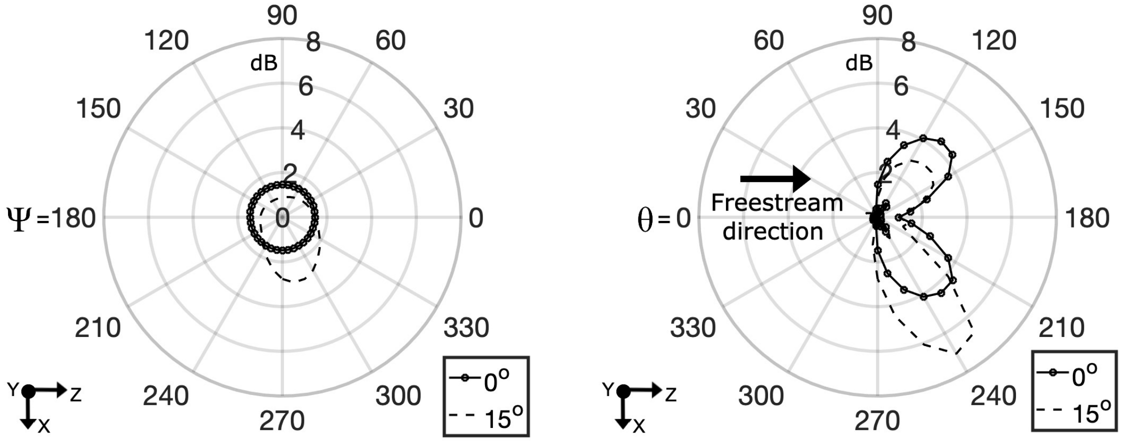

(a) Difference around propeller plane (b) Difference along axial direction

Figure 6.4: Difference in OASPL between solid and permeable FWH integration surface

The OASPL is a measure of the total energy contained in the spectrum. To compare the noise signal captured by the two integrating surfaces, the OASPL for a frequency range of 40 - $10{,}000\ Hz$ is calculated using the circular microphone arrays. It is observed that the OASPL of the solid integration surface is higher than that captured by the permeable surface. Fig. 6.4, plots the difference in OASPL (FWH SLD - FWH PRM) in the propeller plane and along the axial direction. In the propeller plane, at 0^o AoA, the difference between FWH SLD and FWH PRM surface is around $1.4\ dB$, showing little to no variation with azimuthal angle (Ψ). However, at an AoA of 15^o, the difference in OASPL varies by over $2\ dB$ with a change in azimuthal angle. It fluctuates between $0.85\ dB$ at $\Psi = 120^o$ to $2.96\ dB$ at $\Psi = 280^o$, as shown in Fig. 6.4a. In the axial plane, along the free stream direction, the difference in FWH SLD and FWH PRM OASPL acquires a lobular structure. In the top half of the axial plane

($\theta = 0^o \rightarrow 90^o \rightarrow 180^o$), the lobes show a maximum difference of $4.4\ dB$ ($\alpha = 0^o$) and $3.1\ dB$ ($\alpha = 15^o$) at $\theta = 140^o$. The difference increases to $7\ dB$ for $\alpha = 15^o$ at $\theta = 250^o$, while it remains the same for 0^o AoA, $4.4\ dB$ at $\theta = 240^o$, in the lower half of the axial plane ($\theta = 180^o \rightarrow 270^o \rightarrow 0^o$). A common observation from Fig. 6.4a and Fig. 6.4b is that the difference in OASPL increases in the direction of the wake, i.e. the permeable surface underpredicts the OASPL values in the downstream direction.

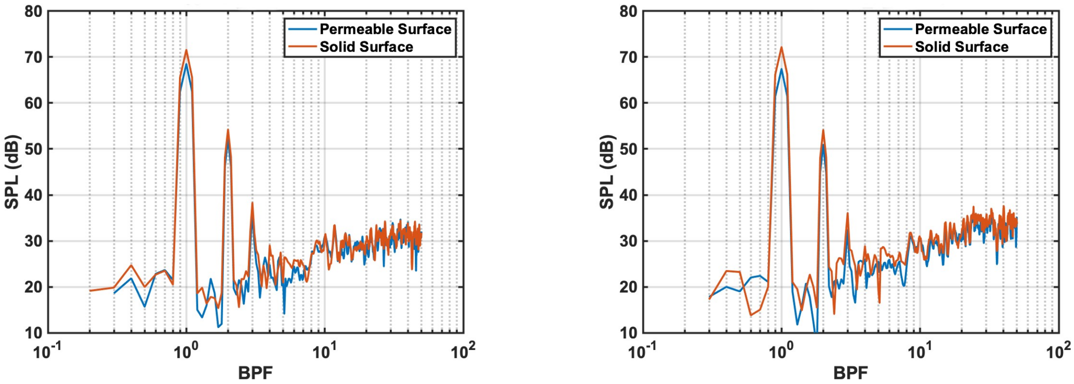

(a) Power spectrum around propeller plane; Ψ = 280^o at 15^o AoA

(b) Power spectrum along axial plane; Θ = 260^o at 15^o AoA

Figure 6.5: Power spectrum of solid and permeable FWH integration surface; Δf = $20\ Hz$

To better understand the cause of this difference in OASPL, a power spectrum analysis is performed on the noise signal. The power spectrum analysis is performed for a frequency range of $40 - 10,000$ Hz using a Hanning window with 50% overlap and a frequency bandwidth Δf of $20\ Hz$, as shown in Fig. 6.5. The power spectrum curves are in good agreement with each other in the high-frequency region. It is because the quadrupole source terms scale to the eighth power of Mach number. Given the low Mach number (< 0.3) of the present simulation, it is not a surprise that the quadrupole sources do not play a dominant role in determining the high-frequency range of the power spectrum. As a result, the inability of FWH-SLD to capture the quadrupole source terms has no impact on broadband noise or the OASPL of the signal. The difference in power spectrum level is primarily observed in the low-frequency region. At $\Psi = 280^o$ ($\alpha = 15^o$) the difference in SPL at 1^{st} BPF is $3\ dB$, which is the same as the total difference in OASPL between FWH SLD and FWH PRM surfaces, as shown in Fig. 6.5a. A similar observation is made along the axial direction as well. Fig. 6.5b show the power spectrum at $\Theta = 260^o$ (for $\alpha = 15^o$), the difference in SPL at 1^{st} and 2^{nd} BPF is about $5\ dB$, whereas the broadband part of the signal are in good agreement.

The computational results clearly show the difference in OASPL measurements of the solid and permeable FWH integration surface. However, these results can not justify the choice of one integration surface over another. Hence, the computational results of both integration surfaces are compared against experimental data obtained by Edoardo Grande. Fig. 6.6 shows the comparison between the noise signals captured by the two FWH integration surfaces and experimental measurements. In the downstream location (Mic number 1), the solid surface is in excellent agreement with the experimental results, whereas the permeable surface under-predicts the OASPL ($f = 40 - 1,000\ Hz$) by $10\ dB$. The results show similar trends observed in the computational results, where the permeable surface underpredicted the tonal component of the propeller noise. Moving in the upstream direction (Mic $1 \rightarrow$ Mic 8), the OASPL values of the solid surface begin to diverge from the experimental results and is in better agreement with the permeable surface. A power spectrum analysis is performed on the noise signal to understand its cause and analyze the energy content in different frequencies.

In the upstream direction at Mic 1 the FWH SDL shows good agreement with the experimental result at $1^{st}$and 2^{nd} BPF, the agreement however deteriorates towards higher harmonics. The higher harmonic tones observed in the experimental data could be attributed to factors such as; i) Proximity of the propeller blades to the wind tunnel shear layer at 15^o AoA; ii) Vibrations in the experimental setup resulting in unsteady loading on the propeller blades; causing higher harmonic noise. These factors are not present in the computational simulation and can justify the observed variation in SPL at harmonics of BPF. Moving downstream, towards Mic 8, the difference in SPL between the experimental and solid surface increases to $7\ dB$ at 2^{nd} BPF, rising to over $20\ dB$ for subsequent harmonics. It

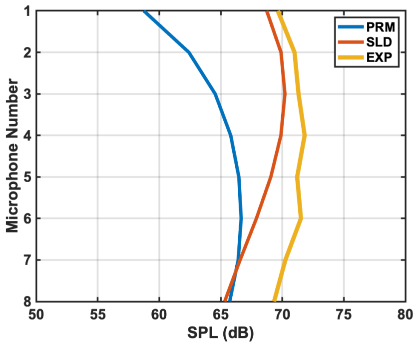

(a) OASPL measurements for $f = 40 - 1,000\ Hz$

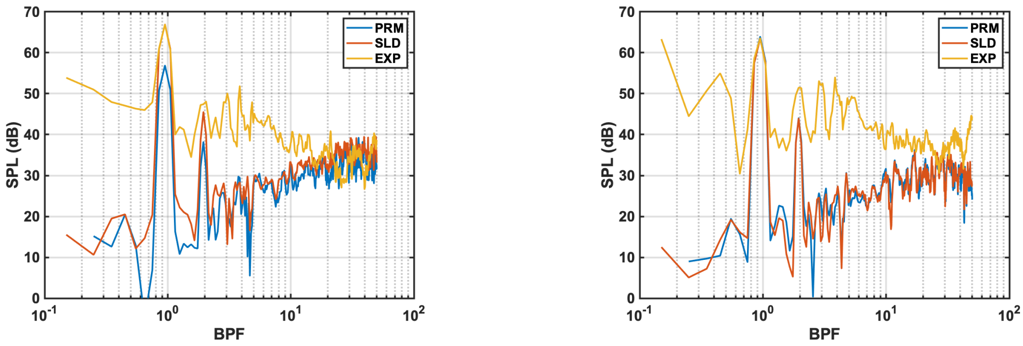

(b) Power spectrum level at microphone number 1; $\Delta f = 20\ Hz$

(c) Power spectrum level at microphone number 8; $\Delta f = 20\ Hz$

Figure 6.6: Comparison between solid (SLD), permeable (PRM), and experimental (EXP) noise data at 15^o AoA

results in the difference in the OASPL values observed in Fig. 6.6a. The FWH PRM surface constantly underpredicts the tones at 1^{st} and 2^{nd} BPF in the downstream direction, and the OASPL value at Mic 1 is $11\ dB$ less than the experimental value. The permeable surface data seems to be corrupted by the propeller wake. Individual analysis of the acoustic data obtained by the three integration surfaces, see Fig. A.4, showed a similar trend of under-predicting tonal noise in the direction of the propeller wake. Consequently, averaging the values from the three FWH PRM surface does little to correct the data.

Through the power spectrum analysis, it is clear that the solid integration surface has the best agreement with the experimental result.It captures the 1^{st} BPF tone to within $1\ dB$ of the experimental measurements at 15^o AoA and has a similar directivity to the experimental values. Hence, the acoustic data captured by the FWH solid surface is used for studying the noise generated by the propeller in this thesis.

6.2.2. Grid selection

The present section analyses the effect of grid resolution on acoustic results. Based on conclusions of Section 6.2.1, the FWH SLD integration surface has been used to analyze the results in this section. The resolution study is carried out for coarse, medium, and fine resolution for microphones placed at $\theta = 90^o$ and 110^o. Fig. 6.7a, shows the variation in OASPL ($40 - 10,000\ Hz$) and SPL at 1^{st} BPF for both the microphones. The OASPL and SPL at 1^{st} BPF vary by less than $0.5\ dB$ between the coarse, medium, and fine resolution setup. At higher frequency, the agreement of SPL deteriorates significantly with the resolution, see Fig. 6.7b. At a frequency range of $1,500 - 2,500\ Hz$, the SPL varies by $6\ dB$ between the coarse and the medium resolution. The variation reduces to $3\ dB$ between medium and fine resolution.

The solid FWH integration surface, due to its proximity to the propeller blade, lies in VR region 12. It ensures that the cutoff frequency for all the resolutions in the setup is above $10,000\ Hz$, hence the variation in sampling frequency can not justify the difference in broadband noise levels with grid resolution. A power spectrum analysis is performed on the pressure values obtained from the propeller blade surface to understand the cause of variation in SPL with grid resolution. A frequency bandwidth (Δf) of $1,000\ Hz$, is used for analysing a frequency range of $1,000 - 10,000\ Hz$. Fig. 6.8a shows the

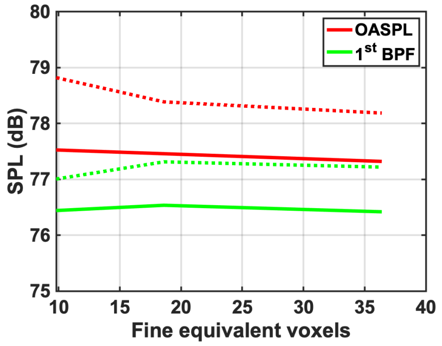

(a) Variation in OASPL and 1^{st} BPF with grid resolution; Solid lines represent $\theta = 90^o$ & dotted line represent $\theta = 110^o$ AoA;

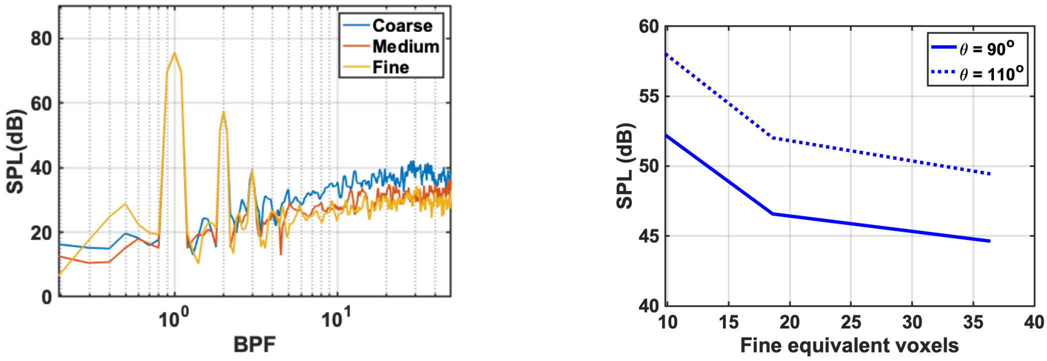

(b) Variation in spectrum level with resolution ($\Delta f = 20\ Hz$, AoA = 0^o, $\theta = 90^o$)

(c) Variation in broadband noise ($1,500 - 2,500 Hz$) with grid resolution.

Figure 6.7: Variation in acoustic result with grid resolution at $\alpha = 0^o$

surface pressure distribution (in dB), obtained for a frequency range of $1,500 - 2,500\ Hz$ for coarse, medium, and fine resolution setup. It is observed that the blade surface pressure at the trailing edge for higher frequencies $(1,000 - 10,000\ Hz)$ increases with decreasing resolution. The surface pressure fluctuation at the trailing edge of a propeller is a significant source of broadband noise [9]. These fluctuations are produced due to the downstream convection and formation of a turbulent boundary layer over the blade surface. A plausible explanation for the variation in broadband noise with the resolution is that the coarse resolution setup is unable to resolve the small-scale turbulence present in the turbulent boundary layer. The larger turbulent structures result in higher pressure fluctuations as they convent downstream from the propeller blade trailing edge into the wake, resulting in higher broadband noise. Fig. 6.8b attempts to picture this phenomenon by overlaying vortices visualized by Λ_2 vortex criterion. It can be observed that at $\Lambda_2 = -4 * 10^7\ 1/sec^2$ the coarse resolution is unable to resolve the smaller flow structures like the medium and the fine resolution setup. The same analogy can be applied to the flow structures present in the turbulent boundary layer as well. Another reason for it could be the low trip resolution for the coarse mesh. With only two voxels to cover the trip, the trip step might not be completely resolved in the simulation affecting the flow transition and consequently the turbulent BL.

From the OASPL values, it can be stated that the coarse resolution is sufficient for capturing the acoustic data. However, since the aerodynamic data converges at medium resolution and the change in broadband noise is also significantly lower at this resolution, the medium resolution setup is used for analyzing the acoustic results in the present study.

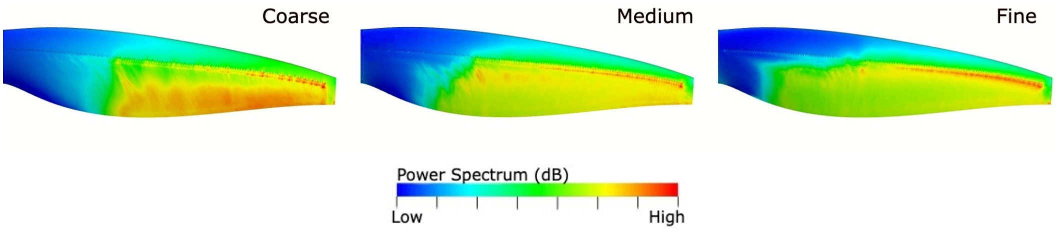

(a) Surface pressure fluctuation (dB) on the suction side of the propeller blade.

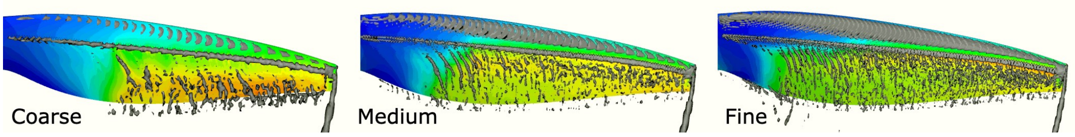

(b) Surface pressure fluctuation (dB) map with vortex visualisation at $\Lambda_2 = -4 * 10^7 \ 1/\text{sec}^2$

Figure 6.8: Surface pressure fluctuation (dB) at 0^o AoA for a frequency range of $1,500 - 2,500 \ Hz$; contour range 60 dB, suction side of the propeller blade.

7

Results

This chapter discusses the aerodynamic and acoustic results obtained from simulations. It is divided into three sections, Sections 7.1 and 7.2 discusses the aerodynamic results in terms of the forces experienced by the propeller blade and flow field analysis, and Section 7.3 discusses the aeroacoustic results.

7.1. Propeller force

The forces experienced by a propeller depend upon its RPM and inflow conditions. When the propeller operates at a non-zero AoA, relative to the freestream, the freestream velocity consists of components that act parallel and perpendicular to the propeller disc. These components change the effective blade AoA of the propeller, causing a variation in blade loading around the azimuthal (Ψ) plane. Operating at $6,000$ RPM at a freestream velocity of $12\ m/sec$, changing the AoA from 0^o to 15^o results in an increase in mean thrust by 3.87%, while the torque required increases by 1.16%. It shows that the torque values are less sensitive to the changes in AoA when compared to thrust values. As a result, the propeller experiences a net increase in its propulsive efficiency with a change in AoA. Table 7.1, shows the mean thrust, torque, and efficiency values obtained for the two AoAs.

	15^o AoA	0^o AoA	Difference (%)
C_T	$7.4 * 10^{-2}$	$7.1 * 10^{-2}$	3.87
Thrust (N)	7.11	6.84	
C_Q	$8.6 * 10^{-3}$	$8.5 * 10^{-3}$	1.16
Torque (Nm)	0.25	0.24	
η (%)	54.88	53.66	1.22

Table 7.1: Mean thrust, torque and propeller efficiency value for propeller; % difference calculated between 0^o and 15^o AoA

Operating at an AoA, the propeller plane can be classified into two main parts, the advancing blade side, and the retreating blade side. The classification is based upon the variation in resultant velocity and AoA experienced by the propeller blades due to the change in freestream velocity components around its azimuthal position. On the advancing side, the propeller experiences an increase in its resultant velocity and AoA over the blade section, resulting in higher thrust. The conditions reverse on the retreating side. Appendix A, explains the concept of advancing and retreating side in detail through velocity triangles. The simplistic calculation based on the propellers velocity triangles identified that the propeller blade operating at $\Psi = 270^o \rightarrow 0^o \rightarrow 90^o$ (advancing side) will experience higher blade loading than propeller operating at $\Psi = 90^o \rightarrow 180^o \rightarrow 270^o$ (retreating side).

Fig. 7.1, quantifies the change in sectional C_T and C_Q values as the propeller blade rotates around the propeller plane. As the sectional variation of C_T around the propeller plane remains constant at 0^o AoA, the value at $\Psi = 0^o$ is chosen as the reference value. For 15^o AoA, $\Psi = 0^o$, 90^o , 180^o, and 270^o are chosen to study the variation in sectional thrust and torque values with AoA. The propeller blade is divided into three sections, root ($r/R = 0 - 0.4$), mid-span ($r/R = 0.4 - 0.8$), and tip ($r/R = 0.8 - 1$), to get better insight into how the aerodynamic forces vary across the blade. At $\Psi = 0^o$ for 15^o AoA, the propeller blade experiences significantly higher thrust and torque relative to 0^o AoA. The thrust values at the root vary by 45% it gradually reduces to 22% at the mid-span and 16% at the tip. A similar observation is made at $\Psi = 180^o$. The thrust values are lower by 32% at the root, 13.8% at mid-span, and 9.3% at the tip relative to 0^o AoA. Though the sectional variation in thrust values is expected a variation of over 30% at the root section deserves further examination.

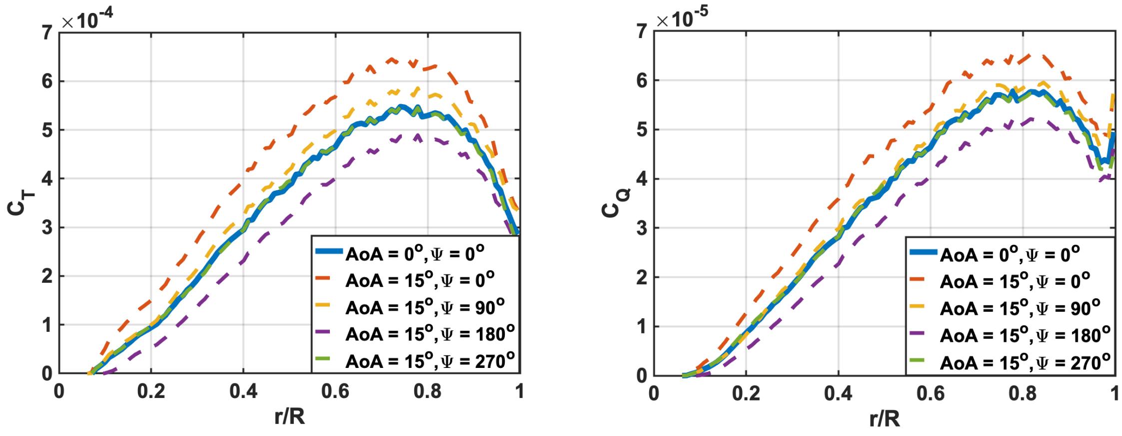

(a) C_T value across blade span at different Ψ for 15^o and 0^o

(b) C_Q value across blade span at different Ψ for 15^o and 0^o

Figure 7.1: Variation in sectional C_T and C_Q with azimuthal angle (Ψ) for $\alpha = 0^o$ and 15^o

The thrust produced is directly dependent upon the lift (C_l) and drag (C_d) force experienced by the propeller blade section. The sectional C_l and C_d value is a function of the resultant velocity over the propeller blade section. It is determined by the components of the freestream velocity and local rotational speed of the propeller and influences the AoA and Reynolds number of the blade section. At the tip region, the rotational speed dominates over the freestream velocity component. Consequently, the effect of change in propeller AoA is reduced on the sectional blade AoA towards the tip region, see Fig. A.5. At the root section, the velocity induced by the propeller rotation is the smallest. It results in the root section experiencing the highest variation in resultant velocity due to AoA. The change in resultant velocity also influences the Reynolds number. Studies into the aerodynamic characteristic of low Reynolds number airfoil show an exponential rise in C_l/C_d value in the Reynolds number range of $5 * 10^4$ to 10^5 [44]. In this case, the average Reynolds number in the root region at $\Psi = 0^o$ is $8.5 * 10^4$ at 0^o it increases to $9.7 * 10^4$ for 15^o. Fig. 3.9b shows that this region experiences one of the highest increases in C_l/C_d value with Reynolds number. Hence the variation of thrust value by over 30% at the root section can be justified by the combined influence of the Reynolds number effect and higher variation in the region.

The above paragraph explained the variation of aerodynamic forces along the blade span. However, it does not quantify the net effect of these forces on the propeller plane. Fig. 7.2a shows the total thrust force produced by a propeller blade as it rotates around the propeller plane. At 0^o AoA the blade produces a steady thrust of 3.4 newtons, at 15^o AoA the thrust force varies between 2.8 newtons at $\Psi = 198^o$ (minimum) to 4.3 newtons at $\Psi = 17^o$ (maximum). Showing a 35% change in loading around the azimuthal position. The maximum and minimum loads experienced by the propeller blade lead to cyclic loading of the propeller, as seen in Fig. 7.2b. However, upon analyzing Fig. 7.2b it is observed that the net fluctuation in thrust force for the propeller around the azimuth is less than 1% for 15^o AoA. It is because the point of minimum and maximum loading have an azimuthal distance of 180^o. As a result, for a twin-bladed propeller, the net force balances out between these locations.

7.2. Flow field analysis

The propeller flow field is analyzed by visualizing the velocity field and vortices produced by the propeller. The velocity field is obtained by averaging the flow field values for a period of five propeller rotations. To visualize, the vortex field a phase-locked analysis is performed on the transient flow

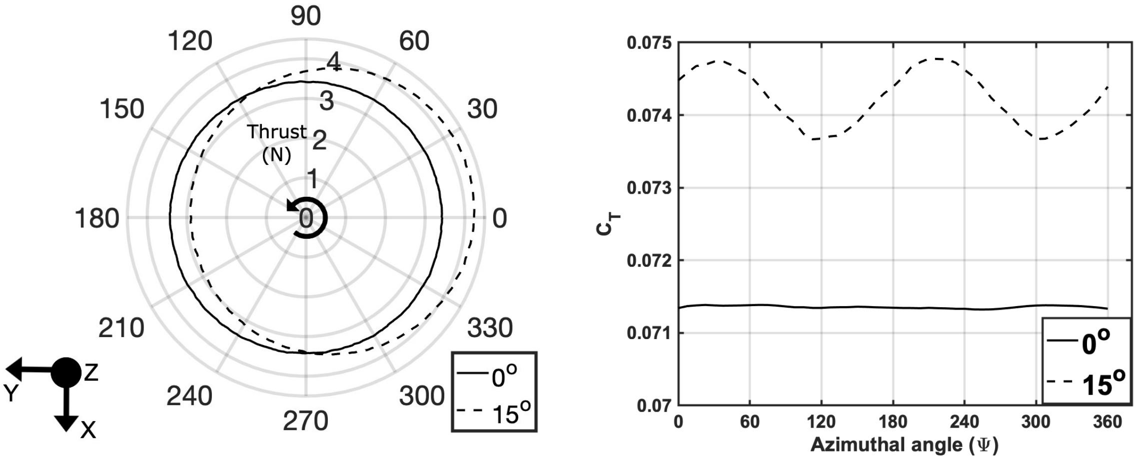

(a) Net thrust force produced by a single propeller blade with changing azimuthal angle (Ψ)

(b) Propeller C_T per rotation

Figure 7.2: Change in thrust values with azimuthal angle (Ψ)

field. The vortices are then detected using the Lambda-2 vortex criterion. The analysis is performed in the axial direction and along the propeller plane of symmetry. Section 7.2.1 discusses the changes in velocity, and Section 7.2.2 discusses the changes in vortices produced by the propeller. In Section 7.2.3 the effects of the change in AoA on the surface pressure fluctuations of the blade surface are analyzed.

7.2.1. Velocity field

The flow velocity in the propeller slipstream is an important parameter to describe the flow field in that region. It captures the variations caused due to the addition of momentum into the flow field by the propellers. In this section, the averaged velocity field behind the propeller is analyzed to quantify and understand the effect of AoA on the flow field. The transient flow measurement has been averaged out for five propeller rotations to obtain the mean flow presented in this section. The velocity contours so obtained are captured along the propeller plane of symmetry as well as the axial direction and analyzed.

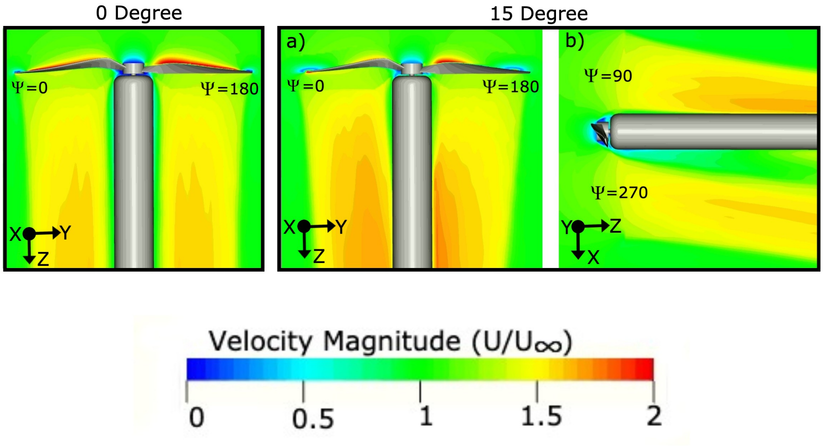

Figure 7.3: Axial velocity profile for 0^o and 15^o AoA

Fig. 7.3 captures the velocity profile along the propeller plane of symmetry. At 0^o AoA, the propeller wake is symmetric about the XZ and YZ planes. Hence, a single plane is sufficient to visualize the velocity field. Operating at 15^o AoA, varying blade loads about Ψ leads to a non-symmetric velocity field. Hence, both XZ and YZ planes are used for analyzing the velocity field for 15^o AoA. The velocity field has been non-dimensionalized using the free stream velocity ($U_\infty = 12\ m/sec$ along the z axis). Operating at $6,000$ RPM, at 0^o AoA, the propeller accelerates the flow to 1.4 times the freestream velocity at $z/R = 0.2$, where z is the distance along the positive Z-axis, and R is the radius of the propeller. As the wake travels downstream, the trailing edge vortices present in the flow start to break down and transfers energy into the flow field, which is partially responsible for the increase in the slipstream velocity to 1.6 time the freestream velocity at $z/R > 1$. At 15^o AoA, the non-axial free stream velocity causes the propeller blade to experience varying loads around the propeller plane and deflects the wake produced. To capture these phenomena the propeller velocity profile is captured along the YZ as well as the XZ plane Fig. 7.3 a) and b) respectively. The results in Section 7.1 showed that the propeller experiences higher loading at $\Psi = 0^o$ (advancing side) than at $\Psi = 180^o$ (retreating side). The asymmetry in loading around the propeller plane results in an asymmetric velocity field about the propeller axis, as seen in Fig. 7.3 a). The velocity magnitude is up to 6% higher at $z/R = 0.3$ in the advancing side compared to the retreating side. As the wake travels downstream, the velocity magnitude close to the nacelle on the retreating side shows a significant rise (around two times the freestream velocity) compared to the advancing side. It is because of the energy transferred into the flow by the root vortex interacting with the nacelle. This interaction is caused by the deflection of propeller wake by the oncoming freestream at 15^o AoA, as seen in Fig. 7.3 b).

The mean velocity field is captured at different locations along the axial direction to develop a deeper understanding of how the flow develops along the axial direction. Fig. 7.4 shows the evolution of the velocity field at $z/R = 0.2, 0.6$ and 1 for 0^o and 15^o AoA. The velocity magnitude is visualized for a range of $12 - 20\ m/sec$, as it highlights the variations in the mean velocity field. The white spots in the velocity plots are regions where the mean velocity is less than the freestream velocity.

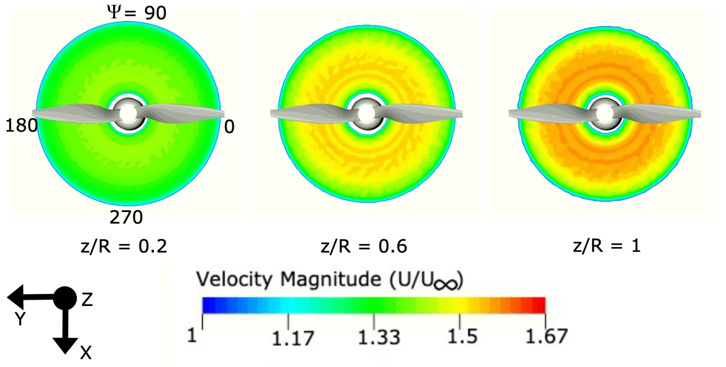

(a) 0^o AoA

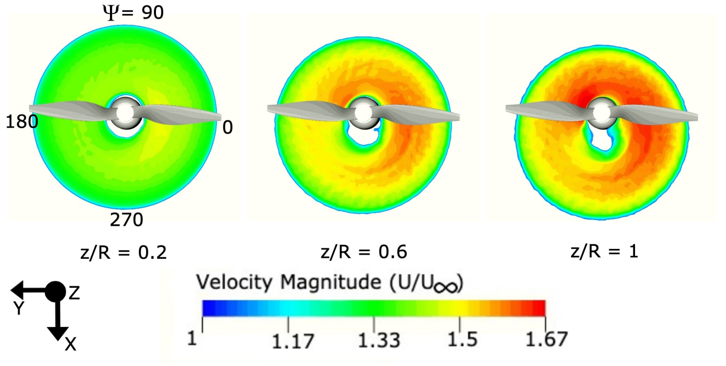

(b) 15^o AoA

Figure 7.4: Velocity magnitude at different radial position along the propeller axis

Fig. 7.4a captures the mean velocity field at 0^o AoA for the above-mentioned axial locations. At $z/R = 0.2$, the mean velocity is 1.3 times the freestream velocity in the wake of the propeller. It leads to a 9% contraction in the propeller stream tube compared to the propeller diameter. As the wake moves downstream, the trailing edge vortices produced by the propeller blades dissipate and transfer energy into the wake. At 0^o AoA, the root and tip vortices produced by the propeller remain coherent in the entire measurement region. It prevents the flow in the freestream from mixing with the propeller wake. Which results in the formation of two distinct velocity bands in the propeller was at $r/R < 0.2$ and $r/R > 0.8$, as seen in Fig. 7.4a.

Fig. 7.4b shows the velocity field in the wake of the propeller at 15^o AoA. A distinguishing feature of the flow field at 15^o is the asymmetric nature of the velocity field. At $z/R = 0.2$ the velocity field starts to show a higher mean velocity close to the root region ($r/R = 0.2 - 0.4$) on the advancing side of the propeller plane ($\Psi = 270^o \rightarrow 0^o \rightarrow 90^o$). As the wake moves downstream the asymmetric in the velocity field becomes more evident. Examination of Figs. 7.2a and 7.4b establishes a clear correlation between the influence of blade loading on the downstream velocity profile. As the blade loading reduces between $\Psi = 180^o$ to 240^o so does the mean velocity magnitude. The inflow angle of the freestream velocity deflects the propeller wake, which results in the break down of the root vortex around $\Psi = 0^o \rightarrow 90^o \rightarrow 180^o$. It causes the observed rise in mean velocity close to the nacelle. The nature of the vortices shed by the propeller, and the impact of AoA shall be discussed in more detail in Section 7.2.2.

7.2.2. Vortex field

In the present section snapshots of the instantaneous flow field are captured to analyze the vortices being shed by the propeller. The analysis is carried along the propeller axis on the XZ plane of symmetry. A phase-locked analysis is carried out on the transient flow field for a period of five propeller rotations to isolate the periodic fluctuations in the flow field. A measuring window spanning from $z/R = -0.1$ (ahead of the propeller) to $z/R = 1.7$ (behind the propeller) is used to capture the vortices. The vortices being produced by the propellers are visualized using the Lambda-2 (Λ_2) vortex visualization technique.

Fig. 7.5 captures the evolution of the vortices produced by the propeller along the freestream. The vorticity magnitude (ω) is non-dimensionalized using a reference value of 500, which is obtained by dividing the freestream velocity of the simulation by the characteristic length. At 15^o, due to the change in inflow angle, the propeller wake is pushed towards the positive X-axis. The root vortex and nacelle interaction result in the root vortex breaking down into smaller vortical structures. The inflow angle also results in the formation of stronger vortices at the propeller hub. The two phenomena create a region of high vorticity at $z/R = 0.4$ to 0.8. Despite the high vorticity, it has minimal contribution to the broadband noise due to the low flow velocity. The breaking up of the root vortex and downward deflection of the tip vortices can be visualized by Fig. 7.6.

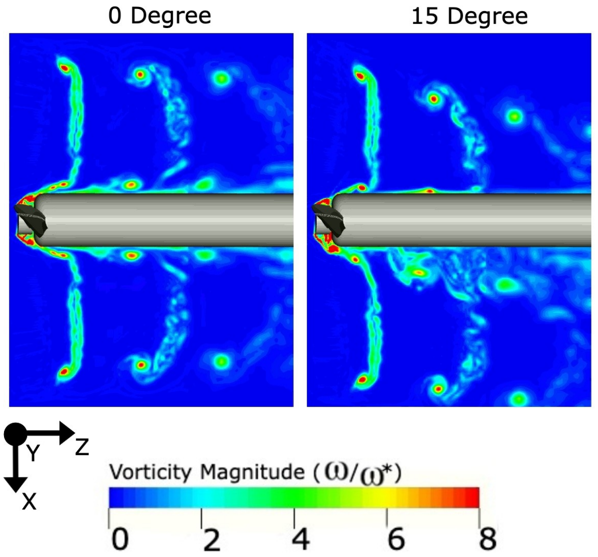

Figure 7.5: Vorticity magnitude along the propeller axis

Using the Λ_2 vortex criterion the vortices in the fluid domain are identified using the three-dimensional velocity field. In Fig. 7.6 the Λ_2 value is set at $-1 * 10^6$ $1/sec^2$, the color contour represents the velocity magnitude of the shed vortex. The tip vortex exhibits a similar structure and velocity profile at 0^o and 15^o AoA. The only difference is the downward deflection of the vortices and the breaking up of the root vortices, which have been discussed in the previous sections. To understand the nature of the trailing edge vortices a closer look is taken at the propeller blade section for 15^o and 0^o AoA at $\Psi = 0^o$. The trailing edge vortices at the tip region ($r/R > 0.8$) of the propeller convect at three times the freestream velocity and exhibit the same characteristics for 0^o and 15^o AoA. At the root section ($0.0 > r/R > 0.4$), there are visible differences in the vortices being shed. At 15^o the trailing edge vortices are convected at approximately 2.5 times the freestream velocity, whereas it is less than two times the freestream velocity at 0^o. The vortex structure and shape at the trailing edge also differ for 0^o and 15^o AoA. The vortices produced at the leading edge of the propeller blade experiences higher convective velocity at 15^o AoA than at 0^o. It could lead to variation in surface pressure fluctuation over the blade surface, which in turn can affect the noise produced by the propeller blade. The following section discusses the variation in blade surface pressure fluctuation for 0^o and 15^o AoA.

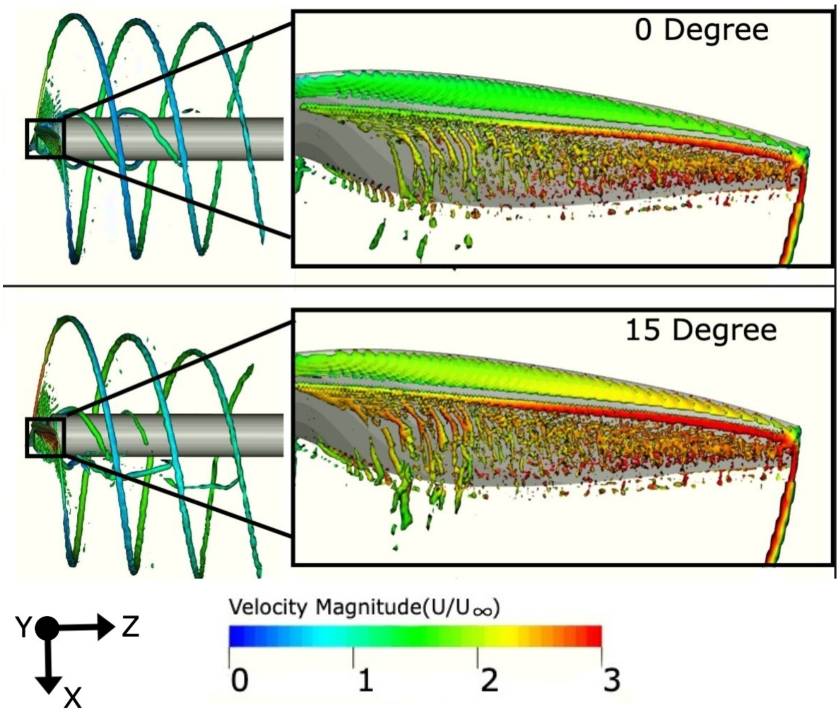

Figure 7.6: Vortex visualization for 0^o and 15^o AoA at $\Lambda_2 = -1 * 10^6\ 1/sec^2$ and $\Psi = 0^o$

7.2.3. Surface pressure fluctuation

The force fluctuations over a propeller blade surface due to fluctuating surface pressure is a dominant acoustic source. In this section, the variation in blade surface pressure fluctuation is analyzed for 0^o and 15^o AoA across the blade span to understand how the AoA impacts the surface pressure fluctuation at different frequencies. The blade surface pressure values are obtained for 0.1 seconds (10 rotations) at a sampling frequency of $3.6 * 10^5\ Hz$. The pressure fluctuations captured are reported in the dB scale set against a reference value of $2*10^{-5}\ Pa$, and the contour plot over the blade surface has a range of $60\ dB$. A power spectrum analysis is performed on the surface pressure values that convert the pressure signal from the time domain to the frequency domain and helps analyze the energy content of selected frequency bands. The analysis is performed for a high-frequency band ($1,500 - 7,500\ Hz$), with a frequency bandwidth (Δf) of $1,000\ Hz$, and a low frequency band ($100 - 700\ Hz$) with $\Delta f = 200\ Hz$. The segregation of the analysis into high and low-frequency helps in understanding the chord and spanwise distribution of the surface pressure fluctuation for different frequency bands and the impact of AoA on it.

For $f = 100 - 300\ Hz$ pressure fluctuations at the leading edge dominate the blade surface pressure fluctuation at 15^o AoA, see Fig. 7.7. It remains a significant source till $f = 500 - 700\ Hz$ at which the low-pressure fluctuation is almost uniformly distributed over the blade surface. At 0^o the contribution of the propeller leading edge to the low-pressure fluctuation is significantly reduced, and the blade

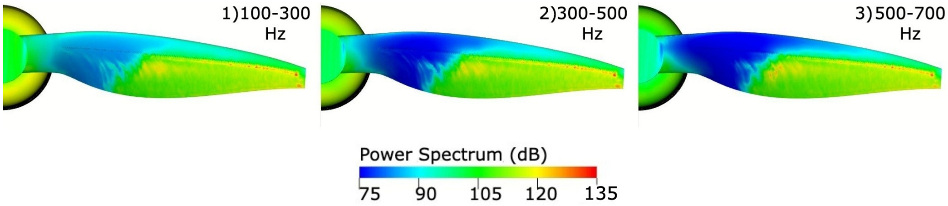

(a) Surface pressure fluctuation (dB) on the suction side of the propeller blade at 0^o AoA

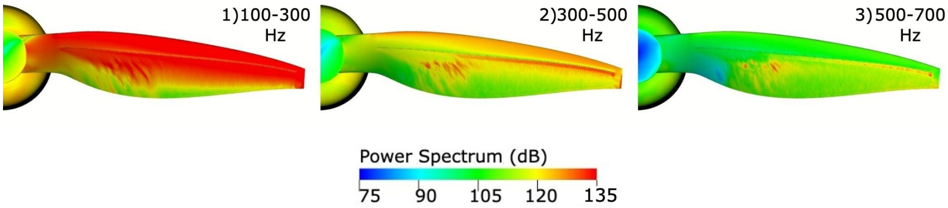

(b) Surface pressure fluctuation (dB) on the suction side of the propeller blade at 15^o AoA

Figure 7.7: Surface pressure fluctuation (dB) at 1^{st}, 2^{nd} and 3^{rd} BPF; contour range 60 dB

section aft of the trip becomes a more dominant contributor. A plausible explanation of this behavior is the change in AoA experienced by the propeller blade around the azimuthal plane while operating at 15^o AoA. The change in AoA results in a periodically varying pressure field over the propeller blade. The leading edge of the propeller experiences the maximum variation in pressure with change in AoA. Justifying the dominating contribution of the leading edge to low-pressure fluctuation. Since a propeller blade operating at 0^o AoA does not experience any such variation about its azimuthal position, there is no significant pressure fluctuation at the blade's leading edge. The root section of the propeller blade is also a region of particular interest. Section 7.1 discusses the significant variation in C_T value at the root section of the propeller blade, Section 7.2.2 also pointed out the difference in vortex structures in the same region. Figs. 7.7a and 7.7b shows the discrepancy in the surface pressure fluctuation for the two AoA at the root region. At 0^o AoA, the root section experiences significantly lower surface pressure fluctuation than 15^o AoA. The difference could be a potential source of noise, which shall be discussed in Section 7.3.

Fig. 7.8 captures the surface pressure fluctuation over the propeller blade surface at $f > 1,000$ Hz contributing to the broadband noise spectrum. For 0^o AoA, the pressure fluctuation over the propeller blade surface does not change significantly with frequency. The pressure fluctuation is at its minimum close to the blade root and increases towards the tip region. The trailing edge of the propeller blade at the tip region experiences maximum pressure fluctuation. Hence, contributing the most to the trailing edge broadband noise produced by the propeller. At 15^o AoA, the pressure fluctuation shows considerable variation, between $1,500 - 4,500$ Hz. The change is minimal at the higher frequency range, $4,500 - 7,500$ Hz, and starts to resemble the pressure fluctuation distribution at 0^o AoA. For the frequency range between $1,500 - 4,500$ Hz, the propeller blade at 15^o AoA experiences a higher pressure fluctuation at the root section than 0^o AoA. The magnitude of the pressure fluctuation reduces with an increase in frequency. However, at 15^o AoA, the trailing edge region towards the propeller tip experiences the highest pressure fluctuation. It is similar in magnitude to that of the propeller blade at 0^o AoA. As this section contributes the most to the broadband part of the acoustic spectrum, it is a possibility that the propeller blades exhibit similar broadband characteristics despite the change in AoA.

7.3. Acoustics

This section analyzes and quantifies the changes that occur in the acoustic characteristic of the propellers with AoA. Section 7.3.1 discusses and quantifies the difference in the noise produced by the propeller across its blade span. Sections 7.3.2 and 7.3.3 analyzes the variation in the directivity of the noise generated by the propeller along its axial and radial plane.

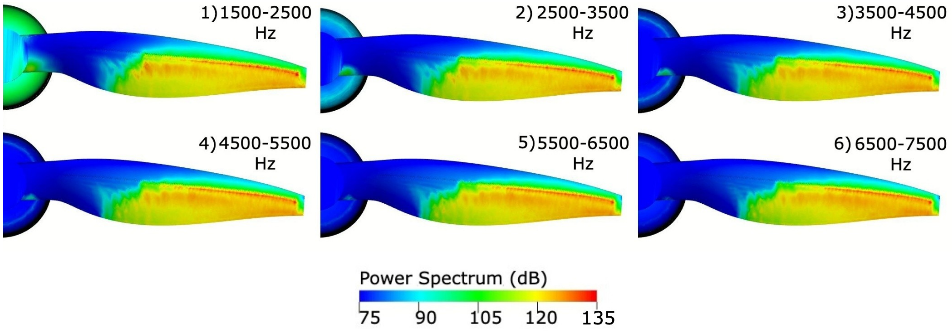

(a) Surface pressure fluctuation (dB) on the suction side of the propeller blade at 0^o AoA

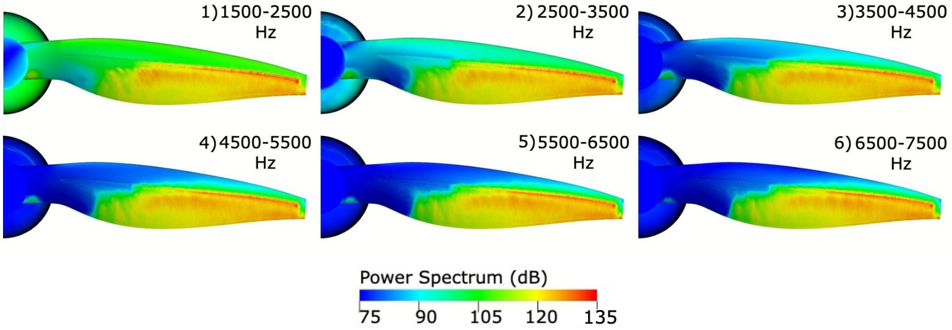

(b) Surface pressure fluctuation (dB) on the suction side of the propeller blade at 15^o AoA

Figure 7.8: Surface pressure fluctuation (dB) between $1,500 - 7,500$ Hz at $1,000$ Hz interval; contour range 60 dB.

7.3.1. Source noise

Sections 7.1 and 7.2 discussed how the forces and flow parameters varied across the propeller blade with a change in AoA. The present section quantifies those variations in terms of the sound power level (PWL) across the propeller blade span. Measured against a reference value of 10^{-12} watts, the PWL is measured using the dB scale. The difference between PWL and SPL is their dependencies upon distance. SPL measures the pressure fluctuation produced by a sound wave when it reaches a receiver, it depends upon the distance between the source and the receiver. PWL measures the amount of energy produced by a source of the sound and is independent of the distance between the source and observer. PWL is hence preferred to measure the variation in the source strength (propeller blade) with a change in AoA.

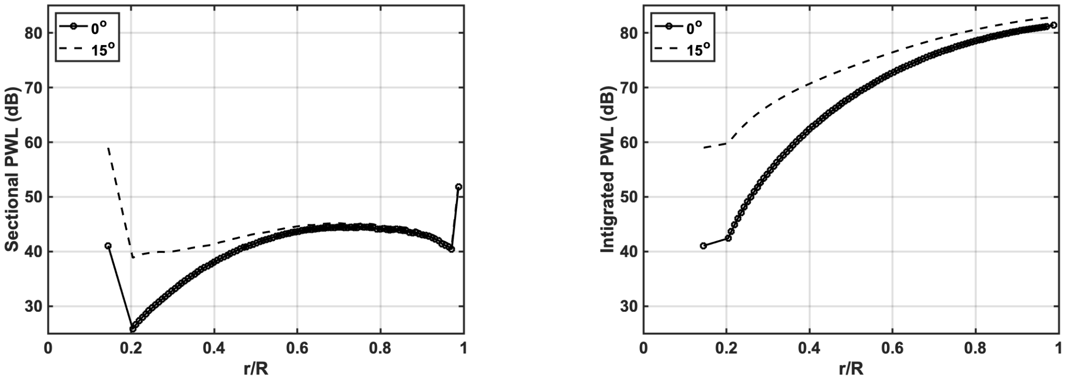

(a) Sectional sound power level

(b) Integrated sound power level over the blade span

Figure 7.9: Sound power level across a the propeller blade

Fig. 7.9 presents the sectional (Fig. 7.9a) and integrated (Fig. 7.9b) PWL across the propeller blade span for 0^o and 15^o AoA. The PWL is calculated by segmenting the propeller blade across its span using the structured mesh generated by the $Opty\partial b^{®}$ package and then calculating the pressure fluctuation over the individual sections. The structured mesh at the root ($r/R = 0 - 0.2$) and tip ($r/R = 0.975 - 1$) section of the propeller blade are not segmented like the rest of the blade span. It results in the region having a relatively larger area than the rest of the segmented blade section, causing the peak in the PWL values at the root and tip section, as observed in Fig. 7.9a. Analysis of the sectional PWL reveals that significantly higher noise is generated at the root region. For $r/R = 0 - 0.4$ the average PWL between 0^o to 15^o varies by $7\ dB$, with the difference rising close to $13\ dB$ near the root and reducing to $3\ dB$ closer to $r/R = 0.4$. The increase in surface pressure fluctuation at 15^o observed in Section 7.2.3 can be a plausible explanation for the higher PWL level in the same region. Moving towards the tip, the difference in sectional PWL collapses to less than $2\ dB$, which again follows a similar trend observed by the surface pressure fluctuations. The net noise produced by the propeller blade at 15^o AoA is 83 dB, which is $1.5\ dB$ higher than the noise produced by it at 0^o AoA. It implies that the variation in PWL at the root region has a marginal impact on the overall PWL of the propeller blade. The effect change in AoA has on the directivity of noise shall be explored in the following sections.

7.3.2. Radial directivity

The present section analyses the variation in the OASPL with AoA around the radial plane. It is measured for a frequency range of $40 - 10,000\ Hz$ using a circular microphone array of $1\ m$ radius. In the present simulation, the AoA is changed by varying the inflow angle instead of changing the propeller position. As a result, the distance of the microphones wrt. the propellers remain constant. It eliminates a source of uncertainty caused in the measurements due to the relative shift in propeller location. The directivity analysis is divided into a low-frequency ($40 - 1,000\ Hz$) and high-frequency ($1,000 - 10,000\ Hz$) plot. It is done to analyze the influence of frequency on directivity and find the dominating component of the OASPL.

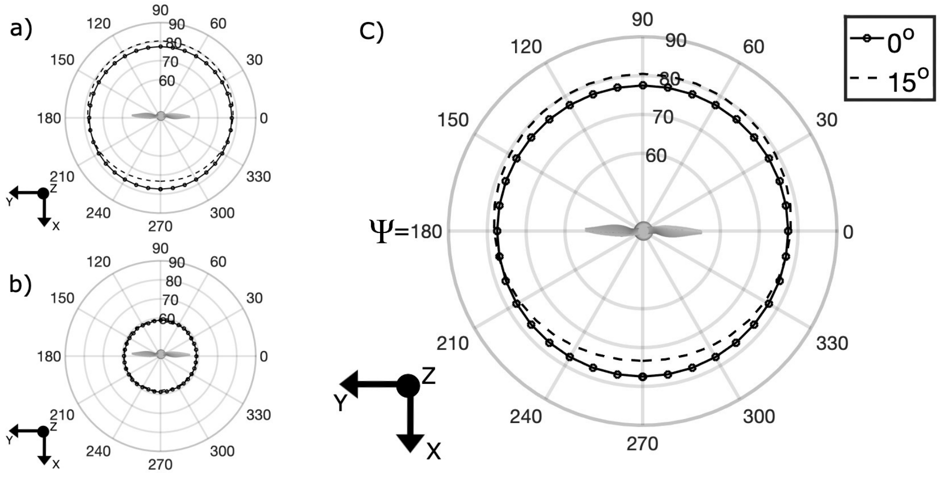

Figure 7.10: Radial directivity of OASPL; frequency range a) $40 - 1,000\ Hz$ b) $1,000 - 10,000\ Hz$ c) $40 - 10,000\ Hz$; measured at $1\ m$ from the propeller axis of rotation;

Fig. 7.10a shows the radial directivity of the noise produced by the first five BPF ($40 - 1,000 Hz$) of the propeller. Fig. 7.10b shows the directivity of the high-frequency noise produced by the propeller ($1,000 - 10,000\ Hz$). The OASPL for $40 - 10,000\ Hz$ is present in Fig. 7.10c. A comparison of the directivity plots reveals that the low-frequency noise dominates the OASPL in the radial direction. The broadband noise shows no variation in directivity with a change in AoA. At 0^o AoA, the propeller exhibits a symmetric directivity pattern about the plane of rotation. However, at 15^o, the directivity pattern becomes non-axisymmetric about $\Psi = 0 - 180^o$ axis. The OASPL in the propeller plane lying between $\Psi = 0^o - 90^o - 180^o$ is relatively higher at 15^o than 0^o AoA. The OASPL value reaches its highest value at $\Psi = 90^o$, where the OASPL is $3\ dB$ higher for 15^o AoA. The point of maximum variation is the same as predicted by [9] and no phase lead/lag is observed in the simulated as seen by [10, 11]. It is because of the difference in the measurement conditions and the type of propeller blades. Experiments by Woodward [10] and Mani [11] were conducted for large turboprops with multiple propeller blades and a significantly higher inflow and tip Mach number. A large number of blades operating at high tip

Mach numbers result in the propeller blades interacting with the wake produced by the other blades. It leads to the propeller blade experiencing unsteady loading, causing noise in higher harmonics of BPF. The unsteady noise also leads to the phase lead/lag effect observed by [10]. The present simulation uses a twin-blade propeller with a maximum tip Mach number of 0.3 and a freestream velocity of 12 m/sec. Visualizing the vortex field produced by the propeller in Section 7.2.2 made it apparent that the freestream velocity leads to the downstream convection of the vortices before they interact with the propeller blade. It reduces the impulsive change in propeller blade loading due to wake interaction, hence removing a source of unsteady noise that would cause tonal peaks at higher harmonics.

Fig. 7.11 presents the power spectrum analysis of the noise signal at three different azimuthal positions. The spectrum analysis is performed at a frequency bandwidth of $\Delta f = 20\ Hz$. It reveals the energy content of each frequency band and helps understand their variation across the azimuthal position. Based on the directivity plot in Fig. 7.10, power spectrum analysis of microphones placed at $\Psi = 90^o, 180^o$ and 270^o has been performed. The analysis reveals that the change in SPL level with the azimuthal position is restricted to mainly the 1^{st} and 2^{nd} BPF. At $\Psi = 90^o$ the tonal peak, at 1^{st} BPF, of the propeller is higher by $3\ dB$ for 15^o AoA and is reduced by an equal magnitude at $\Psi = 270^o$. The power spectrum plot for both 15^o and 0^o AoA, show three distinct tonal peaks at multiples of BPF with minimal difference in the spectrum at a higher frequency. It is in line with the observation made in Section 7.2.3 that the propeller blades would exhibit similar broadband characteristics despite the change in operational AoA.

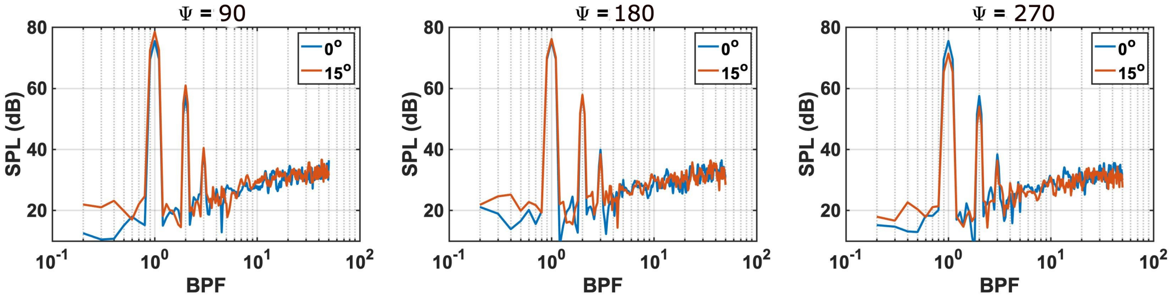

Figure 7.11: Variation in spectrum level around the propeller plane

7.3.3. Axial directivity

In the present section, the directivity of the OASPL is analyzed along the propeller axis in the XZ plane. The analysis is performed using a circular array of 36 microphones, using the same methodology described in Section 7.3.2. In a CAA simulation, microphones do not disturb the flow. As a result, it is feasible to place microphones upstream of the propeller plane. The ability enables a 360^o analysis of the OASPL along the propeller axis, which is extremely difficult, if not impossible to achieve in experiments.

Fig. 7.12a, b, & c represents the variation of the OASPL for 0^o and 15^o around the XZ plane for a frequency range of $40 - 1,000\ Hz$,$1,000 - 10,000\ Hz$, and $40 - 10,000\ Hz$ respectively. The directivity plot for the low and high-frequency range in Fig. 7.12a & b exhibit a dipolar noise radiation pattern associated with steady loading and broadband noise, respectively. In the low frequency region the variation in the tonal noise is similar to that observed around the propeller plane, with $\theta = 0^o \rightarrow 90^o \rightarrow 180^o$ experiencing higher noise than $\theta = 180^o \rightarrow 270^o \rightarrow 0^o$. As the propeller location remains the same wrt. the microphone, the change in directivity can be attributed to the relative change in pressure amplitude produced by the propeller blade due to the changes in propeller tip Mach number and blade AoA. Another interesting observation is the dominance of broadband noise in the axial directivity of noise in the forward and aft direction. For $\theta = 330^o \rightarrow 0^o \rightarrow 30^o$ and $\theta = 150^o \rightarrow 180^o \rightarrow 210^o$ the broadband noise is significantly higher than the tonal component. It is due to the dipolar nature of the two acoustic sources and the 90^o phase difference due to the difference in their noise generation mechanism, as discussed in Section 3.1.2.

Fig. 7.13 presents the noise spectra for the signal at $\theta = 90^o$, 0^o and 270^o. For $\theta = 0^o$ it can be observed that there is a lack of tonal peak in the power spectrum plot. It is due to the destructive interference of the pressure wave-forms produced by the propeller blades which are equal in magnitude

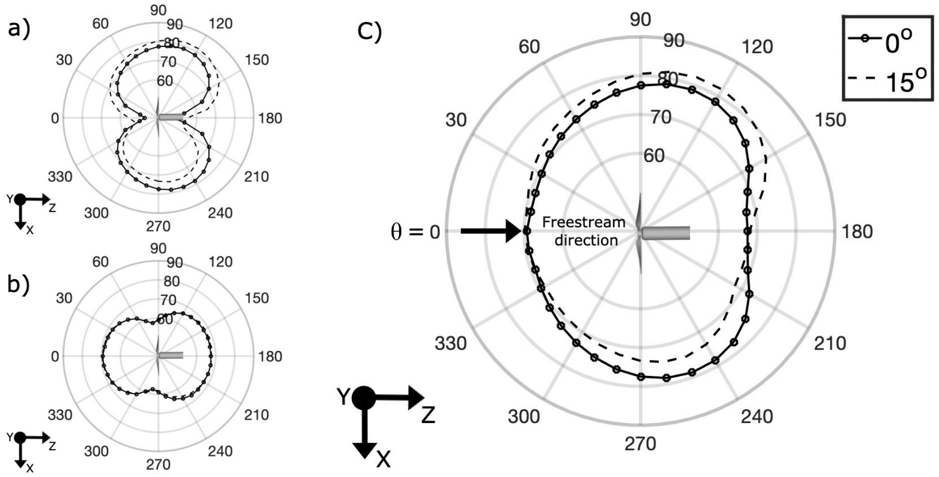

Figure 7.12: Axial directivity of OASPL; frequency range a) $40 - 1,000\ Hz$ b) $1,000 - 10,000\ Hz$ c) $40 - 10,000\ Hz$; measured at $1\ m$ from the propeller axis of rotation;

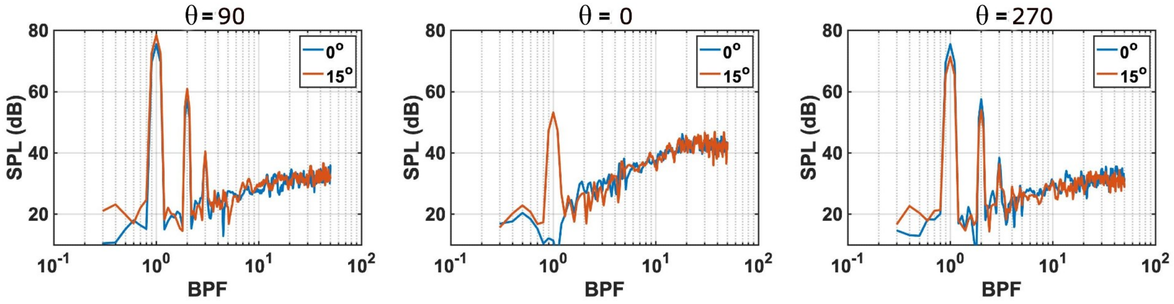

Figure 7.13: Variation in noise spectra along the axial direction

but opposite in phase. However, at 15^o AoA, there is an asymmetry in the blade loading about the propeller plane, which results in the singular tonal peak observed for 15^o AoA.

8

Conclusions and Recommendations

The present chapter consists of the conclusions drawn from the result of this study and makes recommendations for the extension of this work. The conclusion drawn from the study has been presented in terms of the research questions listed out in Section 3.3. Section 8.2 discusses the scope of expansion of the present study and additional analysis that can be carried out to understand the aerodynamic and aeroacoustics characteristics of propeller operating at low Reynolds number.

8.1. Conclusions

This section aims to answer the research questions set in Chapter 3 by concluding the results discussed in Chapters 6 and 7. The research questions and their answers have been discussed below:

1. **What is the computational resource required in conducting a study of the impact of AoA on aerodynamics and acoustic characteristics of a low Reynolds number propeller?**
    - What is the required grid resolution to accurately capture all the flow phenomena?
        - In this study, three different grid resolutions were analyzed to check for grid independence and validated against experimental data. The medium resolution set up with $18.6 * 10^6$ fine equivalent voxels, with the smallest voxel size of $5.7 * 10^{-5}\ m$ was found sufficient in capturing all the flow phenomena.
    - What is the impact on the accuracy of results with changes in grid resolution?
        - The value of C_T was under-predicted by 6.3% in the coarse setup compared with the medium resolution setup. The difference in C_T value was limited to 0.3% between the medium and fine resolution setup. At 2% the C_Q values showed slightly higher variation between the medium and fine resolution setup. However, these were within acceptable levels to prove for grid independence of the results. To check for the accuracy of the force coefficient were compared against experimental data. It was found that the medium resolution setup under-predicted the C_T values by 8.5% and over-predicted C_Q value by 9.3%. These values indicate a reduction in the accuracy of the simulation with reducing grid resolution.
          The coarse resolution setup is unable to resolve the smaller flow structures close to the propeller blade. It results in the variation in force coefficients with grid resolution for the simulations. The differences in force coefficients between the experimental and simulation results could be due to the difference in flow characteristics over the propeller blade. The difference occurs due to the forced transitioning of the flow over the propeller blade surface in the simulation.
          In terms of acoustic values, the low-frequency tonal noise shows a negligible variation with grid resolution. The tonal noise dominates the noise spectrum, consequently, the OASPL (from $40 - 10,000\ Hz$) also remains steady with the change in grid resolution. The broadband OASPL is higher by $6\ dB$ (for $1,500 - 2,500\ Hz$) for the coarse resolution wrt. the medium resolution. The coarse resolution setup is unable to resolve small-scale

    turbulence close to the propeller blade. It results in higher pressure fluctuations along the blade trailing edge resulting in higher broadband noise generation.

- How does the variation in AoA impact the accuracy of the results at a similar grid resolution?
    - The variation in AoA had a negligible impact on the accuracy of the results for similar grid resolution. It signifies that the medium resolution setup can be used for the entire range of AoA ($0^o - 15^o$) with similar flow conditions.

2. **What is the impact on Aerodynamics characteristics of the propeller with a change in AoA**

    - What impact does a change in AoA have on the overall performance and efficiency of the propeller?
        - The change in AoA, from 0^o to 15^o, increases the thrust produced by the propeller from 6.84 to $7.11\ N$. The 3.87% increase in the net C_T value per rotation is accompanied by an increase in C_Q value by 1.16%. It results in an overall increase in propeller efficiency from 53.66% to 54.88%.
    - How does the thrust and torque value vary across the propeller blade with a change in AoA and azimuthal position?
        - The propeller blade exhibits a cyclic variation in blade loading around the propeller plane. It experiences maximum loading of $4.3\ N$ at $\Psi = 17^o$ and $2.8\ N$ at $\Psi = 198^o$, which is a 35% variation between the point of maximum and minimum loading. In terms of span-wise variation of thrust and torque value, the maximum % variation with AoA occurs at the root region, followed by the mid-span and the propeller tip region. The coupled influence of the Reynolds number effect and higher variation in resultant velocity at the root region ($0 < r/R < 0.4$) results in over 30% variation in the sectional thrust value at $\Psi = 0^o$ for 0^o and 15^o AoA.
    - What is the impact of the change in AoA on the flow filed?
        - The flow field is analyzed by visualizing the mean velocity and phase-locked vorticity in the wake of the propeller. The velocity field is axially symmetric for 0^o AoA about the XZ and YZ plane of symmetry. For 15^o AoA, the average velocity field is no longer axisymmetric about the plane of symmetry. The asymmetry in propeller blade loading leads to a 6% higher velocity magnitude in the advancing side ($\Psi = 270^o \rightarrow 0^o \rightarrow 90^o$) of the YZ plane. Analyzing the mean velocity shows a clear correlation between blade loading and mean velocity. The asymmetry of the downstream velocity field replicates the blade loading pattern about the propeller plane.

          The tip vortices being shed by the propeller no significant variation in strength and remain coherent for 0^o and 15^o AoA. The change in AoA has a visible impact on the downstream convection of the root vortex. The change in inflow angle, at 15^o, causes the root vortex to interact with the support structure. It results in the breakdown of the coherent vortical structure and acceleration of the flow close to the support strut. The inflow angle has a relatively higher influence on the resultant velocity and blade loading in the root region ($0 < r/R < 0.4$) of the propeller. It results in a significant variation in the vortices produced in this region. A consequence of this is the change in surface pressure fluctuation and hence the noise generated by the propeller blade.

3. **What is the impact on the acoustic characteristics of the propeller with a change in AoA?**

    - How does the sound power level (PWL) produced by the propeller change with AoA? How does it relate to the aerodynamic characteristics of the propeller blade?
        - The average PWL in the root region ($0 < r/R < 0.4$) of the propeller varies by $7\ dB$ between 0^o and 15^o AoA. The sectional measurements shows that the PWL for 15^o AoA is $13\ dB$ higher at $r/R = 0.2$ as compared to 0^o AoA. The difference reduces to $3\ dB$ at $r/R = 0.4$ and is less than $1\ dB$ as it moves closer to the tip. The net PWL increases by $1.5\ dB$ for the propeller blade at 15^o AoA as compared to 0^o AoA.

          The sound produced is directly dependent upon the amount of pressure fluctuation produced by the source. Hence, the observed variation in PWL was correlated against the surface pressure fluctuation map for different frequency ranges. The pressure fluctuation on the propeller blade surface showed similar trends of variation with change in AoA. The pressure fluctuations in the root region of the propeller showed significantly higher variation with change in AoA. It can be attributed to the relatively higher changes in resultant flow velocity and blade loading in this region.

- How does the axial and radial directivity of the noise produced change with changing AoA?
  - In the radial plane, the tonal component dominates the OASPL and directivity of noise. The change in AoA leads to an asymmetry in the noise radiation pattern in the radial plane. The OASPL is higher by $3\ dB$ at $\Psi = 90^o$ for 15^o AoA and reduces by an equal magnitude at $\Psi = 270^o$. The variation is limited to the 1^{st} and 2^{nd} BPF tones of the propeller noise. The Broadband spectrum shows a negligible variation with change in AoA. It is expected as the surface pressure fluctuation on the propeller blade in the high-frequency region is almost identical at higher magnitudes closer to the tip of the propeller.

    In the axial direction, a similar trend is observed for directivity as in the radial plane. The broadband noise dominates the OASPL directly aft and in front of the propeller blade. The tonal noise in this region is similar in magnitude but opposite in phase. It leads to the cancellation of the tonal peaks resulting in lower tonal noise.
- What changes occur in the SPL levels of higher harmonics due to change in AoA?
  - The variation in higher harmonics is primarily caused due to impulsive changes in loading caused due to turbulent inflow conditions, Blade vortex interaction, etc. In the present simulation due to a relatively high freestream velocity of $12\ m/sec$ and a uniform inflow condition. The propeller blades do not experience any impulsive change in blade loading despite the change in AoA. As a result, there is no change in higher harmonics with a change in AoA.

8.2. Recommendations

This section lists out the various recommendations that can help expand on the present study and further enhance the understanding of the effect of inflow angle on low Reynolds number propeller:

- **Trip placement:** in the present study the trip is placed at the quarter chord length on the suction side of the propeller blade. To analyse the effect of trip on the aerodynamics and acoustic characteristics, the trip position can be changed to better suite the natural transition point of the flow. Trips can also be added on the pressure side of the blades and results compared with untripped simulation.

- **Change in AoA and RPM:** due to time and resource constraint, this study only analysed two AoAs at fixed RPM and freestream velocity. The study can be expanded further to include multiple AoAs, advance ratio (J), and hover condition. Doing so would help develop a better understanding of the impact of inflow condition on the propeller acoustics. Analysing the propeller at hover condition for different AoAs would also help capture additional sources of noise such as blade vortex interaction, etc.

- **Numerical beamforming:** Numerical beamforming can be applied in the simulation to isolate the source of noise for a specific frequency range across the propeller blade span. It would enhance the understanding of the regions producing noise and the subsequent impact of AoA on them.

- **Development of low fidelity model:** high fidelity tools are resource-intensive and are not suitable for preliminary design and getting quick estimates. The results of the present study can be used to validate low fidelity models for propellers operating in non-axial inflow conditions. Since low fidelity tools require significantly lesser computational resources, they can be used in conjunction with other low fidelity models to get reasonable estimates on UAV performance early on in the design phase.

A

Appendix

This section aims to provide additional information to support the concepts/points discussed in the report.

Microphone location

The microphone locations of ARRAY-2 in the computational domain wrt. the default co-ordinate system.

Microphone Number	X-Axis (m)	Y-Axis (m)	Z-Axis (m)	θ $(^o)$
1	1.12	0	0.80	234.44
2	1.28	0	0.64	243.52
3	1.40	0	0.44	252.49
4	1.47	0	0.23	261.24
5	1.5	0	0	0
6	1.47	0	-0.23	278.76
7	1.40	0	-0.44	287.51
8	1.28	0	-0.64	296.48

Table A.1: Microphone location of ARRAY 2 in the simulation domain at $\alpha = 0^o$

Microphone Number	X-Axis (m)	Y-Axis (m)	Z-Axis (m)	θ $(^o)$
1	1.12	0.8	0.80	234.44
2	1.28	0.91	0.64	243.52
3	1.40	1	0.44	252.49
4	1.47	1.04	0.23	261.24
5	1.5	1.06	0	0
6	1.47	1.04	-0.23	278.76
7	1.40	1	-0.44	287.51
8	1.28	0.91	-0.64	296.48

Table A.2: Microphone location of ARRAY 2 in the simulation domain at $\alpha = 15^o$

NASA SR series propellers

During the 1980s researchers at NASA developed a series of advanced propellers that were studied for their aerodynamic and acoustics characteristics. These propellers were known as the SR series of propellers. The literature reviewed for this thesis has analyzed the SR-2 and SR-7A series of propellers. The SR-7A propeller is similar to the SR-3 propeller [10]. Figure A.1 shows the blade profile of the different SR series propeller blades.

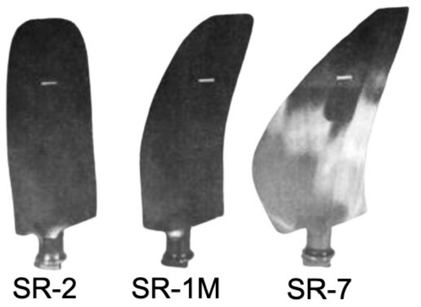

Figure A.1: NASA SR series propeller blades[8]

The SR-7A and SR-2 propeller used by Woodward [10] and Whitefield [11] had a diameter of 62.2 cm, designed Mach number of 0.8, and a designed tip speed of $244\ m/sec$.

Advancing and retreating side

In the computational setup, the inflow AoA is changed to simulate the effect of AoA, and the propeller blades rotate in a counter-clockwise direction, as shown in Figs. A.2a and A.2b. AoA can also be simulated by keeping the inflow angle constant and changing the propeller AoA as shown in Fig. A.2c.

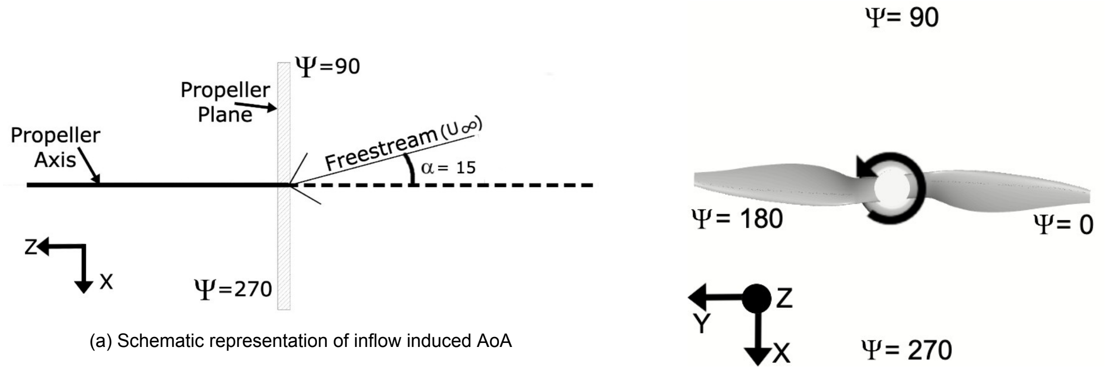

(a) Schematic representation of inflow induced AoA

(b) Propeller view (forward looking aft)

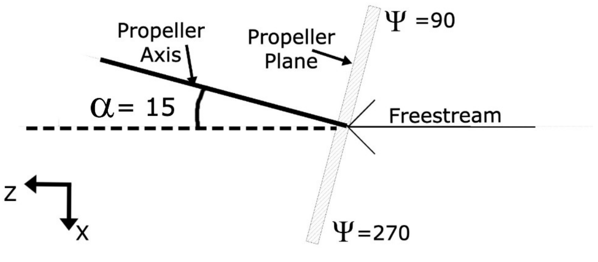

(c) Schematic diagram of propeller induced AoA

Figure A.2: Simulating AoA in the computational setup

To explain the concept of advancing and retreating sides, the resultant velocity and AoA will be calculated using velocity triangles. The calculations are performed at a radial location (r/R) of 0.53 and azimuthal position of $\Psi = 0^o$ and 180^o for 0^o and 15^o AoA. Fig. A.3a, shows the inclination of the propeller shaft relative to the freestream. The airfoil marked in red moves downwards (towards $\Psi = 270^o$), whereas the one marked in blue moves upwards (towards $\Psi = 90^o$). At $\alpha = 0^o$, the propeller experiences uniform loading around the propeller plane. Fig. A.3b shows the resultant velocity (V_r) for the propeller blade element at $r/R = 0.53$. At $\alpha = 15^o$, the propeller blade experiences varying loads around the propeller plane. The loads vary due to the change in local AoA and resultant velocity experienced by the propeller at the different azimuthal positions. Figs. A.3c and A.3d show the variation in resultant velocity and the corresponding change in AoA between the downward moving propeller blade (at $\Psi = 180^o$) and upwards moving propeller blade at ($\Psi = 0^o$). The downward moving blade experiences a lower resultant velocity over the blade section as compared to the upwards moving blade it results in a lower AoA and hence lower blade loading. The advancing side refers to the section of the propeller plane where the blades experience higher blade loading ($\Psi = 270^o \rightarrow 0^o \rightarrow 90^o$), while $\Psi = 90^o \rightarrow 180^o \rightarrow 270^o$ is defined as the retreating side.

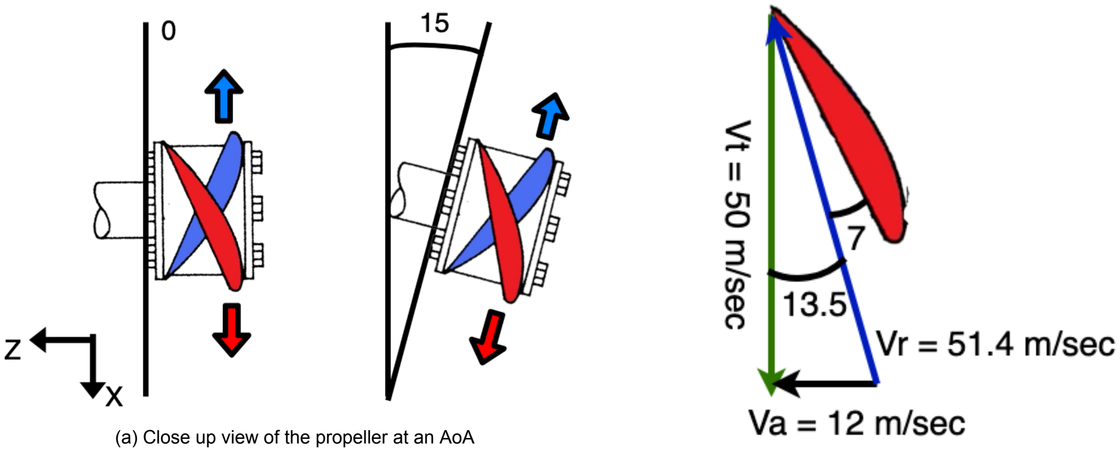

(a) Close up view of the propeller at an AoA

(b) Propeller blade at $\alpha = 0^o$

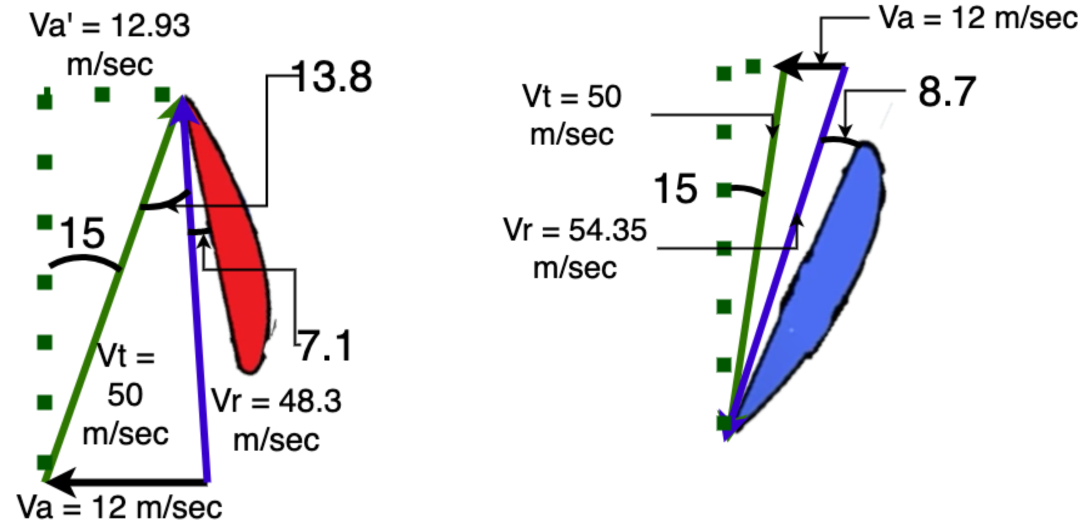

(c) Propeller blade at $\Psi = 180^o$ moving downwards, $\alpha = 15^o$

(d) Propeller blade at $\Psi = 0^o$ moving upwards, $\alpha = 15^o$

Figure A.3: Variation in AoA and resultant velocity for propellers with an AoA

Permeable vs solid surface acoustic data

Fig. A.4, shows the difference in SPL between the solid and permeable FWH surface. The differences calculated are for each permeable integration surface instead of averaging the contribution of all three surfaces.

Sectional blade AoA

Fig. A.5, shows the average variation in sectional blade AoA around the azimuthal plane (Ψ).

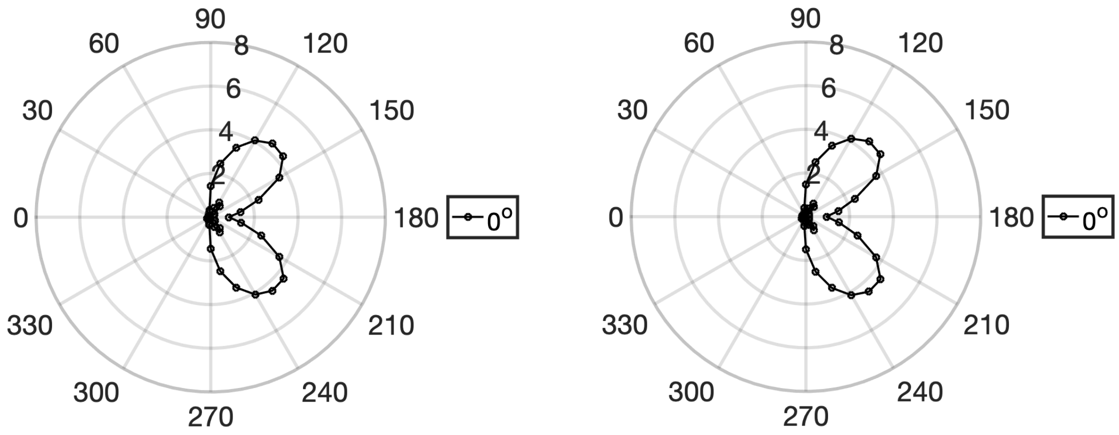

(a) Difference between FWH SLD and 1^{st} FWH PRM

(b) Difference between FWH SLD and 2^{nd} FWH PRM

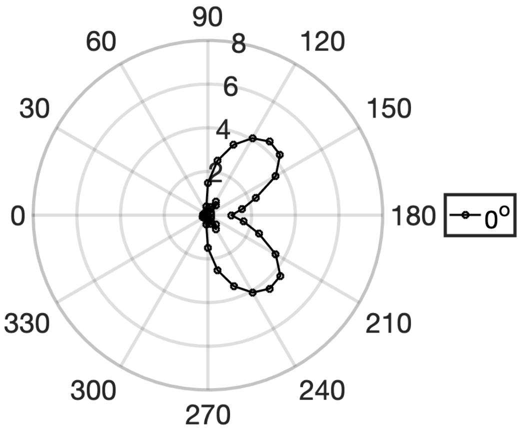

(c) Difference between FWH SLD and 3^{rd} FWH PRM

Figure A.4: Difference between FWH SLD and the the three individual FWH PRM surface

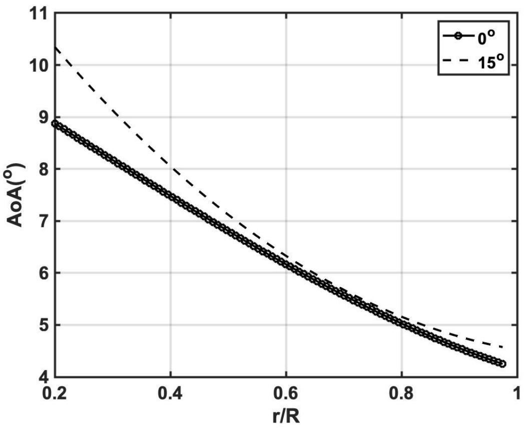

Figure A.5: Average change in AoA across blade span.

Axial velocity profile

Fig. A.6 shows the average velocity profile in the propeller slipstream along the axial direction. The average has been calculated for five propeller rotations.

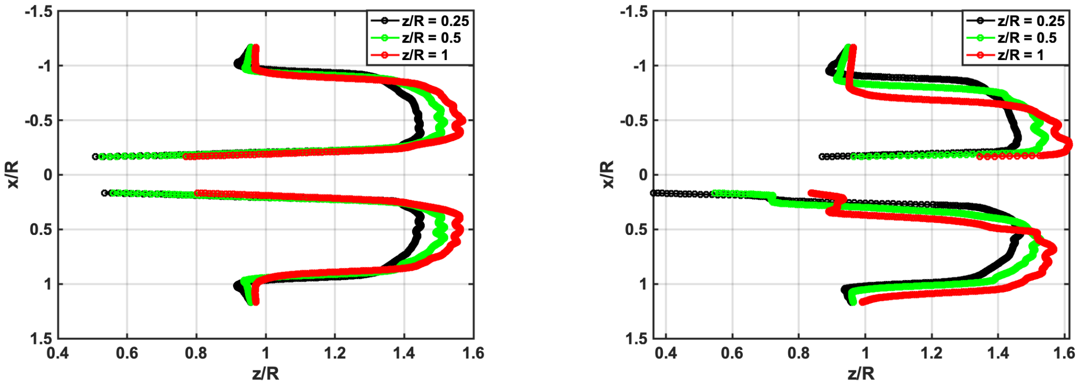

(a) Axial velocity profile at 0^o AoA

(b) Axial velocity profile at 15^o AoA

Figure A.6: Mean axial velocity profile in the propeller slipstream

B

Appendix

This section provides the formulas for the different non-dimensional parameters used throughout the thesis.

Non-dimensional parameters

Coefficient of thrust (C_T)

$$C_T = \frac{T}{\rho n^2 D^4} \tag{B.1}$$

Coefficient of Torque (C_Q)

$$C_Q = \frac{Q}{\rho n^2 D^d} \tag{B.2}$$

Advance ratio (J)

For axial inflow condition:

$$J = \frac{U_\infty}{nD} \tag{B.3}$$

$$J_{IF} = \frac{U_\infty cos(\alpha)}{nD} \tag{B.4}$$

where α is the AoA.

Propeller efficiency (η)

The propeller efficiency is the ratio of the power supplied (P_{in}) to the use-full output produced by the propeller (P_{out}), and is defined as:

$$\eta = \frac{P_{in}}{P_{out}} \tag{B.5}$$

it can be calculated using:

$$\eta = \frac{1}{2\pi} \frac{C_T}{C_Q} J \tag{B.6}$$

Non-dimensional velocity

$$\text{Velocity [-]} = \frac{U}{U_\infty} \tag{B.7}$$

U defines the velocity being measured.

Non-dimensional vorticity

$$\text{Vorticity [-]} = \frac{\omega}{\omega^*} \tag{B.8}$$

ω is the compute vorticity magnitude, and ω^* is calculated as:

$$\omega^* = \frac{l}{U_\infty} \tag{B.9}$$

l is the characteristic length at $23\ mm$, and U_∞ is the freestream velocity at $12\ m/sec$.

Bibliography

[1] Andrew Christian. Initial investigation into the psycho-acoustic properties of small unmanned aerial system noise. *23rd AIAA/CEAS Aeroacoustics Conference*, June 2017.

[2] Jr H. H. Hurt. *Aerodynamics for Naval Aviators*. Naval air system command, 1965.

[3] Topper Learning. *Basic of sound*, accessed: 01.2.2020. `https://www.topperlearning.com/answer/`.

[4] Joshua Jordaan. *Acoustic Meta-atoms: An Experimental Determination of the Monopole and Dipole Scattering Coefficients*. The Department of Engineering Australian National University, 2017.

[5] D. G. Simons. *Introduction to Aircraft Noise (Course Reader for AE-4431 in Master Track of TU Delft Aerospace Engineering)*. Tu Delft, Kluyverweg 1, 2629 HS Delft, 2018.

[6] Wikipedia. *A-Weighting*, accessed: 01.2.2020. `https://en.wikipedia.org/wiki/A-weighting`.

[7] Stewart Glegg & William Devenport. *Aeroacoustics of low Mach Number Flows*. Academic Press, 2017. ISBN 978-0128096512.

[8] Roberto Merino Martínez. *Microphone arrays for imaging of aerospace noise source*. Tu Delft, 2018. ISBN 978-94-028-1301-2.

[9] W.M. Dobrzynski. The effect on radiated noise of non-zero propeller rotational plane attitude. *AIAA 10^{th} Acoustic Conference*, July, 1986.

[10] Richard P. Woodward. Measured noise of a scale model high speed propeller at simulated take-off/approach conditions. *AIAA 25^{th} Aerospace Sciences Meeting*, January, 1987.

[11] C.E. Whitefield. High speed turboprop aeroacoustics study. *NASA Contractor Report 182257*, 1989.

[12] Ramani Mani. The radiation of sound from a propeller at angle of attack. *NASA Contract Report 4264*, 1990.

[13] Nikolas S. Zawodny. Acoustic characterisation and prediction of representative, small-scale rotary-wing unmanned aircraft system component. *American Helicopter Society Annual Forum*, May, 2016.

[14] Nikolas S. Zawodny. Investigation of rotor-airframe interaction noise associated with small scale rotary wing aircraft system. *Journal of the American Helicopter Society*, 65:1–17, January 2020.

[15] Y. Yang. Aerodynamic and aeroacoustic performance of isolated multicopter rotor during forward flight. *AIAA propulsion and energy forum*, July, 2018.

[16] Yuanxum Bao. Lattice boltzmann method for fluid simulation. April, 2014.

[17] D. Herrmann. A study of the suitability of powerflow as an educational engineering design tool for undergraduate students. *Thesis Report*, University of Stuttgart.

[18] D.B. Hanson. Influence of propeller design parameters on far-held harmonic noise in forward flight. *AIAA*, 18:1313–1319, 1980.

[19] Physics LibreTexts. *Speed of Sound, Frequency, and Wavelength*, accessed: 01.2.2020. `https://phys.libretexts.org/`.

[20] Commercial drone market size, share trends analysis report by application (filming photography, inspection maintenance), by product (fixed-wing, rotary blade hybrid), by end use, and segment forecasts, 2019 - 2025. `https://www.grandviewresearch.com/industry-analysis/global-commercial-drones-market`, Accessed: September 2020.

[21] John F. Groeneweg. Aeroacoustics of advanced propellers. *17th Congress of the international Council of Aeronautical Sciences*, 1990.

[22] D.B. Hanson. Sound from propeller at angle of attack: a new theoretical viewpoint. *The Royal Society*, pages 315–328, 1995.

[23] Eugene A. Krejsa. Prediction of the noise from a propeller at angle of attack. *13th Aeroacoustics Conference*, 1990.

[24] Simon Marié. Comparison between lattice boltzmann method and navier–stokes high order schemes for computational aeroacoustics. *Journal of Computational Physics*, 228, 2009.

[25] Flight Standards Service U.S. Dept. of Transportation, FAA. *Pilot's Handbook of Aeronautical Knowledge*. FAA.

[26] Frank E. Hitchens. *Propeller Aerodynamics: The history of Aerodynamics and operations of aircraft propellers*. Andrews UK Limited, 2015.

[27] D. Russell. Acoustic monopoles, dipoles, and quadrupoles: An experiment revisited. *American Journal of Physics*, 1999.

[28] Jack E. Marte & Donald W. kurtz. *A Review of Aerodynamic Noise from Propellers, Rotors, and Lift Fans*. NASA, Jet Propulsion Laboratory, Cal. Tech, Pasadena, california, 1970.

[29] Thomas F. brooks. Airfoil self-noise and prediction. *NASA Technical reports*, 1989. doi: 19890016302.

[30] S. Oerlemans. Location and quantification of noise sources on a wind turbine. *Journal of Sound and Vibration*, 299, 2007.

[31] W. C. P. van der Velden. *Computational aeroacoustic approaches for wind turbine blade noise prediction*. Tu Delft, 2017. ISBN 978-94-6186-756-8.

[32] Angus Leslie. Broadband noise reduction from a mini-uav propeller through boundary layer tripping. *Acoustics 2008*, November 2008.

[33] Oleg A. Godin. An exact wave equation for sound in inhomogeneous , moving, and non-stationary fluids. *OCEANS'11 MTS/IEEE KONA*, 2011.

[34] M. J. Lighthill. On sound generated aerodynamically .i general theory. *The royal society mathematical physical & Engineering sciences*, 222, 1952.

[35] M. J. Lighthill. On sound generated aerodynamically .ii turbulence as a source of sound. *The royal society mathematical physical & Engineering sciences*, 211, 1954.

[36] M.S. Howe. *Theory of vortex sound*. Cambridge university press, 2002. ISBN 9780521012232.

[37] A. Hirschberg & S.W. Rienstra. *An introduction to aeroacoustics*. Eindhoven University of Technology, 2004.

[38] N. Curle. The influence of solid boundaries upon aerodynamic sound. *The royal society mathematical physical & Engineering sciences*, 231, 1955.

[39] J. E. Ffowcs Williams and D. L. Hawkings. Sound generation by turbulence and surfaces in arbitrary motion. *The royal society mathematical physical & Engineering sciences*, 1151, 1969.

[40] WIKIBOOKS. *Engineering Acoustics/Analogies in aeroacoustic*, accessed: 01.2.2021. `https://en.wikibooks.org/wiki/Engineering_Acoustics/Analogies_in_aeroacoustics`.

[41] L. Gutin. On the sound filed of rotating propeller. *NASA technical memorandum 1195*, October, 1948.

[42] Donald B. Hanson. Helicoidal surface theory for harmonic noise of propeller in far field. *AIAA Journal*, 1980.

[43] S. L. Padula. Predicted changes in advanced turbo prop noise with shaft aoa. *AIAA* 9^{th} *Acoustic Conference*, 1:381–387, July, 1986.

[44] Thomas J. Muller. Aerodynamic measurements at low reynolds numbers for fixed wing micro-air vehicles. *Defense technical information center; unclassified report*, September, 1999.

[45] Justin Winslow. Basic understanding of airfoil characteristics at low reynolds numbers $(10^4 - 10^5)$. *Journal of Aircraft*, 55:1050–1061, May-June, 2018.

[46] Dustin E. Gamble. Automated dynamic propeller testing at low reynolds number. *48th AIAA aerospace sciences meeting*, 55:1050–1061, January 2010.

[47] *Propeller performance measurement for low Reynolds number unmanned aerial vehicle application*. Master's Thesis, Wichita State University, 2004.

[48] M. Selig. *UIUC Propeller Data Site*, accessed: 01.2.2020. `https://m-selig.ae.illinois.edu/props/propDB.html`.

[49] John B. Brandt. Propeller performance data at low reynolds number. *49th AIAA aerospace sciences meeting*, January 2011.

[50] R. macNelll. Blade element momentum theory extended to model low reynolds number propeller performance. *The Aeronautical Journal*, 121:835–857, May. 2007.

[51] B. Theys. Experimental and numerical study of micro-aerial-vehicle propeller performance in oblique flow. *Journal of Aircraft*, 54:1076–1084, May 2017.

[52] David Serrano. Effect of disk angle-of-attack on aerodynamic performance of small propellers. *Aerospace Science and Technology*, 92:901–914, 2019.

[53] C. E. Hughes. Low speed wind tunnel performance of high speed counter rotating propellers at angle of attack. *Aerospace Science and Technology*, 92:901–914, 2019.

[54] Rayan S. McKay. Multirotor unmanned aerial system propeller noise caused by unsteady blade motion. *25th AIAA/CEAS Aeroacoustic conference*, May,2019.

[55] Zhenyu Wang. A comprehensive approach to study aerodynamics and aeroacoustics of small multi copter unmanned systems. *AIAA SciTech Forum*, January,2018.

[56] Seokkwan Yoon. Computational aerodynamic modeling of small quadcopter vehicles. *AHS Forum 73*, 2017.

[57] Charles David Coffen. Tilt rotor hover aeroacoustics. *NASA contractor report 177598*, June 1992.

[58] S. Chen. Lattice boltzmann method for fluid flows. *Annual Review Fluid Mechanics*, 30:329-364: 329–36, 1998.

[59] L. Kadanoff. On two levels. *Physics Today*, 39:7–9, 1986.

[60] Damiano Casalino. Facing rim cavities fluctuation modes. *Journal of Sound and Vibration*, 333: 2812–2830, 2014.

[61] Hudong Chen. Recovery of the navier-stokes equations using a lattice-gas boltzmann method. *Physical Review A*, 45, April, 1992.

[62] Yao Deng. The lattice boltzmann method for compressible flows at high mach number. 23^{rd} *Annual Conference of the Computational Fluid Dynamics Society of Canada*, June, 2015.

[63] Dassault Systèmes. *PowerFLOW users Guide*. Exa Corporation, Release 5.5.

[64] Sauro Succi. *The Lattice Boltzmann Equation*. Oxford university press, 2001. ISBN 9780198503989.

[65] Christopher M. Teixeira. Incorporating turbulence models into the lattice-boltzmann method. *International Journal of Modern Physics C*, 9:1159–1175, 1998.

[66] D. Casalino. An advanced time approach for acoustic analogy predictions. *JOURNAL OF SOUND AND VIBRATION*, 2003.

[67] P.di Francescantonio. A new boundary integral formulation for the prediction of sound radiation. *Journal of sound and vibration*, 15 May 1997.

[68] Farassat F. The prediction of helicopter rotor discrete frequency noise. *Proceedings. American Helicopter Society International Annual Forum*, 38:497–507, 1982.

[69] Thomas Rossing. *Springer Handbook of Acoustics*. Springer-Verlag New York, 2014. ISBN 978-1-4939-0755-7.

[70] Schlichting H. *Boundary Layer Theory, 9^{th} edition*. Springer, 2002. ISBN 978-3-662-52919-5.

[71] F. Ducros. Large-eddy simulation of transition to turbulence in a boundary layer developing spatially over a flat plate. *Journal of fluid mechanics*, 326:1–36, 1996.

[72] J. Boudet. Implementation of a roughness element to trip transition in large-eddy simulation. *Journal of Thermal Science*, 24:30–36, 2015.

[73] L. Anselmi. *Computational analysis of ducted wind turbines noise*. Master's Thesis, TU Delft, 2017.

[74] Philippe R Spalart. On the differences in noise predictions based on solid and permeable surface ffowcs williams-hawkings integral solutions. *International Journal of Aeroacoustics*, 18:621–646, November, 2019.